MIMICKING THE PROPERTIES OF SCAR TISSUE IN SPINAL CORD INJURIES

DAVID RHYS JENKINS

Doctor of Philosophy

ASTON UNIVERSITY

September 2022

Thesis Summary

Spinal cord injury is a severe condition leading to paralysis below the point of injury, and the healing prospects over time with or without medical intervention are low. The economic costs derived from SCIs are enormous and lifelong. The average lifetime costs of a SCI are estimated around £1.12 million per patient in the United Kingdom. Only a handful of novel treatments are currently being developed and tested, mainly neuroprotective agents and stem cell therapies. As with any other disease or condition, SCI animal models have been invaluable to investigate the efficacy of therapeutic interventions and aim to recreate the pathology of human SCI as closely as possible. Because of the complexity of human SCI, there are no existing models that are able to encompass all aspects of injury in a robust and reproducible manner, which hinders the advance of new treatments. There have been few attempts to replicate the glial scar *in vitro*, mainly using monolayer cultures or simple three-dimensional alginate/collagen gels.

In this work, micro-hollow fibres were utilised to induce cellular alignment like that seen *in vivo* in the spinal cord. This strategy to induce a defined spatial distribution of neuronal cell types was paired with gellan gum fluid gels with mechanical properties similar to the spinal cord before and after injury as a mimic of the extracellular matrix in the healthy and damaged spinal cord.

The results from this project provide a more detailed understanding of the cellular and mechanical features that are seen after trauma in the spinal cord. This knowledge will also improve the research and development of novel therapeutic agents, including cellular therapies, as the platforms developed here will be more representative of the human situation, whilst simultaneously reducing the use of animals.

Acknowledgements

I would like to start by thanking my supervisor Dr Patricia Perez-Esteban, who has not only been a mentor but a friend through this PhD. For making sure that I believed in myself when I didn't, and making me appreciate my research experience through all the ups and downs that a PhD throws at you. Dr Eric Hill has added to this, from his invaluable help when I broke my wrist, to his endless knowledge and ideas about anything and everything. Prof Rhein Parri for his humour and always making me think, what's the question? Last but not least, to Dr Ewan Ross for his 16 days of impeccable supervision.

I would like to thank Aston University for funding this PhD, and allowing me to do research in a truly interesting topic.

Thank you to the whole lab group, who have made this an enjoyable experience, and for keeping me thinking with the constant questions. Specifically, I would like to thank Adele for teaching me everything iPSC and Dr Caves for keeping the lab going, and both of you for the continuous whinging which kept me sane. Dr Grainger who taught me, made me laugh and helped wherever possible, you were missed when you left Aston, but I have found a great friend.

I would like to apologise to my family for never being able to go up north due to cells, all the time, and thank you for all the support I could have ever needed, you've been amazing.

But finally, to the one who stood beside me every step of the way. From working months on end without a day off, cancelling plans because of cells, putting up with my stress, and supporting me more than I could ever have dreamed of. I hope I can make it up to you after this thing has finally been submitted and I can hopefully regain some semblance of a life. Thank you Squish, for everything.

List of Contents

Table of Contents

List of Abbreviations 6

List of Figures 8

List of Tables 12

Chapter 1 13

1. Introduction **13**

1.1. Physiological aspects of the healthy spinal cord 14
1.2. Spinal Cord Injuries 17
1.2.1. Biological and mechanical characteristics of injury – the glial scar 20
1.3. Current and novel treatments for spinal cord injuries 26
1.3.1. Gold standard clinical management strategies of spinal cord injuries 26
1.3.2. Pharmaceutical approaches 26
1.3.3. Cellular therapies 27
1.3.3.1. Oligodendrocyte Precursors 29
1.3.3.2. Mesenchymal Stem Cells 31
1.3.3.3. Neural Precursor Cells 31
1.4. *In vivo* and *in vitro* models of trauma 33
1.4.1. Animal models 33
1.4.2. In silico Models 35
1.4.3. Ex vivo models 35
1.5. Biomaterials in Tissue Engineering 37
1.5.1. Introduction 37
1.5.2. Types of Biomaterials Used for SCI modelling 38
1.5.2.1. Hydrogels 38
1.5.2.2. Fluid gels 40
1.5.2.3. Drug Delivery 41
1.5.2.4. Scaffolds 41
1.5.2.5. Micro-Hollow Fibres 42
1.5.2.6. Mimicking the spinal cord and spinal cord injuries 43
1.6. Stem cells for *in vitro* modelling 45
1.6.1. Introduction 45
1.6.2. Neural Precursor Cells 46
1.6.3. iPSC-derived motor neurons 47
1.7. Conclusions and gaps in knowledge 47

Chapter 2 49

2. Aim and objectives **49**

Chapter 3 52

3. Materials and Methods **52**

3.1. Cell culture 52
3.1.1. Cell Lines 52
3.1.2. Cell culture surface preparation 52
3.1.3. Storage and thawing of cell lines 52
3.1.4. NG108s and OECs 53
3.1.5. SH-SY5Y 54
3.1.6. SH-SY5Y Differentiation 54
3.1.7. Induced pluripotent stem cells (iPSCs) 55

3.1.8. Embryonic Stem cells 56
3.1.9. Neural induction of iPSCs 56
3.1.10. Neural Precursor Cells (NPCs) 57
3.1.11. Freezing NPCs 58
3.1.12. Motor Neuron Differentiation from NPCs 58
3.1.13. Neuronal Differentiation 59
3.1.14. Seeding Cells on Micro-Hollow Fibres 60
3.1.15. Immunofluorescent Staining (ICC) 60
3.1.17. Cell Tracker Green 64
3.2. Biomaterials fabrication and characterisation 64
3.2.1. Micro-hollow fibre (Micro-HF) fabrication 64
3.2.2. Morphological characterisation of micro-hollow fibres 65
3.2.3. Nuclear Magnetic Resonance (NMR) of micro-hollow fibres 66
3.2.4. Liquid permeation studies in micro-hollow fibres 66
3.2.5. Coating of micro-HFs for cell culture 67
3.2.6. Mounting of micro-HFs on 3D printed mounts for cell culture 68
3.2.7. Fabrication of fluid gels 68
3.2.8. Fabrication of fluid gels for cell culture 69
3.2.9. Morphological characterisation of fluid gels 69
3.2.10. Rheological characterisation of fluid gels 69
3.3. Cell Imaging 70
3.3.1. Live cell imaging 70
3.3.2. Fixed fluorescent imaging 70
3.4. Data visualisation and statistical analysis 71

Chapter 4 72

4. Biomaterials optimisation and characterisation 72
4.1. Introduction 72
4.1.1. Rheology 72
4.1.2. Rotational Rheometry 73
4.1.3. Gellan Gum 74
4.2. Results 76
4.2.1. Micro-hollow Fibre Morphology 76
4.2.2. Micro-Hollow Fibre Structural analysis via NMR 79
4.2.3. Liquid Permeation of Micro-Hollow Fibres 81
4.2.4. Optimisation of the fabrication method of Gellan Gum Fluid Gels 82
4.2.5. Morphological characterisation of gellan gum fluid gels 84
4.2.6. Rheology of gellan gum fluid gels 85
4.3. Discussion 92
4.3.1. PX:PCL Micro-HFs Fabrication and Characterisation 92
4.3.2. Gellan Gum Fluid Gel Fabrication and Characterisation 97

Chapter 5 100

5. Planar (2D) Cell Culture and Differentiation of Neuronal Cell Types for SCI Modelling 100
5.1. Introduction 100
5.1.1. SH-SY5Y 100
5.1.2. iPSCs and NPCs 101
5.2. Results 103
5.2.1. 2-Dimensional Cell Line Culture 103
5.2.2. PSCs Form Colonies Which Express Oct4 and Sox2 105
5.2.3. Neural Induction 106
5.2.4. Motor Neuron Differentiation 110
5.2.5. Excitatory Neuron Differentiation 114
5.2.6. Live Cell Tracking 115
5.3. Discussion 117
5.3.1. 2D Growth of SH-SY5Y Cells 117
5.3.2. Cell Viability for 3D Culture Preparation 117
5.3.3. iPSCs Could Efficiently Generate NPCs 119

5.3.4. Motor Neuron Differentiation 121
5.3.5. Synchronous Neuronal Differentiation 122
5.3.6. Cell Tracker Green Remained Stable During Differentiation 122

Chapter 6 124

6. Biomaterials in action 124
6.1. Introduction 124
6.2. Results 127
6.2.1. Multiple Cell Types Align Along Micro-Hollow Fibres 127
6.2.2. Scratch wound assay 142
6.3. Discussion 144
6.3.1. NG108-15s and Olfactory Ensheathing Cells align along the micro-hollow fibres 144

Chapter 7 147

7. General Discussion and Conclusion 147
7.1. Summary of Experimental Findings 148
7.2. General Discussion 151
7.2.1. Biomaterials 151
7.2.2. Cell Optimisation before the incorporation of biomaterials 153
7.2.3. Bringing all the elements of the model together 154
7.3. Conclusion 155

Chapter 8 157

8. Future Work 157
8.1. Motor Neurons 157
8.2. Measures of Differentiation 157
8.3. Electrical signalling and recording 158
8.4. Micro-fluidic chamber to induce damage 159
8.5. Increasing the variety of cell types in the model 159

Chapter 9 160

9. References 160

List of Abbreviations

4-OHT	4-hydroxy-tamoxifen
AFM	Atomic Force Microscopy
ASIA	American Spinal Injury Association
BB	Blocking buffer
BSA	Bovine serum albumin
BSCB	Blood-spinal cord barrier
C	Cervical
ChAT	Choline acetyl transferase
Coc	Coccygeal
CNS	Central nervous system
CSPG	Chondroitin sulphate proteoglycan
DMEM	Dulbecco′s Modified Eagle′s Medium
DMSO	Dimethyl sulfoxide
dPBS	Dulbecco’s Phosphate Buffered Saline
ECM	Extracellular matrix
EDTA	Ethylenediaminetetraacetic acid
ESC	Embryonic stem cell
FBS	Foetal bovine serum
FFT	Fast Fourier Transform
GFP	Green fluorescent protein
GG	Gellan gum
HF	Hollow fibre
hiPSC	Human induced pluripotent stem cell
ICC	Immunocytochemistry
IL	Interleukin
IPN	Interpenetrating polymeric hydrogels
iPSC	Induced pluripotent stem cell
L	Lumbar
MCP	Monocyte chemoattractant protein
MSC	Mesenchymal stem cell
MNP	Motor neuron precursor

NIM	Neural induction media
NMM	Neural maintenance media
NMP	1-Methyl-2-pyrollidone
NMR	Nuclear magnetic resonance
NPC	Neural precursor cell
OEC	Olfactory ensheathing cell
PCL	Polycaprolactone
PLGA	Poly(lactic-co-glycolic acid)
PFA	Paraformaldehyde
Poly-HEMA	Polyhydroxyethylmethacrylate
pORN	Poly-L-ornithine
PX	Polystyrene
RA	Retinoic acid
ROS	Reactive oxygen species
S	Sacral
SC	Spinal cord
SCI	Spinal cord injury
SEM	Scanning Electron Microscopy
SEM	Standard error of the mean
SHH	Sonic hedgehog
SLAM	Suspended layer additive manufacturing
T	Thoracic
TBI	Traumatic brain injury
TCP	Tissue culture plastic
TGF	Transforming growth factor
TNF	Tumour necrosis factor
ULA	Ultra-low attachment
VMAT	Vesicular monoamine transporter
VTN	Vitronectin
WHO	World Health Organisation

List of Figures

Figure 1: Anterior and posterior view of the spinal nerve sensory innervation (adapted from Bican et al., 2013). Diagram created using BioRender (www.biorender.com). 13
Figure 2: Experimental set-up for the fabrication of micro-hollow fibres via wet spinning using a single-orifice spinneret. Diagram created using BioRender (www.biorender.com). 55
Figure 3: Experimental set-up for liquid permeation of deionised water through the lumen of micro-hollow fibres and out of their pores. Diagram created using BioRender (www.biorender.com). 57
Figure 4: Schematic representation of a rotational rheometer. On the left-hand side, the sample is loaded onto a plate, and the rotator is lowered onto the sample, normally leaving a standard gap. On the right-hand side, the rotator is moving at a specific speed (measured in Hz, or 1/s) to determine the deformation of the sample material. Diagram created using BioRender (www.biorender.com). 63
Figure 5: Representative SEM micrographs of PX:PCL micro-HFs. (A) Cross section (X500); (B) Close-up of the cross section to demonstrate the wall's porous structure (X5,000); (C) micro-HF surface, showing the characteristic striations (X600); (D) Close-up of the micro-HF's surface with visible parallel grooves (X1,500). Scale bars: 50 µm (A), 5 µm (B), 20 µm (C) and 10 µm (D). Images were obtained in the imagining facilities at the University of Bath. 66
Figure 6: Representative SEM micrographs of PX:PCL micro-HFs. (A) Separation of the inner structure (X350), where the inner fibre peels off from the outer encasing micro-hollow fibre membrane; (B) Inner micro-fibre partially separated from the outer encasing micro-hollow fibre membrane, with a visible porous inner wall of the outer micro-fibre (X200). Scale bars: 50 µm (A) and 100 µm (B). Images were obtained in the imagining facilities at the University of Bath. 67
Figure 7: ^{1}H NMR spectrum of micro-HFs. (A) Whole fibre; (B) Inner fibre; (C) Outer fibre. Chemical shift of the peaks in the spectrum (ppm) is indicated at the top of each spectrum. The integration of relevant peaks is shown in red, and the approximate location in the spectrum of relevant peaks is annotated in Roman numerals in blue. i – $CDCL_3$. ii – aromatic hydrocarbons in PX, iii, iv and v – characteristic peaks of PCL. 69
Figure 8 - Liquid permeation through the porous walls of micro-HFS determined as cumulative mass of permeate over time compared to the cumulative inlet mass for a flow rate of 0.1 mL per min pumped through the inner lumen of micro-HFs. (N = 3, Error bars represent the standard deviation of three independent repeats). 70
Figure 9: Calibration of the peristaltic pump used to circulate cooling water through the jacket of the beaker used for fluid gel fabrication. A linear regression was performed, and the equation correlates the speed at which the mechanism of the pump moves (RPM) with the flow rate of water pumped (mL/min) – Pump speed (RPM) = 2.211 x (Flow rate) + 10.59. 71
Figure 10: Cooling rates of gellan gum fluid gels in DMEM salt solution (A); Comparison of gelling temperatures of gellan gum fluid gels prepared in DMEM salt solution. (N = 3, Error bars represent the standard deviation of three independent repeats). 73
Figure 11: Representative SEM micrographs of 7-day freeze-dried 0.6% (w/w) gellan gum in PBS made in non-cooled jacketed beaker. (A) X3,000; (B) X1,500; (C) X150; (D) X30. Images were obtained in the imagining facilities at the University of Bath 74
Figure 12: Comparison of mechanical testing of mammalian brain tissue. Numerical rheometry data was extracted from (JORBA et al., 2017, EBERLE, 2020, Ryu et al.,

2021, Mijailovic et al., 2021, Budday et al., 2017a, Budday et al., 2017b, Weickenmeier et al., 2018, Parkins et al., 2021, Nicolle et al., 2005, Kruse et al., 2008, Hamhaber et al., 2007, Weickenmeier et al., 2016, Moeendarbary et al., 2017, Millward et al., 2015, Green et al., 2008, Vappou et al., 2007, Wuerfel et al., 2010, Riek et al., 2012). Error bars represent SD. 76
Figure 13: Data analysis from (Moxon, 2016) relating concentration (% w/w) of gellan gum with elastic module measured via rotational rheometry. The dots shown in the figure represent actual published data, joined with a curve of best fit. The vertical and horizontal lines represent the range of concentrations to match stiffness/elastic moduli values in the range of 100 – 300 Pa. 77
Figure 14: Rheology of 0.6% (w/w) gellan gum fluid gels in PBS. (A) Frequency sweep (1%); (B) Amplitude sweep (1Hz). (N = 3, three independently prepared fluid gels tested three times each). 77
Figure 15: Rheology of gellan gum fluid gels in DMEM/F12. All percentages are (w/w). (A-B) 0.25% gellan gum, (C-D) 0.3175% gellan gum, (E-F), 0.375% gellan gum, (G-H), 0.5% gellan gum. A,C,E,G correspond to frequency sweeps, and B,D,F,H correspond to amplitude sweeps. (N = 3, three independently prepared fluid gels tested three times each). 78
Figure 16: Comparison of elastic moduli values for gellan gum fluid gels prepared in DMEM/F12 salts. N=3 three separate gels measured three times. Data is shown as mean ±.SEM, an ANOVA was performed with Tukey's multiple comparisons. 80
Figure 17: Growth curve of undifferentiated SH-SY5Y cells versus differentiated SH-SY5Y cells. Cells were seeded at 20,000 cells per cm^2 and counted at 24-, 72- and 120-hours post-seeding. RA was added after 24 to begin differentiation (N = 3). Statistical analysis was performed using ANOVA with Sidak's multiple comparisons post hoc test. 90
Figure 18: AlamarBlue® assay assessing cell viability. SH-SY5Ys were seeded with their respective condition, 10% AlamarBlue® was added to the respective media and normalised against fully reduced regent and the media to work out a % viability (N=3 independent repeats). ANOVA with Tukey's multiple comparisons was done comparing each condition to the control (regular 2D culture, black bar). 91
Figure 19: Representative ICC staining and quantification of LN5 iPSCs. LN5 iPSCs were cultures and expanded on human vitronectin in Essential 8 media. A, Sox2, B, Oct4, C, DAPI, D, merge, E, phase contrast, F quantification of iPSCS expression of Sox2 and Oct4 as a proportion of DAPI, n=3 ± SD, a t-test was performed, no statistical significance. 94
Figure 20: ICC of LN5 NPCs on human and mouse laminin. A, B, E, F, I, J, M, N, Q, R, U, V, mouse laminin C, C G, H, K, L, O, P, S, T, W, X, human laminin. A and C show Pax6 staining, B and D show Sox 2 staining I and K show nestin staining, J and L show Ki67 Staining, Q and S show Tuj staining and R and T show MAP2 staining. DAPI is shown in E, G, M, O, U and W. Merges are shown in F, H, N, P, V and X. Images are representative of n=3, taken at 20x objective, scale bar is 100µm. 95
Figure 21: NPC ICC quantification. NPCs were stained with Sox2, Pax6 and Ki67 and positive cell expression was quantified as a percentage of DAPI, n=3 SD shown with ANOVA and Sidak's multiple comparisons. 96
Figure 22: Motor neuron induction. An Olig2-GFP reporter line was used to test a motor neuron induction. Images taken at day 2 (A-B), day 4 (C-D) and day 6 (E-F) on a fluorescent EVOS M5000 scale bar = 125µm. 98
Figure 23: Motor neuron induction. An Olig2-GFP reporter line was used to test a motor neuron induction. Images taken at day 1 (A-B), day 4 (C-D), day 9 (E-F) and day 12 (G-H) after being passaged. Left hand images appear blank due to a lack of GFP expression. Images taken on a fluorescent EVOS M5000 scale bar = 125µm. 99

Figure 24: LN5 iPSC Motor neuron differentiation at 30 days post passage. A, Olig2, B, HB9, D, Pax6, E, Sox2, G, S100β, H, Tuj. C, F, I Merge. Images taken at 20x objective on Leica-epifluorescent microscope, scale bar 125μm. 100
Figure 25: ICC of neuronal differentiation from LN5 iPSCs. A, D, G show Tuj staining, B, E, H show CellTrackerTM Green staining and C, F, II show the merge with DAPI included. Images taken at 3 days (A-C), 7 days (D-F) and 12 days (G-I) after treatment with Compound E treatment began. Compound E treatment lasted for 7 days. Representative images from n=3, scale bar is 50μm, taken on Leica epifluorescent microscope. 102
Figure 26: Images and quantification of CellTrackerTM Green dye in culture during neuronal differentiation. CellTrackerTM Green was used in order to be able to see the NPCs whilst on the fibres. This was assessed in 2D to determine if it would last throughout the 7-14 day cultures. Cells were imaged after 1, 5, and 10 days, and analysed on ImageJ to determine how many pixels remained above the chosen threshold. n=3 An Anova with Tukey's multiple comparison post hoc test was carried out finding no significant difference. Scale bar 50 μm 103
Figure 27: Fluorescent micrographs of Live/Dead stained NG108-15s, OECs, a co-culture of NG108-15s and OECs (calcein-AM/ ethidium homodimer (EH)). All cell types were grown on micro-HFs for 6 days in three independent biological repeats each. Images were taken at day 3 and day 6. Green cells are live cells (Calcein-AM stain), and red cells are dead cells (EthD-III stain). Scale bars: 400 μm. 111
Figure 28: Quantification of cell directionality using the Fast Fourier Transform algorithm method, with cells grown on micro-HFs on day 3 (green), in planar culture on day 3 (control, red), on micro-HFs on day 6 (black) and in planar culture on day 6 (control, blue). (A) Directionality of NG108-15 cells. (B) Directionality of OECs. (C) Directionality of co-culture of NG108-15s and OECs. Data are normalized means to the largest frequency value ± SEM (N=3 independent biological repeats with 15 images analysed for each repeat). 113
Figure 29: Absolute value of the orientation angle with respect to the micro-HF axis for the highest frequency directionality peak for (A) NG108-15 cells; (B) OECs; (C) Co-culture of NG108-15s and OECs; (D) C2C12 Myoblasts. Controls refer to cells grown on 2D. Data are means ± SEM (N=3 independent biological repeats with 15 images analysed for each repeat). ANOVA with multiple comparisons, 95 % confidence, was carried out on the data shown (P values: ***P < 0.001, **P = 0.001 to 0.01, *P = 0.01 to 0.05, ns = not significant, P ≥ 0.05). 115
Figure 30: Number of cells attached to PX:PCL with different coatings and seeding densities. Cells were suspended in 1mL of media with the cell number required and 5 fibres were added. Fibres were stained with DAPI and the number of cells per cm of fibre was estimated. N=3 Anova with Tukey's multiple comparisons. Significance shown compares pORN/Laminin coatings to each other. 116
Figure 31: SH-SY5Y differentiation on PX:PCL micro-HFs. Cells were seeded at 1,000,000/mL in Eppendorf tubes. After 24 hours they were transferred to square bacteriological plates and into differentiation media. Representative images taken at D3 (A-C), D7 (E-F) and D12 (G-H). Stains shown are Tuj (A, D, G), CellTrackerTM Green ™ (B, E, H) and Merge with DAPI (C, F, I). Images taken on Leica Epifluorescent microscope with 50 μm scale bar. 117
Figure 32: A, quantification of cell directionality using the Fast Fourier Transform algorithm method, with cells grown on micro-HFs on day 3 (blue), on micro-HFs on day 7 (red) and on micro-HFs on day 12 (green). 2D planar controls are shown (black). (A) Directionality of NG108-15 cells. Data are normalized means to the largest frequency value ± SEM (N=3 independent biological repeats with 15 images analysed for each repeat). B, Absolute value of the orientation angle with respect to

the micro-HF axis for the highest frequency directionality peak for all conditions. N=3 ±SEM, Anova with Tukey's multiple comparisons was performed. 118
Figure 33: NPC neuronal differentiation on PX:PCL micro-HFs. Cells were seeded at 1,000,000/mL in Eppendorf tubes. After 24 hours they were transferred to square bacteriological plates and into neuronal differentiation media. Representative images taken at D3 (A-C), D7 (E-F) and D12 (G-H). stains shown are Tuj (A, D, G), CellTrackerTM Green TM (B, E, H) and Merge with DAPI (C, F, I). Images taken on Leica Epifluorescent microscope with 50 μm scale bar. 119
Figure 34: A, quantification of cell directionality using the Fast Fourier Transform algorithm method, with cells grown on micro-HFs on day 3 (blue), on micro-HFs on day 7 (red) and on micro-HFs on day 12 (green). 2D planar controls are shown (black). (A) Directionality of NG108-15 cells. Data are normalized means to the largest frequency value N=1 B, Absolute value of the orientation angle with respect to the micro-HF axis for the highest frequency directionality peak for all conditions. N=1. 120
Figure 35: A, quantification of SH-SY5Y cell directionality using the Fast Fourier Transform algorithm method after 12 days of culture, with cells grown on micro-HFs (blue), on micro-HFs with 0.3125% GG fluid gel (red) and 2D control (green). Data are normalized means to the largest frequency value N=3; B, Absolute value of the orientation angle with respect to the micro-HF axis for the highest frequency directionality peak for all conditions. N=3. 122
Figure 36: A, quantification of iPSC derived neuron directionality using the Fast Fourier Transform algorithm method after 12 days of culture, with cells grown on micro-HFs (red), on micro-HFs with 0.3125% GG fluid gel (blue) and 2D control (green). Data are normalized means to the largest frequency value N=1; B, Absolute value of the orientation angle with respect to the micro-HF axis for the highest frequency directionality peak for all conditions. N=1. 123
Figure 37: Phase contrast and CellTracker^{TM} Green of D12 Neuronal differentiation 2 days after the addition of gel. Image is not focused on the surface of the plate showing that some colonies of neurons detached but their neurite connections to each other remained in-tact. Scale bar – 250 μm 124
Figure 38: Scratch wound assay of differentiated SH-SY5Y cells., A, 2D control scratch assay, scratch was performed on D10 of differentiation. B, scratch was performed with 0.3125% GG fluid gel added on the cells to see effect on repair. C, scratch was performed with 0.3125% GG fluid gel added on the cells to see effect on repair, and 0.25% GG fluid gel was pipetted into the wound as the scratch was performed to mimic the mechanical differences in the spinal cord. Wound size was measured using ImageJ, N=3, Anova with multiple comparisons was performed. 124

List of Tables

Table 1: Major features of the three phases of a SCI (Oyinbo, 2011)……21

Table 2: Primary and secondary antibodies used for immunocytochemistry. Those frequently co-stained together are grouped together with red squares……..51

Table 3: Salt concentrations used to fabricate fluid gels……73

Chapter 1

1. Introduction

This Chapter comprises an introduction to the various relevant elements that would lead to the research question and aims of this thesis. Firstly, the physiology of the healthy spinal cord (SC) is discussed, with the aim to establish a basis of knowledge of the tissue from a functional and structural point of view. The different cell types present in the SC, as well as the extracellular matrix that constitutes their microenvironment are discussed (Section 1.1). This works focuses on the *in vitro* replication of the microenvironment of the SC after it has been damaged during a spinal cord injury (SCI); hence, the following section (Section 1.2) describes the causes and epidemiology of SCIs, as well as the implications of such injuries from a socio-economic point of view. Section 1.2 also includes a description of the biological and mechanical changes that occur after injury, which involves the formation of the glial scar. The management and current therapeutic options of SCI are discussed in Section 1.3. These are, to date, extremely limited mainly due to the complexity of the scar tissue and the lack of understanding of the biological and biochemical processes that underpin the formation and clinical progression of the glial scar. This leads to the need of developing better models of SCI, both *in vivo* and *in vitro*, which are reviewed in Section 1.4. There are two essential elements in *in vitro* models of tissues and hence in SCI *in vitro*/*ex vivo* models; namely a material/biomaterial component that replicates the extracellular matrix and environment, and a cellular component. These are the focus of Sections 1.5 and 1.6 respectively, with particular emphasis on induced pluripotent stem cells (iPSCs) in the latter.

1.1. Physiological aspects of the healthy spinal cord

The SC is a complex part of the central nervous system (CNS), linking the brain to the peripheral nerves attached to the cord (Silva et al., 2014). The SC is also able to produce certain spinal reflexes, which are capable of faster reactions times than reactions which are processed by the brain (Hultborn, 2006). The SC exists within the vertebral canal, extending from the brain through the cervical, thoracic, lumbar, sacral and coccygeal segments (Bican et al., 2013b) . Each segment after the first cervical segment has a pair of dorsal and ventral roots, as well as a pair of spinal nerves. These dorsal and ventral roots are where the afferent (sensory) and efferent (motor), respectively, enter the cord. These roots combine close to the cord itself to form the spinal nerves, one on each side (Bican et al., 2013b). These spinal nerves are described as one of 31 different levels, all linking with different anatomies and used for different functions, as shown in Figure 1. As can be seen in Figure 1, the cord extends from the brain at the medulla oblongata, where it then reaches the first vertebrae, represented in orange. Starting from the superior section and moving towards the inferior, there are 8 cervical (C) nerves, which are capable of receiving sensory input from the upper limbs and neck, whilst also providing control to the muscles and glands involved in the parasympathetic system, such as slowing heart rate, constricting airways and stimulate salivary glands (McCorry, 2007). Referred to as the ‘rest and digest’ system, the parasympathetic system controls normal homeostatic function when there are no external stress factors to deal with. Next there are 12 thoracic (T) nerves represented in green in Figure 1; these can receive sensory input from the trunk and control these muscles. Furthermore, there is control of the sympathetic system here with stress-related control of organs, for example increasing heart rate, dilating pupils and inhibiting food processing. Then there are the lumbar (L) nerves, these are

associated with the hips and lower limbs (shown in red in Figure 1), and also have stress functions related to the kidneys, bladder and genitals. Next is the sacral (S) nerves, these are linked with the lower digestive tract and the genitals. Finally, the coccygeal (Coc) these supply the skin covering the coccyx (Silva et al., 2014). These main features are highlighted in blue in Figure 1. The full length of the cord is around 450 mm in males and 430 mm in females, ranging from 13.3 mm diameter in the C5 region, down to 6.3 mm in the T8 region (Frostell et al., 2016).

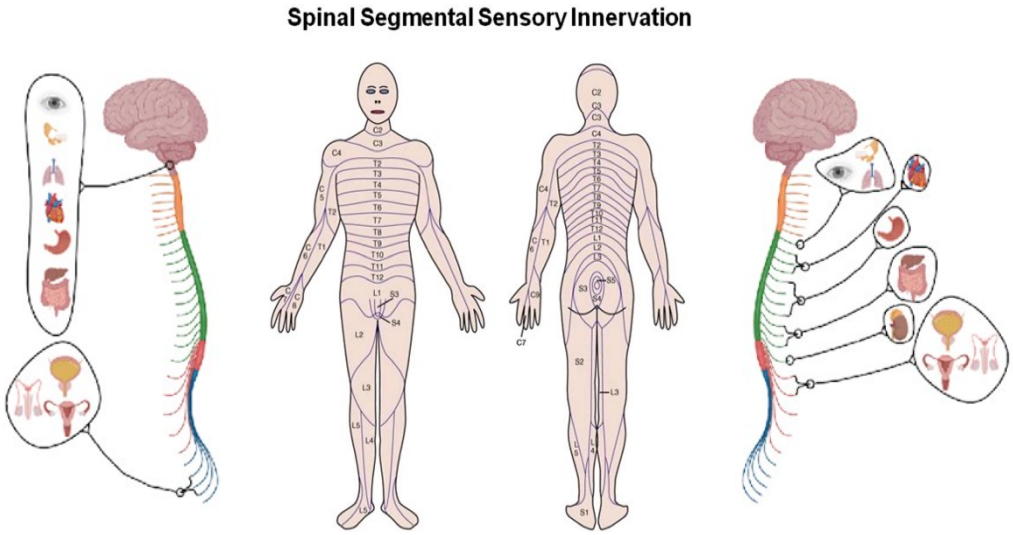

Figure 1: Anterior and posterior view of the spinal nerve sensory innervation (adapted from Bican et al., 2013). Diagram created using BioRender (www.biorender.com).

The cord itself is covered by connective tissue layers called meninges, similar to those found in the brain. These are the dura mater, arachnoid mater, and pia mater, going from the outermost layer to the innermost. The meninges help to provide a layer of protection to the delicate cord inside. Furthermore, there are spaces between the meninges, also there for protective purposes; the subarachnoid space, where cerebrospinal fluid resides between the arachnoid and pia, and the epidural space, where loose adipose and fibrous connective tissue reside between the dura and the

periosteum. Within these protective layers is the SC itself (Bican et al., 2013a, Silva et al., 2014). The SC is split internally and externally into the grey and white matter respectively. The segregation is due to a divide in the cellular microenvironment between the two areas. The grey matter is primarily made up of glial cells, interneurons, as well as parts of afferent and efferent neurons. These are further split, where the entering fibres of the afferent neurons are present, and the dendrites and cell bodies of efferent neurons are present. The white matter is primarily formed of bundles of myelinated axons. These fibre tracts run either ascending or descending transmitting information up to the brain, or down to the periphery.

The SC consists of many cell types, which have very specific roles within the healthy tissue and these change during damage to the SC and the surrounding tissues. The main electrically active cell type is the motor neurons. These have a variety of downstream targets similar to the connections of the sympathetic and parasympathetic nervous system (Figure 1). The motor neurons can be further split into two main categories, upper and lower. Upper originate from the cerebral cortex, while lower are situated in the brain stem and the spinal cord. The SC motor neurons exist in the ventral horn of the spinal cord, controlling the effector muscles in the periphery (Stifani, 2014). Beyond this there are a wide collection of glia which are present. These are mainly astrocytes, oligodendrocytes and microglia. Astrocytes make up between 20 and 40% of the cells within the whole CNS. They have complex structures which interact with almost all cells and structures within the CNS. These provide invaluable support to the cells and the tissue as a whole. They have vast controls of homeostasis in terms of the delivery and removal of solutes in the cerebrospinal fluid and neurotransmitters to support neurons (Gaudet and Fonken, 2018). Microglia are another cell present; these are the resident immune cells within the CNS making up

between 5 and 10% of the cells in the CNS. In a healthy environment, they have low levels of antigen-presenting machinery when compared with other immune cells, however, when activated this is vastly upregulated. Outside of their roles around the immune system, they also exhibit control in terms of CNS development and homeostasis. They interact with synapses, through a process called synaptic pruning, where they refine synaptic connections improving function, and removing unnecessary synapses (Hong et al., 2016, Gaudet and Fonken, 2018). Oligodendrocytes are another cell type present, with vital roles around myelination. They optimise the integrity of axons their structure and the action potential conduction. They extend many processes, making them capable of myelinating multiple segments concurrently.

In summary, the SC is a complex and essential structure within the central nervous system. Despite the various physiologically protective layers that encase it, the SC is susceptible to external damage, which is generally known as a SCI. The following section (1.2) describes the causes, incidence, and consequences of SCIs.

1.2. Spinal Cord Injuries

Traumatic SCIs occur when external forces act upon the SC through contusion, compression or severing which causes severe damage to the cells of the spinal cord. This can cause severe symptoms such as paralysis and loss of sensation and function below the point of injury.

In the UK there are around 18 new cases per million per annum (McCaughey et al., 2016). This accounts for both traumatic injuries, making up around 87% of these cases, and non-traumatic, such as tumours, making up the remainder. This equates to around

1,200 new SCIs in the uk every year (McDaid et al., 2019). The World Health Organisation (WHO) state that those most at risk are males (at a 2:1 ratio) in early adulthood (aged 20-29), and those in old age (over the age of 70), whereas in females are most at risk in adolescence (aged 15-19) and old age (over the age of 60) (WorldHealthOrganisation, 2013). Those who receive their injuries in their later life have significantly worse outcomes (Hachem et al., 2017).

The severity of the injury has a great impact on the patient in terms of clinical and personal factors. To begin with, whether an injury is complete or partial affects the extent to which function is lost below the point of injury. Complete injuries lead to a complete loss of motor and/or sensory function due to a full disconnect between the cord below and above the point of injury. The level or severity also depends on the location of the point of injury, with lower thoracic lesions leading to paraplegia, compared to the more severe quadriplegia resulting from upper cervical lesions (Wilson et al., 2012). This level of severity is measured on the American Spinal Injury Association (AISA) Impairment Scale (AIS). This scale grades injuries on a scale A-E, where E is classed as an uninjured, healthy spinal cord, and A is a complete loss of function below the point of injury. Patients are examined to determine where they fall on this scale. The standardised examination entails motor, sensory and anorectal examinations in order to define the severity of their injury (Roberts et al., 2017). Depending on the type of injury, the severity can also be altered. They can occur through many different actions, namely lacerations from stabbings or other sharp objects, and contusion or compression, mainly from blunt force trauma, road traffic accidents and falls (Silva et al., 2014).

Another consideration with SCIs is the risk of comorbidities associated. Chronic complications include cardiovascular, respiratory and urinary and bowel problems,

along with pressure sores (Sezer et al., 2015). Patients who suffer from SCIs are also at a higher risk of developing multi-morbidities, such as obesity, through reduced exercise opportunities, and depressive and anxiety disorders (Graupensperger et al., 2018). Other effects occur within the support network of patients; this can mean that family members or other caregivers give up time and possibly work opportunities in order to provide care (McDaid et al., 2019).

Along with the devastating impact of SCIs on patient's lives, there is also an immense cost. In the UK, the NHS is thought to spend up to £10 million in lifetime costs for SCIs, with the average around £2.5 million per patient. This equates to an overall £1.43 billion for new cases, with 71% potentially falling on public funding, and the remaining 29% due to reduced employment. These costs change depending on the severity of the injury and the age at which it occurs. For instance initial inpatient care costs are thought to be over £9 million for a tetraplegic, and down to around £1.5 million for a paraplegic (McDaid et al., 2019).

The mental health of SCI patients is a grave issue which was addressed in Migliorini et al. (2008). This study found that almost half of SCI patients suffered with depression, anxiety, clinical levels of stress and post-traumatic stress disorder. Additionally, of those SCI patients diagnosed with one mental health disorder, 60% had at least one other disorder. These levels are significantly higher than those seen in the general population (uninjured). The incidence of mental health issues is seen to be reduced when the health outcomes after the injury improve. This highlights the intricacies of the injury and how mental health is affected after serious health and life changes (Migliorini et al., 2008). Aside from the mental implications, there are also significant social impacts as a result of a SCI. For example, they cause significant interference to

recreational and physical activities, home maintenance, productive activities and sexual relations. This was found to worsen with increasing severity of the injury (Noreau and Fougeyrollas, 2000).

1.2.1. Biological and mechanical characteristics of injury – the glial scar

The neuropathology of a SCI encompasses a series of complicated events. The primary injury begins with the physical damage to the cord. This can occur through four main morphological actions: an impact with transient compression, an impact with continual compression, a dissection, and a transection or laceration. Injuriesare most commonly seen after road traffic accidents, falls and violence, such as blunt force trauma and stab wounds (Silva et al., 2014, DeVivo et al., 2002, Oyinbo, 2011). Of these morphological disruptions, the most common is impact with continual compression, where there is damage to the cord from burst fractures, with bone fragments putting pressure on the cord (Alizadeh et al., 2019). Here the injury can be either complete or incomplete, where the cord itself is severed or not respectively. Most injuries are incomplete, where there is some neurite connection across the site of injury (Tator and Fehlings, 1991). The secondary injury then follows after a cascade of biological processes, which cause worsening of the damage and new dysfunctions. The primary injury causes immediate, large scale cell death and haemorrhage at the site of injury, all of which contribute to the secondary injury cascade. Table 1 outlines the three phases of the biological response seen after the initial injury, where there is specific and overlapping phenotypes seen in the environment surrounding the injury and systemically. During the acute phase, the traumatic event breaches the structural thresholds that the body can cope with this in turn forces physical and biochemical modifications (Oyinbo, 2011). This onset of the secondary injury lasts from the initial

seconds to minutes after the injury, to weeks. The cells in the SC itself are damaged, causing necrosis, apoptosis, and secretion of chemokines. In 1911, it was first suggested that there were secondary injury characteristics seen after a SCI; this was first seen in dogs and then further theorised in the years after (Allen, 1911, Allen, 1914). This early research has been used as a basis for many findings, which have highlighted the importance of understanding the secondary injury, using this knowledge as a basis for treatments.

Table 1 highlights the acute changes that mark the start of the secondary injury, occurring from seconds to minutes after the initial injury. The vascular changes after injury are widespread, such as haemorrhage, vasospasm and thrombosis, as well as a loss of the regulation of these processes. One of the other issues involves the blood-spinal cord barrier (BSCB). The BSCB can be broken down, leading to infiltration of different inflammatory cells through the BSCB. All these vascular changes cause oedema, necrosis, and ischemia (Oyinbo, 2011, Silva et al., 2014, Popa et al., 2010). From a biochemical point of view, the neurotransmitter glutamate is excessively released after injury. As the major excitatory neurotransmitter in the CNS, this can lead to excitotoxicity, which causes direct damage to the tissues, as well as indirect damage through the production of reactive oxygen species (ROS). These ROS are then able to cause oxidative damage to lipids, membranes, proteins and DNA, all leading to cell death (Dumont et al., 2001). Furthermore, the salt balance in the neurons is affected, with $(Na^+ + K^+)$-ATPase function being impaired. This can lead to loss of neuronal function and tissue dissolution, further increasing the effects of the injury. The Na^+, K^+ and Ca^{2+} disruption causes depolarisation of cell membranes and increase intracellular Ca^{2+} concentrations, leading to cell death (Stys, 1998, Dumont et al., 2001).

Table 1: Major features of the three phases of a SCI (Oyinbo, 2011) Edited from Oyinbo (2011).

Primary/Acute (seconds-minutes)	Secondary/Sub-acute(minutes-weeks)	Tertiary/Chronic(weeks-years)
Systemic hypotension and spinal shock		
Vasospasm	Vasospasm	
Cell death from direct insult	Cell death from direct insult	
Ischemia	Ischemia	
Oedema	Oedema	
Derangements in ionic homeostasis	Derangements in ionic homeostasis	
Accumulation of neurotransmitters	Glutamatergic excitotoxicity	
Plasma membrane compromise	Plasma membrane compromise / permeability	
	Free-radical production	
	Lipid peroxidation	
	Nitrous oxide excess	
	Conduction block	
	Excess noradrenaline	
	Energy failure and decreased ATP	
	Immune cell invasion and cytokine release	
	Inflammatory mediated cell death	
	Neurite growth-inhibitory factors	
	Central chromatolysis	
	Vertebral compression/column instability	
	Demyelination of surviving axons	Continued demyelination
	Apoptosis	Continued apoptosis
	Initiation of central cavitation	Continued central cavitation
	Astroglial scar launch	Glial scar / syrinx formation
		Change in ion channels and receptors
		Regenerative processes, including sprouting by neurons
		Altered neurocircuits
		Syringomyelia

Research has now demonstrated that the CNS can no longer be considered an immunologically privileged region, but an immunologically quiescent region (Trivedi et al., 2006). It has been found that the CNS is able to mount a well organised immune response when challenged with injury and infection (Prins and Liau, 2003, Nguyen et al., 2002). The innate immune response becomes activated shortly after the injury occurs, with microglia, as well as neutrophils and dendritic cells infiltrating the parenchyma. These cells are then able to begin to attack any invading microbes present as well as phagocytose cell debris caused by the injury (Trivedi et al., 2006). Inflammation is an important factor in the prevention of effective repair and regeneration after SCI. The resident microglia in the CNS become activated. Microglia and non-parenchymal macrophages are mononuclear phagocytes which reside in the CNS. They have distinctive roles in which they interact with almost all the components of the CNS, where they make up around 5-10% of total brain cells. Microglia have a number of signalling pathways which can lead to activation, one of which is TGFβ-mediated, which occurs in many pathological conditions (Li and Barres, 2018).

If the BSCB is compromised, either by the injury itself, or by ruptured blood vessels, the area is also infiltrated by blood-borne neutrophils. These cells infiltrate within the first 30-45 minutes after injury, and after 3 hours, the production of TNF-α and interleukin-6 (IL-6) are upregulated around the damaged area. This TNF-α is thought to cause an increase in the glutamate-mediated cell death of neurons. As a consequence, TNF antagonists have been shown to slow and ultimately reduce the progression of inflammation associated with SCI (Esposito and Cuzzocrea, 2011). This strategy can be used to attempt to prevent the events of the secondary damage shown in Table 1. The vascular changes around the BSCB continue to develop, as well as the integrity of the barrier itself. Research has shown that, over time, the BSCB remains

compromised, but there is a gradual restoration linked to improved motile function (Cohen et al., 2009). Furthermore, the BSCB has been shown to be compromised following injuries not associated with the SC itself. Peripheral nerve injury in rats was shown to cause leakage of the BSCB, through a process that is independent of the activation of microglia in the spinal cord. This leakage was seen in the lumbar region and occurred after the spinal inflammatory reaction was started following the nerve damage. This study, by Echeverry et al., found that Monocyte Chemoattractant Protein-1 (MCP-1) was responsible for the permeabilisation reaction. This chemokine regulates the infiltration of monocytes/macrophages (Echeverry et al., 2011). In terms of the CNS, this protein is produced by microglia (Deshmane et al., 2009), but it also has a distinct role in SCI. Patients' serum levels have an increased level of MCP-1, which may have an impact on the induction of secondary responses in SCI patients (Liu et al., 2005).

Following severing of axons and damage to the extra-neural structure after a SCI, glial cells in the CNS change conformation and undergo gliosis, forming a glial scar. This scar tissue is composed mostly of reactive astrocytes, which become hypertrophic when triggered by blood leakage from the disrupted blood-brain barrier (Baumann and Pham-Dinh, 2002). The alignment of astrocytes is altered, and the extracellular matrix structure becomes disordered and dense (Watzlawick et al., 2016). The scar also contains a core of oligodendrocyte progenitors, fibroblasts and microglia that destroy cell debris and foreign material. The lack of regeneration in the CNS is mainly due to the inhibitory effects of the CNS extracellular environment (McDaid et al., 2019). The dense and complex structure of the scar is difficult for neurons to penetrate, and as the extracellular matrix is disturbed and the chemical cues guiding axon growth are lost, axons are unable to follow the correct pathway to restore their network (Yu and

Bellamkonda, 2001). Signalling factors such as chondroitin sulphate proteoglycans (CSPGs) are secreted by reactive astrocytes entrapping axons and preventing their extension past the scar (Bradbury et al., 2002). Axons collapse or follow the scar upon contact, which leads to random axon sprouting and loss of function when damage is severe (Watzlawick et al., 2016). Loss of expression of neurotrophic factors following damage, which are important for neural protection, contributes to this damage by enabling cellular atrophy (Plunet et al., 2002).

The complexity of both the glial scar microenvironment, and the biochemical and cellular processes within, constitutes a significant challenge in understanding the course of injury and trauma. These limitations hamper the search for potential repair mechanisms and the evaluation of effectiveness of novel therapeutic options. Innovative approaches for understanding the underpinning biological processes and testing therapeutic strategies are therefore essential. The damage caused, and the physical and biological scar formed all contribute to the lack of repair and regeneration of the SC itself. This thesis will focus on the mechanical properties of the scar, as this change in stiffness is likely to have an impact on the repair. Beginning with a mechanically relevant model allows for modifications to the microenvironment and the cells to answer questions surrounding the biological nature of the scar. The following section reviews some of the most recent innovative treatments, with particular emphasis on cellular therapies as this is where the field seems to be moving towards.

1.3. Current and novel treatments for spinal cord injuries

1.3.1. Gold standard clinical management strategies of spinal cord injuries

SCI patients go through life-long management of the condition. This usually begins with surgery occurring soon after to decompress and stabilise the injury. Furthermore, in this acute phase, other injuries tend to be present due to the reason for receiving a SCI (Sandean, 2020). Rehabilitation involves many passive exercises, these start early to prevent muscle wastage and joint stiffening. Beyond this muscle strengthening is one of the most important ways to allow independence. Alongside weight and resistance band training, electrical stimulation of the paralysed musculature can be used to prevent extreme fatigue (Nas et al., 2015).

1.3.2. Pharmaceutical approaches

Neuroprotective agents are used to help limit the progress of the secondary injury cascade. Riluzole is one of these drugs, it blocks Na^+ and Ca^{2+} ion channels, and prevents glutamate accumulation. This gives protection to the neurons during the acute phase of the injury (Meshkini et al., 2018). Granulocyte colony stimulating factor (G-CSF) is another alternative. This directs bone marrow derived mesenchymal stem cells to the site of injury in order to reduce apoptosis in neurons and oligodendrocytes. This protects the myelin and prevents some sub-acute phase cascades (Hiroshi Takahashi et al., 2012).

These are just some of the drug options available today which have promising effects on patients. They have limitations, as there are specific time frames when their mechanism of action is beneficial. Furthermore, they do not necessarily restore function, only prevent further injury occurring, so the natural repair mechanisms can work effectively. This is a reason for other therapies to be utilised, such as cell-based therapies.

1.3.3. Cellular therapies

Cell therapies are an emerging field, becoming more widespread in recent years with companies such as ReNeuron taking cell therapies all the way to a therapeutic product. Early work on cell therapies for CNS-related conditions began at the end of the 20th century. In 1998, Kondziolka et al. used human teratocarcinoma cells, taken from a 22-year-old male testicular tumour, which were then differentiated using a similar method to that for other neuronal cancer cell lines such as SH-SY5Ys. These neuronal like cells were then transplanted into the damaged portion of the brain after a stroke. This work was previously done in animal models where the cells were shown to be safe, and the implanted cells were seen to form functional connections with the native cells in the tissue. In the animal models, as well as in the human trials, some improvement in the motor function were seen, along with the function along the European Stroke Score in some of the participants (Kondziolka et al., 2005, Kondziolka et al., 2004, Kondziolka et al., 2000). This shows the promising results which can be seen from cell transplants to treat CNS-related conditions with extremely limited treatments and assess potential for rehabilitation. Since then, work has branched out from stroke to other CNS conditions, such as SCI. There are multiple theories as to

how the use of cell transplantations could help with recovery after a SCI. This includes three main factors (Pearse and Bunge, 2006, Li and Lepski, 2013):

a) The secretion of multiple neurotrophic factors at the site of injury, which could improve regeneration. These are thought to be useful to prevent secondary damage but only within the first hours after the injury occurred (Kwon et al., 2011). When transplantation is performed in the days after injury it can improve the chance of graft survival (Tetzlaff et al., 2011), there has still been an association with a reduction in necrotic and apoptotic death, along with other factors involved in secondary injury formation as seen in Table 1, preventing the injury worsening. This is seen in situ through imaging the lesion, where it is possible to see the amount of white matter spared. Subsequently, there is unknown methods which prevent ongoing damage to oligodendrocytes. These cells continue to go through apoptosis through chronic timepoints (Almad et al., 2011). Loss of oligodendrocytes causes demyelination (Assinck et al., 2017), in turn disturbing axonal function and neuronal survival. Around two weeks post injury, oligodendrocyte precursors, begin to differentiate and remyelinate demyelinated axons. This works to try to reduce the amount of damage, but it is not sufficient (Almad et al., 2011).

b) Introducing cells which could provide support, as well as a scaffold for the regeneration of pre-existing cells. Native cells can help to produce healthy extracellular matrix (ECM) proteins and are able to normalise the extracellular environment within the lesion. Additionally, the introduction of cells can provide a support structure for infiltrating and regenerating cells to grow along, allowing for increased efficiency of cellular regeneration. There is also evidence that the

transplanting of oligodendrocytes and Schwann cells around the site of injury is beneficial due to their myelination activities (Almad et al., 2011, Lankford et al., 2002).

c) Replacing lost neurons or neural cells which could be used to improve function. Due to the length of the motor neurons of the spinal cord, regenerating them is not always possible. The implantation of neurons, or stem cells such as neural precursor cells (NPCs), which are able to differentiate into neurons, could allow for a bridging of the gap caused by the trauma. This has been shown to increase some levels of functionality below the point of injury in both animals and humans (Sreenivasa Raghavan Sankavaram et al., 2019).

Early work around cell transplantation for SCI not only used neural cells, but cells from different areas of the body. Examples of these were adult stem cells from umbilical cord blood (Kang et al., 2005), and also olfactory ensheathing cells (Huang et al., 2003). These studies, conducted in the mid-2000s, were met with scepticism as they did not link with other research done at the time, as well as the ethics surrounding the studies (Dobkin et al., 2006, Curt and Dietz, 2005, Li and Lepski, 2013). To this day, these results have not been replicated in clinical trials, which further brings the science presented into question.

1.3.3.1. Oligodendrocyte Precursors

SC oligodendrocytes myelinate mature neurons. There are slightly different subcategories of oligodendrocytes in the SC compared to the brain. In the SC, they

differentiate from motor neuron precursors into oligodendrocyte precursors. They then are able to begin differentiation to form fully mature myelinating oligodendrocytes. The process of myelination is highly regulated. Oligodendrocytes select axons with a diameter above 0.2 μm, along with other molecular cues which are unknown (Simons and Trajkovic, 2006). The onset of myelination seems to be started by the differentiation of neurons (Brinkmann et al., 2008), and their electrical activity (Gyllensten and Malmfors, 1963). There is evidence as early as 2005 that embryonic stem cell-derived oligodendrocyte precursor cells being transplanted into the injured SC could have an enhancement effect of remyelination and improve motor function in rats (Keirstead et al., 2005). As some intact axons can lose their myelin sheath due to the death of oligodendrocytes at the point of injury and beyond (Utzschneider et al., 1994), the introduction of new oligodendrocytes could help recover these demyelinated cells (Totoiu and Keirstead, 2005). A meta-analysis of this type of cell therapy in rat models has shown that there is a significant increase in the motor function and the myelination of axons, as well as a reduction in the cavity size (Fu et al., 2018). Cell therapies show great promise as treatments for these types of injuries.

In the injured SC environment, there are many factors present which are detrimental to the health of oligodendrocytes. The surrounding cell death from both apoptosis and necrosis releases a plethora of proteolytic enzymes, many of which are detrimental to the structure of the cells and the vessels supporting the oligodendrocytes. This can cause increased blood vessel leakage, in turn leading to more apoptosis and necrosis. These factors are also able to inhibit the proliferation and migration of oligodendrocytes, reducing their effectiveness in regeneration (Juliet et al., 2009).

1.3.3.2. Mesenchymal Stem Cells

Mesenchymal stem cells (MSCs) are a cell type easily isolated from multiple sources. The most widely utilised MSCs are obtained from the bone marrow, but they are also present in adipose tissue, and incord blood and placental tissue. The isolation of MSCs involves minimal ethical concerns, as they can be isolated from volunteers to form a bank, as well as from the patient for autologous transplants. These cells are then able to differentiate into their standard three lineages of the adipo-, chondro- and osteo-, as well as some smooth and striated muscle. An important role in their use as a cell therapy is their immune modulation features. They have an array of secreted soluble factors which limit the immune cell response. This is extremely important in SCI due to the damage cause by the secondary injury through the unresolved inflammation (Pittenger et al., 2019). The transplantation of these cells in controlled animal models seemed promising. However, when these types of cells were translated into human clinical trials, the results seem to be underwhelming. Although the transplants appeared to be safe, the results did not match expectations (Cofano et al., 2019).

1.3.3.3. Neural Precursor Cells

Neural Precursor Cells (NPCs) are the adult stem cells present in the brain. These were only relatively recently discovered in the CNS, highlighting the possibility for regeneration and recovery of CNS damage such as after SCI (Johansson et al., 1999). These cells are producing new functional neurons and CNS cells, and they are thought to be part of the mechanism for memory, learning and olfaction (Ming and Song, 2011). They have also been shown to have regenerative effects on SCIs. Evidence of their success is the inhibition of apoptosis in the cells residing in the spinal cord. This was

seen in experiments utilising conditioned media as a treatment, showing that the secretome of NPCs is of vital importance (Kim et al., 2022). This brings into question whether the transplant of cells is necessary, beneficial or the safest option. If the secretome could be upscaled, purified and used as a stand-alone therapeutic option, this could be the safest and most effective way to treat a plethora of conditions in the CNS, not just traumatic injuries (Pinho et al., 2020). NPCs were also shown to be able to migrate from the site of injury, allowing for a comprehensive regeneration around the injury as well as within (Boido et al., 2009).

After evaluating the literature, with regards to the cellular and non-cellular components within the SC and SCI, it is evident that there are many aspects of the three-dimensional microenvironment within the glial scar that are currently unknown. This gap in knowledge dramatically hinders the development of new treatments that can either alleviate the life-long consequences of SCI or provide a definitive regenerative option. iPSCs are widely used as a platform to model disease in the CNS, including the blood-brain barrier, primarily in monolayer culture or as 3D organoids. They are also being tested as potential therapies for SCI with various degrees of success. Most importantly, there are, to date, no existing *in vitro* models of the glial scar that recapitulate the complexity observed *in vivo*. The insights from this thesis could improve the research and development of novel therapeutic agents, including cellular therapies, as the platforms developed here will be more representative of the human specific injury and model possibilities, whilst simultaneously reducing the use of animals.

1.4. *In vivo* and *in vitro* models of trauma

Traumatic brain injury (TBI) and SCI are huge causes of disability and death. The use of modelling systems is paramount in the discovery of the mechanisms behind the pathology, as well as finding novel treatments to improve prognosis. This section will discuss the most commonly used animal models in research, as well as novel *in silico* and *in vitro* models of SCI. *In vitro* modelling of SCI would allow for a humanised system, mimicking the cellular structure of the spinal cord.

1.4.1. Animal models

Animal models of the CNS generally use pharmacological, mechanical trauma and mechanical interventions amongst other things to incite SCI. In general, these models can be good indicators of the success of drugs and treatments, as well as the discovery of the mechanism of action of such therapeutic molecules. Animal models can then be compared to observations made in humans, especially to discover the basics of the disease, and to discover treatments for symptoms (McGonigle, 2014). Although these models provide a good baseline to be transferred into humans, many studies that have been successful in animals have had disappointing results when transferred to human trials. When looking at the broad literature for different types of interventions, no clear treatment has emerged. However, small scale clinical trials seem to be moving from academic researcher-led trials into company profit-based trials, allowing for more rigorous testing to take place, and later stage trials to commence (Yamazaki et al., 2020, Srinivas et al., 2019).

There is a significant number of animals used in an attempt to discover new treatments for SCI, leading to animal suffering. Lilley et al. (2020)investigated the welfare issues associated with this facet of research, finding that animals were put through undue stress, pain and discomfort. They found that there were areas in which this could be reduced through better communication between researchers and groups, as well as through improvements in training (Lilley et al., 2020, Carbone, 2011). Meta-analysis has shown that most models of SCI are undertaken in rats, with thoracic region and contusion injuries being modelled most often. This meta-analysis looked at 2209 studies, with no definitive number of animals stated, this is thousands of animals (Sharif-Alhoseini et al., 2017). Furthermore, the methods to inflict these injuries are attempting to recreate the damage caused by traumatic injuries observed in human often as a result of road traffic accidents. AS such, 62% of studies use blunt force trauma to induce injuries in the animals. Herein lies a large amount of suffering to the animals, with a majority of these injuries being inflicted by weight drop or an impactor (Sharif-Alhoseini et al., 2017). The introduction of reliable *in vitro* models could reduce the number of animals used in this type of research drastically.

The use of animal models has a distinct set of advantages and disadvantages which cannot be ignored. The main positive is that it is a full system, meaning that the interactions from the rest of the body can be studied (Lucia Slovinska et al., 2015). Whole animal studies are a requirement to see full system safety, outcomes, and responses. However, if at least some of the early testing can be done *in vitro* then this could reduce the number of animals used and the suffering caused drastically. An *in vitro* model of the spinal cord, which can be damaged artificially in a similar manner, could be a high throughput, animal free, testing platform.

Although the use of *in vitro* and *in silico* models is not yet up to the standard of animal models, there are certainly ways in which animal suffering could be minimised.

1.4.2. In silico Models

At present, there are limited *in silico* models available for SCI. Amongst the reasons for this are the complex nature of the condition, with the lack of full understanding of the true cellular and molecular mechanisms involved. As well as this, there are a wide range of types of SCI with varying degrees of deformations, severity and prognoses. Those that do exist are in their infancy with limited usage or usage around the spine and spinal loading, rather than a direct link to damage, repair and recovery (Cazzola et al., 2017, Moraud et al., 2016, Franco Woolfe et al., 2007, Lilley et al., 2020, Ziraldo et al., 2015)

1.4.3. Ex vivo models

The use of organotypic or slice cultures of the spinal cord allows for the complexity to be maintained, whilst increasing throughput per animal, as multiple slices can be taken per spinal cord. These slices can then be cultured and damaged in order to see cellular responses, and test therapeutic approaches (Lucia Slovinska et al., 2015, Patar et al., 2019). Furthermore, work has been done in slice models utilising a post injury SC, and slicing and culturing this. This has the benefit of having the biological nature of the scar, with the intrusion of cell types for study *ex vivo.* These slices are a useful tool in order to see the complexity which exists within the tissue, and to test potential therapeutics (Patar et al., 2019). These models still come with the ethical

considerations as an *in vivo* model, but allow for different observations which are more difficult *in vivo*.

1.4.4. In vitro Models

Although there has been more work in the field of *in vitro* models of SCI, they are still far behind what we see in animal models (Lilley et al., 2020). With the surge in 3D modelling on almost all human organs, especially with the use of induced pluripotent stem cells (iPSCs), research groups are getting closer to a usable model of the SC and injury (Weightman et al., 2014, Lobenwein et al., 2015, Yu et al., 2019). However, the complexity of the tissue itself, and furthermore, of the injury, is a tall order to effectively recreate *in vitro*. The unique combination of cell types seen in the spinal cord, neurons, astrocytes, microglia, oligodendrocytes etc., can all be effectively differentiated from iPSCs, allowing for the possibility of a complex human SC to be modelled (Hong and Do, 2019, Walczak et al., 2021).

An *in vitro* model could allow for a higher throughput screening process, Here, NG108-15 cells and SH-SY5Y cells are used as a quick and cheap cancer derived cell model. These cells are fast growing, and are able to extend neurites which can be then used to assess repair and regeneration (Maeda et al., 2021, Huang et al., 2022). These both have their drawbacks, with NG108-15s being a rodent hybrid line, this comes with problems of species variability and the fact that they are not a real cell type which exists in the body (Cargill et al., 1999, Liu et al., 2012, Maeda et al., 2021). Alongside this, SH-SY5Y cells are human, but they are still a cancer line, which had metasizised to the bone marrow (ATCC, 2022). They can be differentiated towards a more neuronal phenotype, which has been accepted for use in the field for many years (He et al., 2018, Sang et al., 2016). Beyond this, the use of human iPSC derived cells will allow

for a more translational model system, which will allow for accurate testing of potential treatments and mechanisms (Nagoshi et al., 2020).

The 2D modelling in use focusses around scratch wound assays on primary cultures (Lucia Slovinska et al., 2015). These are useful, but they lack the 3D nature of the spinal cord and injury. Being able to transfer a scratch like wound to a 3D model, with a similar mechanical structure would allow for better assessments of repair and regeneration.

1.5. Biomaterials in Tissue Engineering

1.5.1. Introduction

Recent advances in biomaterials have led to their growing use in *in vivo* and *in vitro* work for tissue regeneration purposes. By creating materials with different properties in terms of their stiffness and topography, these can be used to mimic, replace and repair many biological structures (Fuhrmann et al., 2017). Their tuneable properties allow for more accurate recreations of the *in vivo* environment, allowing for the development of more accurate models and better treatment methods. The uses of biomaterials are broad, ranging from scaffolds to mimic the *in vivo* environment, to encapsulation of drugs or cells for targeted drug delivery (Li and Mooney, 2016, Hunt and Grover, 2010).

1.5.2. Types of Biomaterials Used for SCI modelling

Biomaterials span a range of different materials with various properties, structures and applications. They can be fabricated as fibres, sheets, gels, porous matrices, in liquid or solid form, and used as combinations to complement and add a multitude of chemical and physical features. These can be used in the body to aid certain treatments, such as drug delivery vehicles, or to provide the scaffolding to replace body parts, such as hip replacements. These, amongst countless other applications, make up the discipline of Biomaterials Science. For the purposes of SCI repair, there have been multiple different biomaterials tested to determine their effectiveness for regeneration (Busch and Silver, 2007). One of these scaffolds is fibres that can be added into the SC to help guide the axonal regeneration, along with other therapies such as conventional drugs or cellular therapies as mentioned in Section 1.3.3. Their main function is to guide and support regrowth and maturation of the neurons within the injury. These fibres can be made up of several different natural or synthetic polymers, each providing different properties, such as stiffness, biocompatibility and biodegradability (Hurtado et al., 2011, Yao et al., 2012).

1.5.2.1. Hydrogels

Hydrogels are hydrophilic polymer networks which encase high volumes of water, usually formed of a variety of different monomers (Ahmed et al., 2013). There are varying types of these lattice structures, each with different functionality, gelation mechanisms and rheological properties. These properties allow for diverse uses, where specific criteria will be suited for individual hydrogels. They are also able to be functionalised by binding specific proteins such as collagen and laminin within the gel

to allow for a better environment for cells to be seeded and grown (Ahmed, 2015). A wide range of monomers can make up the hydrogel, resulting in different classifications. Homopolymeric hydrogels are gels formed of a single repeating monomer, which creates a relatively simple, repeating structure (Iizawa et al., 2007, Ahmed, 2015). Further complexity is reached when adding more monomers into the structure; copolymeric hydrogels are formed of two or more monomers, where at least one of them is hydrophilic, allowing for the “hydro” element of the gel. These monomers can be arranged in any format, whether they be in block, alternating or random configurations to form the polymer network (Yang et al., 2002, Ahmed, 2015). Beyond this, there are multipolymer interpenetrating polymeric hydrogels (IPN), which consist of at least two independently crosslinked hydrogels contained within a network. These allow for a higher level of customisation of the properties. By carefully selecting each of the polymers, and adjusting their relative concentrations, it is possible to create highly customised and controlled hydrogels (Zhai et al., 2000, Ahmed, 2015).

Beyond their composition, hydrogels can be further classified by their structures, with them being amorphous, semi-crystalline and crystalline. In addition to this, the way in which their crosslinking occurs to form this structure is used to classify them, whether this be chemically or physically. Chemically crosslinked hydrogels have permanent bonds, often times covalent bonds, while physical networks have more temporary bonds, such as hydrogen bonding, ionic bonding and hydrophobic interactions (Ahmed, 2015). Beyond this, there are a variety of more specific and nuanced classifications which can be applied to hydrogels, allowing for an incredible amount of detail in the understanding of individual gels, their properties and their uses.

Hydrogels can be introduced into the SCI, are able to support the surrounding network and can also introduce cells, drugs or other small molecules and proteins into the site of injury (Hiemstra et al., 2007a, Hiemstra et al., 2007b). These gels can also be used to mimic the mechanical microenvironment of the body more readily than TCP, such as for SCI (Picollet-D'hahan et al., 2016, Ahmed, 2015, Skardal et al., 2013).

1.5.2.2. Fluid gels

Fluid gels are a form of hydrogel formed through the shearing of a solution capable of becoming a hydrogel during the gelation process (Garrec and Norton, 2012). This causes pockets of hydrogel to form separately from one another and be dispersed at a high concentration in liquid (Shahrizan et al., 2022). A reversable solid is created, able to have viscoelastic properties, causing it to alter its properties depending on the forces placed upon it (Chouhan et al., 2019). These non-Newtonian fluids are therefore useful for their ability to be pipetted into precise locations, whilst retaining their viscoelastic properties. These properties also allow for the fluid gels to self-heal. This is a useful feature which can be utilised by introducing another gel structure within the fluid gel, which has different mechanical properties. In doing so, a more complex model can be created, using multiple mechanical stiffnesses alongside each other, to better mimic specific physiological locations (Talebian et al., 2019). Another benefit of fluid gels is the amount of diffusion which they allow. As they are not a true solid, their fluidic structure allows for the diffusion of molecules throughout. This can be a great benefit for *in vitro* models as it allows cells to be effectively and efficiently fed, providing the nutrients and extracting the waste in a system better than a solid hydrogel with similar mechanical properties. Conversely, the slower rates of diffusion seen in hydrogels,

specifically more densely structured ones, can support gradients throughout the gels (Amsden, 1998, Lühmann and Hall, 2009).

1.5.2.3. Drug Delivery

Similarly to how the structure of hydrogels and fluid gels can be used to help or hinder diffusion, they can also be used for drug delivery purposes. Gels can be finely tuned with specific therapeutics or active compounds embedded or encapsulated within them, in order to have controlled release in models or in a therapeutic setting (Jiang et al., 2014, Amsden, 1998). These compounds can be bound to the gel itself, embedded within a hydrogel or gel particulates in fluid gels. Many different factors, particularly growth factors such as BDNF and NGF for CNS regeneration have been used with varying degrees of success (George et al., 2020).

1.5.2.4. Scaffolds

Biomaterial scaffolds allow for cells to be grown in specific formations based around the scaffold they are grown on; this is controlled by the topography, surface chemistry, shape, and other physicochemical factors. Scaffolds have countless uses in life sciences research, and they play a key role in SCI modelling. They began being used to provide a surface for axonal growth and regeneration, bridging the gap in the lesion, with many different scaffolds being tested as potential treatments (Elliott Donaghue et al., 2014, Liu et al., 2013). Scaffolds themselves can be categorised, similarly to hydrogels as discussed in Section 1.5.2.1. These classifications include the types of polymers that form them, natural, synthetic biodegradable and synthetic non-biodegradable. Each has benefits and drawback depending on the intended

application. Natural and biodegradable polymers allow for the scaffold to be introduced and then be absorbed by the body. Natural polymers have cellular binding sites, improving adhesion, whilst also having the benefit of limiting the immune response when implanted. This can be partially overcome by coating synthetic polymers with proteins such as laminin to have similar effects. Furthermore, synthetic polymers are more consistent and tuneable when compared with natural polymers. Overall, each has its use, and thrives better when considering different applications (Katoh et al., 2019).

1.5.2.5. Micro-Hollow Fibres

Biomaterials can be fabricated via different methods, depending on their desired functionality, structures and characteristics. Polymeric hollow fibres in the micro scale have been produced by many methods, one of which is by phase inversion single-orifice spinneret (wet spinning). This was first done by Yao et al. (2012), and later improved upon by Vilinhas (2019). Contact with water allows the fibres to solidify by removing the solvent in which the polymers are dissolved, before being transferred to hot ethanol. This later part of the process extracts the oil in the formulation, causing the fibre to become porous. These fibres also have an added topographical difference; they present striations along the surface of the fibres, which are parallel to their length. This can be exploited to cause alignment of cells along the fibres. Uses for this involve modelling the SC and the peripheral nervous system (PNS), and for other tissue engineering applications. Fibres can also be produced by electrospinning. These fibres are much smaller, in the nanometre range, and tend to be used for 3D scaffolds rather than as a surface for cell growth. These are created by extruding through a needle, after which the polymer solution is electrospun in an electrically charged area, with a

constant voltage (Liu et al., 2006). These mesh structures have been proven to aid attachment and orientation of OECs, which again could be used for implants into the SC and other areas of the body (Kueh et al., 2012).

1.5.2.6. Mimicking the spinal cord and spinal cord injuries

The SC is an extremely soft structure, with the Young's modulus in the range of 200-500 Pa for the healthy SC and 50-200 Pa after injury (Moeendarbary et al., 2017). Structures this soft are difficult to mimic *in vitro* and finding the appropriate materials that have these mechanical properties limits their usability (George et al., 2020). Furthermore, mimicking the glial scar adds to the complexity, as the stiffness reduces. The formation of the scar then acts as a barrier to regeneration exacerbating the dysfunction (Fitch and Silver, 2008). It is hoped that overcoming permanent damage to the CNS could be achieved by utilising specifically engineered microenvironments which can kickstart and aid regeneration (Sachs et al., 2017).

Depending on the gel/polymer to be used to recreate the microenvironment, there are a number of methods capable of fine tuning the mechanical structure of the material. The simplest way is through the concentration of the polymer in the gel. Increasing the concentration usually results in thickening and stiffening of the hydrogel formed. Supporting that, increasing the crosslinking of the polymers, whether via increased concentration of salts (which act as cross-linkers), radiation or another method, to set the gel, likely leads to a stiffer gel being formed (Ahmed, 2015).

Once the desired stiffness is achieved, the specific spatial distribution of elements within the SC becomes the next barrier. The SC has a specific cellular structure, with

the orientation of the cells being a major part of the function. The motor neurons of the SC are the longest cells in the body, with lengths of up to 1 m, and this morphologyis one of the reasons why they are able to perform their function (Linderoth and Foreman, 1999). Recreating this level of organisation *in vitro* comes with many complications as cells do not generally grow in controlled directions in tissue culture plastic in planar cultures. *In vivo*, cells are directed by chemicals and their gradients, mechanical cues and electrical stimulation. Each of these and more can be utilised *in vitro*. Chemokine gradients are useful to direct the migration of specific cell types towards or away from areas of choice. Furthermore, it is possible to direct cells in 3D with the use of hydrogels as a medium to hold and disperse these factors (Amsden, 1998, Shallard and Mayor, 2020).

Mechanical cues have a dramatic effect on the SC from development through to regeneration potential. During development, mouse and Xenopus SC cells have different migration and proliferation rates due to the mechanical stiffness of the ECM which they are attached to (Barriga et al., 2018, Shallard and Mayor, 2020, David E Koser et al., 2016). The mechanosensing of neural cells axons has been studied, with evidence emerging that a mechanical stiffness gradient, without any chemical cues is enough to direct axonal outgrowth. Axons preferentially grew towards softer substrates, and when mechanosensors were blocked, this phenotype was lost and brain development became abnormal (David E Koser et al., 2016). In addition to migration, neural precursor cells are known to have altered differentiation depending on the stiffness of the substrate which they are attached to. They favourably differentiate to neurons on softer substrates and to glia on stiffer substrates (Kothapalli et al., 2020).

A complete *in vitro* model does not only require the various biomaterial-based elements that constitute the extracellular microenvironment, but also, and very importantly, cells that populate and grow in such environments. The following section will discuss the use of stem cells in particular, and their potential as biological tools to recreate tissue *in vitro*.

1.6. Stem cells for *in vitro* modelling

1.6.1. Introduction

A stem cell is defined as a cell which is able to self-renew and differentiate into one or more cell types. Induced pluripotent stem cells (iPSCs) are a type of cell which have been artificially reverted into their early embryonic state (Zakrzewski et al., 2019). These cells, under the correct conditions are able to be differentiated into any cell in the body. This process, discovered in 2007 by Takahashi et al, has altered the way in which human *in vitro* models can be formed. The first methods of reprogramming used lentiviral and retroviral transduction of human fibroblasts focusing on what are now call the 'Yamanaka factors'. These transcription factors, Sox2, Oct4, c-Myc and Klf4, essentially reprogramme the cells into a naïve embryonic like state (Takahashi et al., 2007, Yu et al., 2007). Since this discovery, the process has been tweaked, using episomal and mRNA as the strategy for reprogramming, which tends to have a lower footprint than that of viral methods, meaning the genome is unaffected (Malik and Rao, 2013).

This technology has created a boost in human *in vitro* models. As more efficient reprogramming and differentiation methods are being discovered, models are

increasing in complexity and specificity, including CNS models (Zahumenska et al., 2020). This became more prominent after Chambers et al, in 2009, differentiated human iPSCs (hiPSCs) into neural cells through dual SMAD inhibition. This involved inhibiting the SMAD pathway, a downstream target of the transforming growth factor-β (TGF-β), through the inhibitors Noggin and SB431542. This was then updated by Shi et al. in 2012, where they found alternative small molecules which decreased variability in the NPCs formed (Chambers *et al.,* 2009; (Shi et al., 2012)

Aside from the scientific benefits of iPSCs, one of the main ways which they have progressed the field rapidly is the ethical debate around other methods of modelling. Ethically sourced iPSC-derived models have some of the most accepted ethical considerations when compared to embryonic stem cells, for example.

1.6.2. Neural Precursor Cells

NPCs are the stem cells found in the brain, arising from the neural tube; this can be seen *in vitro* with the neural rosette formation. These cells are able to form the main neural and glial cells in the CNS (Hong and Do, 2019). NPCs were first isolated in 1989 from embryonic rat forebrain (Temple, 1989) where they challenged the idea that no new neurons were differentiated after development. These NPCs have been used extensively in *in vitro* modelling and in stem cell transplants (Hong and Do, 2019). Their uses have been broad, with work done on seizure (Alastair I. Grainger et al., 2018), autism (Gordon and Geschwind, 2020), Alzheimer's disease (Penney et al., 2020) and many more. These cells have opened up the possibility for *in vitro* modelling to be carried out, not only in 2D but in 3D as well. Many 3D models utilise the iPSC derived cells to create 3D CNS models, such as the cortex. A similar differentiation protocol is

conducted in 3D to produce electrically active cortical organoids which can be used for healthy or diseased models (Gordon et al., 2021). This technology has a wide range of uses, both in 2D and in 3D modelling, with 3D modelling better mimicking the structures seen *in vivo*.

1.6.3. iPSC-derived motor neurons

The use of iPSC derived motor neurons tends to be focused around the modelling of motor neuron disease. These have the potential to electrically, structurally, and morphologically mimic the phenotype which is seen *in* vivo, both in healthy and diseased patients, through the use of disease lines and then can be compared with isogenics. Much work has been carried out in 2D and 3D, utilising iPSC models to assess the pathophysiology of the disease. Similar methods can be used within SCI as the cells undergo the same differentiation pathway (Alexandra E Johns and Maragakis, 2022). These cells are a vital addition to the field of the SC research, for injuries and the diseases surrounding the tissue.

1.7. Conclusions and gaps in knowledge

This review of the literature has explored the SC physiology, what are the biochemical, mechanical and cellular changes after injury, the current treatments and the modelling strategies currently in use. The *in vitro* modelling of the SC is incredibly limited, with very basic models having problems in terms of how well they are able to mimic the environment of SCI. Current models tend to focus on the role of astrocytes in the glial scar, whilst not seeing how motor neurons can be repaired and regenerated in order

to return function to patients (Spencer et al., 2017, Wanner et al., 2008, Fang et al., 2019).

This gap in the knowledge, together with the complexity of the injury, leads to several exciting scientific questions which can be addressed through the use of biomaterials, such as those explored in this review; micro-hollow fibres for cellular alignment, fluid gels for their mechanical properties of the glial scar and iPSC derived cells as the human cellular component that is required in an accurate model.

Chapter 2

2. Aim and objectives

The mechanical properties of healthy and injured spinal cords in animals have been measured previously in the literature using atomic force microscopy. The results have shown that the glial scar is approximately an order of magnitude softer than healthy SC tissue, with Young's Moduli of 50-200 Pa versus 200-500 Pa respectively (Moeendarbary et al., 2017). For context, the Young's Modulus of tissue culture plastic is estimated to be more than 100 times larger than these values (Skardal et al., 2013), indicating the unsuitability of monolayers grown in traditional flasks for modelling CNS tissues. This drop in stiffness changes the mechanical and structural microenvironment, leading to changes in cellular processes. For example, studies have shown that neural precursor cells (NPCs) preferentially differentiate down the neural lineage on a mechanically soft substrate when compared to a mechanically stiffer substrate. Additionally, precise location of motor neurons (a predominant cell type in the spinal cord) is essential for their functional input and output, and their migration is regulated by axon guidance cues. The literature shows that generally motor neurons are aligned and static in the spinal cord (Alizadeh et al., 2019). This is very difficult to reproduce *in vitro*, unless a scaffold is used.

iPSC technology is at the forefront of *in vitro* modelling, this thesis utilises iPSC derived CNS cells. iPSC technology addresses the limitations of other cell types, as iPSCs are able to generate a range of CNS cells from both healthy and diseased donors. Alternatively, iPSC-derived Neural Progenitor Cells (NPCs) present an ideal source of cells for CNS modelling, despite their narrower differentiation capacity.

This project aims to use human induced pluripotent stem cells in combination with biomaterials to generate a physiologically relevant model of the spinal cord and the glial scar that forms after a spinal cord injury.

The specific objectives to achieve the aim of this thesis are:

1. **Assessment of the structure, mechanical properties, permeability, and surface topography of newly fabricated micro-hollow fibres to determine their suitability for cell culture in *an in vitro* model of the SC/SCI.**

2. **Optimisation of the formulation and fabrication methods of gellan gum fluid gels based on their rheological properties to mimic the mechanical properties of the extracellular matrix in the spinal cord as seen in the literature.**

3. **Optimisation of the 2-dimentional growth and differentiation potential of neural cell lines and iPSC derived neural precursor cells and neurons, coupled with the study of the biocompatibility and toxicity of the biomaterials on 2-dimensional cell cultures.**

4. **Assessment of the suitability of micro-hollow fibres to facilitate cell alignment and differentiation of neuronal cell lines and iPSC-derived neurons and the quantification of such alignment.**

5. **Incorporation of mechanically relevant gellan gum fluid gels surrounding the 2-dimensional cultures and the micro-hollow fibres and quantification of their effect in terms of alignment and wound closure/migration in a mechanically relevant environment.**

There are many aspects of the three-dimensional microenvironment within the glial scar that are currently unknown. This gap in knowledge dramatically hinders the development of new treatments that can either alleviate the life-long consequences of SCI or provide a definitive regenerative option. Most importantly for this thesis, there are, to date, no existing *in vitro* models of the glial scar that recapitulate the complexity observed *in vivo*. This thesis aims to mitigate the current challenges within the field.

Chapter 3

3. Materials and Methods

3.1. Cell culture

3.1.1. Cell Lines

All cell lines were purchased with certificates of analysis showing they were mycoplasma free. Pluripotent stem cell lines were purchased with a normal karyotype and only used for a maximum of 8 passages.

3.1.2. Cell culture surface preparation

Most of the cell types used in this thesis were cultured on coated Corning (USA) tissue culture plastic (TCP) or cell culture grade coverslips when being used for immunocytochemistry assays (ICC). Glass coverslips (13 mm thickness, VWR) were sterilised in 70% ethanol and allowed to dry overnight in the laminar flow hood to allow for complete evaporation before use. The aim of cell culture coatings was to enhance long term adherence of cells. The specific coatings and their preparation are described in each of the subsections below.

3.1.3. Storage and thawing of cell lines

Cell lines were all stored in their respective culture media+ 10% Dimethyl sulfoxide (DMSO, Sigma-Aldrich, USA) in liquid nitrogen unless stated otherwise. All cells were stored at 1,000,000 cells/vial

All cell lines were thawed in a 37 °C water bath and resuspended in their respective media. Cells were then centrifuged at 200xg, unless otherwise stated, to form a pellet and the supernatant was discarded. Cells were then counted on a haemocytometer and seeded at sufficient densities, specified for each cell type in the sections below. Cells were banked in vapour phase liquid nitrogen storage, with at least 20 vials per cell line and type.

3.1.4. NG108s and OECs

The rat-mouse hybridoma cell line NG108-15 (obtained from collaborators in the Department of Biochemical Engineering at UCL) was initially used to model motor neurons of the SC (Chapter 5). Cells were maintained in T-75 culture flasks and passaged approximately every 5 days when at around 80% confluency. They were maintained in DMEM/F12 (1:1) + GlutaMAX™ medium (Gibco™ 2156450) with 10% foetal bovine serum (FBS) (Sigma-Aldrich F2442) in a humidified incubator at 37 ºC and 5% CO_2.

Olfactory ensheathing cells (OECs, obtained from collaborators in the Department of Biochemical Engineering at UCL) were used in co-culture experiments for cell alignment (Chapter 5), maintained in T-75 culture flasks, seeded at 5,000/cm^2 and passaged approximately every 7 days when at around 80% confluency. They were maintained in DMEM/F12 (1:1) + GlutaMAX™ medium (Gibco™ 2156450) with 10% foetal bovine serum (Sigma-Aldrich F2442). Tissue culture plates and flasks were freshly coated with Poly-L-lysine (Sigma-Aldrich, 100 µg/mL) incubated for 30 minutes, and then dried for 30 minutes. The OECs used in this work had previously gone through an immortalisation process, using the c-MycER^{TAM} technology (Santiago-

Toledo et al., 2019). To facilitate cell growth of OECs, a 1:10,000 dilution of 4-hydroxy-tamoxifen (4-OHT, Sigma-Aldrich) was added to the media on the day when media change/cell passaging was required, as its unstable above -20 ºC. Cells were cultured in a humidified incubator at 37 ºC and 5% CO_2. Cells were used up to passage 8, beyond this, growth began to slow and cell morphology changed.

3.1.5. SH-SY5Y

SH-SY5Y cell line, a human neuroblastoma which has been cloned three times from the SK-N-SH neuroblastoma line, was used as a human motor neuron model (Chapter 5). Cells had previously been virally transfected with GFP and mCherry fluorescent tags after ebing obtained from European Collection of Cell Cultures (cat. no: 94030304) (George et al., 2018), allowing for live cell imaging on opaque scaffolds. Cells were seeded onto tissue culture plastic at a seeding density of 20,000/cm^2 and maintained in RPMI (Sigma) +10% FBS (Sigma-Aldrich) +1% GlutaMAX™ in a humidified incubator at 37 ºC and 5% CO_2. Cells were fed every 2-3 days and passaged every 5-7 days at around 80% confluency.

3.1.6. SH-SY5Y Differentiation

SH-SY5Y cells were differentiated on tissue culture plastic or coverslips were coated with 200 µL/cm^2 of 20 µg/mL Poly-L-Ornithine (pORN) in dH_2O, incubated for 4 hours, followed by 2 washes with sterile dH_2O. Laminin was dissolved in dH_2O at a concentration of 10 µg/mL, coating at 200 µL/cm^2, and incubated overnight. This was then removed and washed with DPBS without calcium and magnesium prior to cell seeding. Cell seeding density was 20,000/cm^2 in RPMI (Sigma) + 10% FBS (Sigma) +

Glutamax (Gibco). Cells were allowed to attach for 24 hours before media being changed to DMEM/F12 (Gibco) + 10% FBS (Sigma) + Glutamax (Gibco) with 10μM EC-23 Retinoic Acid (HelloBio) to begin differentiation. Cells were fed every other day for 5 days before media was changed to DMEM/F12 (Gibco) + Glutamax (Gibco) + 50ng/mL BDNF (Stem Cell Technologies, Germany). This media was replaced every other day until the end of the experiment.

3.1.7. Induced pluripotent stem cells (iPSCs)

Healthy control iPSCs (referred to as LN5) were obtained from Axol Biosciences (UK) and used between passages 30 to 38. They were derived from CD34+ cord blood from a male new-born, and reprogrammed through a non-integrating episomal vector. These arrived with a normal karyotype and were negative for mycoplasma. TCP was coated with human recombinant vitronectin (VTN) (ThermoFisher, USA) for at least 1 hour, diluted 1:100 (10 μg/mL) in sterile Dulbecco's Phosphate Buffered Saline (dPBS) without Ca^{2+} and Mg^{2+}. iPSCs were defrosted in a 37°C water bath until a small ice crystal was left. 1 mL of DMEM/F12 was added into the 1 mL cell suspension in the cryovial, and then the 2 mL were added to 3 mL of DMEM/F12. This was then centrifuged at 200g for 5 minutes until a cell pellet was formed. The supernatant was removed, and the pellet was resuspended in complete E8 media (ThermoFisher, USA) supplemented with 10 μM Rock-Inhibitor for the first 24 hours, (Y-27632, HelloBio, UK). The cell suspension was triturated only 3-4 times to retain cells in clumps. They were then plated into the VTN coated plates. Cells were fed daily with full media changes of complete E8 media and inspected for random differentiation. This process continued for 4-7 days until the larger colonies began to touch, at which point cells were split, replated and frozen. Cells were washed twice

with sterile dPBS (without Ca^{2+} and Mg^{2+}) before 50 µM EDTA (Gibco) diluted in sterile dPBS (without Ca^{2+} and Mg^{2+}) was added and incubated for 5 minutes at 37°C. When the edges of the colonies were beginning to detach and curl up, the EDTA was removed, complete E8 was added, and the media was rinsed over the surface in order to gently detach the whole colonies. These colonies were then split between 1:6-1:10 either into VTN coated TCP or into Cryovials with 10% DMSO for freezing.

3.1.8. Embryonic Stem cells

The Embryonic stem cell line, LT1e-OLIG2GFP, were purchased from WiCell, via a material transfer agreement (MTA). They were modified from the hESBGN-01 human embryonic stem cell line by Xue et al. (2009). This was carried out using homologous recombination to create this stable line. This line was used between passages 25 and 30, with no mycoplasma and normal karyotype upon arrival. These cells were cultured in the same manner as the iPSCs, with no notable differences.

3.1.9. Neural induction of iPSCs

iPSCs underwent neural induction using a modified method from Shi et al. (2012)iPSCs were seeded at 20% confluency between passages 30 and 40 on 2X VTN concentration, 20 µg/mL, in complete E8 media. After 24 hours, media was changed into E6 (ThermoFisher, USA) + 2µM XAV-939 + 10µM SB431542 + 0.1µM LDN193189, this is the neural induction media (NIM). Cells were fed daily for 12 days. At around day 7-9, neural rosettes began to form, where cells organise themselves.

After 12 days in neural induction media, cells were detached using Accutase (Sigma-Aldrich,USA) to obtain a single cell suspension. Cells were washed twice with sterile dPBS (without Ca^{2+} and Mg^{2+}) and Accutase was added and incubated at 37°C for 5 minutes. This was then inhibited with 3x the amount of DMEM/F12. Cell suspension was then centrifuged at 200g for 5 minutes. The supernatant was removed and the cell pellet was resuspended in N2B27 media, consisting of a 1:1 mix of Advanced DMEM:F12 (ThermoFisher, USA) and Neurobasal Media (ThermoFisher, USA) with 1% Glutamax (ThermoFisher, USA) 0.5X N2 (ThermoFisher, USA), 0.5X B27 (ThermoFisher, USA), known as Neural Maintenance Media (NMM). Cells were seeded on coverslips, for ICC imaging, coated with 200 µL/cm^2 of 20 µg/mL Poly-L-Ornithine (pORN) in dH_2O, incubated for 4 hours, followed by 2 washes with sterile dH_2O. Laminin was dissolved in dH_2O at a concentration of 10 µg/mL, coating at 200 µL/cm^2, and incubated overnight. This was then removed and washed with DPBS without calcium and magnesium prior to cell seeding. For cell seeding media was supplemented with 10 µM Rock-Inhibitor, and after 24 hours, this was removed. NPCs were then fed every 2-3 days and passaged at around 90% confluence.

3.1.10. Neural Precursor Cells (NPCs)

Tissue culture plastic or coverslips were coated with 200 µL/cm^2 of 20 µg/mL Poly-L-Ornithine (pORN) in dH_2O, incubated for 4 hours, followed by 2 washes with sterile dH_2O. Laminin was dissolved in dH_2O at a concentration of 10 µg/mL, coating at 200 µL/cm^2, and incubated overnight. This was then removed and washed with DPBS without calcium and magnesium prior to cell seeding. Cells were seeded in 6 well plates for expansion at around 100,000/cm^2, changing the media every 2-3 days. They were passaged at around 90% confluency, removing media and washing with dPBS without magnesium and calcium. Cells were detached using Accutase (ThermoFisher,

USA) to obtain a single cell suspension, covering the whole cell surface and incubated for 5 minutes. DMEM/F12 was added equal to three times the volume of Accutase used to neutralise the dissociation reaction. Cells were then centrifuged for 5 minutes at 200 x g, to form a pellet. This was then resuspended in NMM and seeded where required. At passage 3 or 4 cells were transferred to their final format, either onto coverslips or onto micro-hollow fibres for experimentation.

3.1.11. Freezing NPCs

Cells were split as described in Section 3.1.7 with Accutase and counted using a 1:1 dilution of trypan blue (ThermoFisher, USA) on a haemocytometer. The cells in the 4 corners of the grid were counted and the averages were obtained, although this counting method comes with its problems, and is not the most accurate way of counting cells, this was the only method which we could utilise (Piccinini et al., 2017). Cryovials were labelled and filled with 100 µL of DMSO. Cells were diluted to 2-4x10^6 cells/900 µL inNMM. then 900µL of cell suspension was added and cells were transferred to a CoolCell (Corning, USA) and placed at -80°C for at least 24 hours, before being moved to vapour phase liquid nitrogen for long term storage.

3.1.12. Motor Neuron Differentiation from NPCs

Day 0 of this differentiation starts when cells had reached the NPC stage in NIM at around 80% confluency. They then were transferred to E6 media + 200ng/mL Sonic Hedgehog (SHH) (Stem Cell Technologies) + 50µM RA + 8ng/mL bFGF (Peprotech) + 10ng/mL Activin A (Stem Cell Technologies). When they reached 100% confluency after around 2 days, cells were passaged onto pORN/Laminin coated plates using

Accutse in the same manner as described for NPCs, at a seeding density of 100,000/cm^2. These were then fed daily for 10 days, until day 14. After this point media was changed every other day, By this point some of the cells should have started expressing Olig2. At this point some wells were dissociated for cryopreservation. By day 30, most cells should be expressing Olig2.Beyond day 30, cells were fed every other day, with E6 + 10ng/mL BDNF (Stem Cell Technologies) + 10ng/mL GDNF (Stem Cell Technologies). This maturation took up to 4 weeks, by which point they should have started expressing the mature marker HB9. The differentiation of motor neurons was unsuccessful, as discussed in section 5.3.4.

3.1.13. Neuronal Differentiation

At passage 3 or 4, NPCs were transferred to final plating format. NPCs were seeded at 100,000/cm^2, which is slightly lower than usual so as to be able to see individual neurites. Plates were coated with pORN/Laminin, into NMM with 10μM Rock inhibitor. Media was changed on day 1 to remove death and Rock inhibitor. After 48 hours, media is changed into BrainPhys + SM1 (Stem Cell Technologies, Germany) + 20ng/mL BDNF (Stem Cell Technologies, Germany) + 20ng/mL GDNF (Stem Cell Technologies, Germany) + 2μM Compound E (HelloBio). This media was changed every 3 days with half media changes. After 6 days of treatment with Compound E, this was removed and cells were fed every 3 days with BrainPhys + SM1 + 20ng/mL BDNF + 20ng/mL GDNF.

3.1.14. Seeding Cells on Micro-Hollow Fibres

NG108-15s, OECs, undifferentiated SH-SY5Ys and NPCs were split as usual (explained in the corresponding previous sections), counted and 1 mL of cell suspension in the appropriate media was placed in an Eppendorf tube at the given, density: 500,000/mL, 1,000,000/mL or 2,000,000/mL. up to 10 fibres were then placed in the tube and this was transferred to an incubator overnight. The following day, fibres were removed and placed in 5 x 5 well square, non-tissue culture treated petri dishes (Sterilin) for culture, with each well being $4cm^2$. Media was changed as in 2D controls. With 1 – 2mL per well.

3.1.15. Immunofluorescent Staining (ICC)

Immunofluorescent staining incubation times were all performed at room temperature unless specified otherwise.

Cells were cultured for immunocytochemistry (ICC) on 13 mm cell culture grade coverslips. Cover slips were separated from each other and sterilised using 100% ethanol under constant agitation for at least 1 hour, before being placed in wells and allowed to dry in cell culture laminar flow hood to ensure total evaporation. Cells were then fixed using an equal volume of cell culture medium and 4% (v/v) paraformaldehyde (PFA) for 5 minutes. This was then removed and replaced with 4% PFA alone for a further 5 minutes, then washed twice with PBS. Permeabilization buffer, PBS with 0.2% (v/v) Triton-X-100 was added for 5 minutes twice. Cells were then blocked for 1 hour in blocking buffer (BB), PBS with 0.2% (v/v) Triton-X-100 and 2% (w/v) bovine serum albumin (BSA) on a rocker at a low RPM. Cells were then

stained with one or two primary antibodies which were dissolved in BB for 1 hour (see Table 2). Cells were washed 3 times for 5 minutes in BB to remove any excess primary antibody. Secondary antibodies were dissolved in BB at 1:500 (See Table 2) and added for 1 hour, protecting them from light throughout. Coverslips were then washed again in BB 3 times for 5 minutes. They were then rinsed with dH_2O before being placed cell side down on glass microslides in mounting medium containing DAPI (Fluoroshield). Slides were then left to dry overnight and stored at 4°C, whilst being protected from light. Non-specific staining was checked by adding secondary antibodies alone.

Table 2: Primary and secondary antibodies used for immunocytochemistry. Those frequently co-stained together are grouped together with squares.

Antibody	Expression	Dilution	Species	Secondary (all used 1:500)	Cells Lines
Oct4 (Abcam, Ab181557)	Marker of Self-renewal	1:300	Rabbit	Goat Anti-Rabbit FITC (green) (Jackson ImmunoResearch, 127016)	iPSC, ESC
Sox2 (R&D systems, MAB2018)	Pluripotency and Self Renewal Marker	1:100	Mouse	Donkey Anti-Mouse Rhodamine (red) (Jackson ImmunoResearch, 112581)	iPSC, ESC, NPC
Pax6 (Biolegend, 901301)	Neural Precursor Cells Transcription Factor	1:300	Rabbit	Goat Anti-Rabbit FITC (green) (Jackson ImmunoResearch, 127016)	NPC

MAP2 (Abcam, Ab5392	Mature Neurons Cytoskeleton	1:1,000	Chicken	Goat Anti-Chicken	NPC, iPSC derived Neuron, Motor Neuron
βIII tubulin (Invitrogen)	Neuron-Specific Tubulin	1:500	Mouse	Donkey Anti-Mouse Rhodamine (red) (Jackson ImmunoResearch, 112581)	NPC, iPSC derived Neuron, SH-SY5Y
OLIG2 (Invitrogen)	Motor Neuron Precursor Transcription Factor	1:200	Rabbit	Goat Anti-Rabbit FITC (green) (Jackson ImmunoResearch, 127016)	Motor neurons
HB9 (DSHB)	Mature Motor Neuron Transcription Factor	1:200	Mouse	Donkey Anti-Mouse Rhodamine (red) (Jackson ImmunoResearch, 112581)	Motor neurons
Ki67 (Abcam, ab15580)	Cell proliferation	1:500	Rabbit	Goat Anti-Rabbit FITC (green) (Jackson ImmunoResearch, 127016)	NPC
Nestin (Merck MAB5326)	Neural Precurson Cytoskeletal Protein	1:300	Mouse	Donkey Anti-Mouse Rhodamine (red) (Jackson ImmunoResearch, 112581)	NPC

3.1.16. AlamarBlue® as a surrogate measure of cell proliferation

Culture media was supplemented with 10% (v/v) AlamarBlue® (ThermoFisher, USA) and incubated at 37˚C and 5% CO_2 for 4 hours. After this point, AlamarBlue® media was removed stored in Eppendorf tubes. Cells were washed with PBS and were fed with standard culture media. Spent AlamarBlue® media was then transferred to black 96 well plates and 100 µL per well was added. The plate was read on a BMG Labtech FLUOstar Omega microplate reader at an excitation wavelength of 560nm and absorbance wavelength of 590nm.

$$\%\ Reduction\ AlamarBlue = \frac{S^{x} - S^{control}}{S^{100\%\ reduced} - S^{control}} \qquad (1)$$

This equation was used to estimate cell viability where:

- S^{x} is the sample fluorescence
- $S^{100\%\ reduced}$ is the fluorescence from 100% reduced, autoclaved, media + 10% AlamarBlue
- $S^{control}$ is the fluorescence of the fluorescence from the control, culture media + 10% AlamarBlue

AlamarBlue® was chosen as it is not an end point assay, which, due to cost constraints, was more effective to be able to do repeated measurements on the same sample without further setups required. The resazurin in the solution is reduced my cellular metabolites, converting it to the fluorescent resorufin, which is then read on the plate reader (ThermoFisherScientific, 2023).

3.1.17. Cell Tracker Green

Before cells were seeded in their final format, they were loaded with CellTracker™ Green (Invitrogen). The dye was dissolved in DMSO to a stock concentration of 5 mM, and filtered through a 0.2 µm, regenerated cellulose, sterile filter (Sartorius). This was then added to NMM at a final concentration of 5 µM on the NPCs for 30 minutes. This was then removed, and the cells were washed once with PBS and fresh NMM was added. Cells were then imaged at specific time points.

3.2. Biomaterials fabrication and characterisation

3.2.1. Micro-hollow fibre (Micro-HF) fabrication

A phase inversion, single orifice spinneret method was followed to fabricate the micro-HFs, adapted, and optimised from the protocol described by Yao et al. (2012). The casting solution was prepared in a sealable flask; 0.75 g of polycaprolactone (average M_n 80,000, Sigma-Aldrich, Dorset, UK), 0.75 g of polystyrene (average M_n 280,000, Sigma-Aldrich, Dorset, UK), followed by 8.5 g of 1-Methyl-2-pyrollidone (NMP, Acros Organics, Fisher Scientific, Loughborough, UK) was added and the flask sealed to avoid solvent evaporation. The solution was stirred continuously under gentle heat until the polymers were fully dissolved. Once dissolved, 1 mL of paraffin oil (Sigma-Aldrich, Dorset, UK) was added and mixed on a magnetic stirrer overnight. A syringe pump (Cole-Parmer) was set up vertically over a 2-litre beaker of deionized water. The

casting solution was spun through a syringe blunt needle (ADHERE, 27G, 1” long) of internal diameter 0.203 mm attached to a syringe. It was ensured that the needle was fully immersed in the water during the whole fabrication process. A flow rate of 0.01 mL min^{-1} was used for the polymer mixture. A schematic representation of the fabrication process can be seen in Figure 2. After spinning, the micro-HF was transferred into a beaker of fresh deionised water to soak for 24 hours in order to fully extract the solvent (NMP). The ratio water:NMP was sufficiently large to remove all the solvent. This was confirmed by the lack of cytotoxicity of the micro-HFs as scaffolds as shown later in this work. Following this, the micro-HFs were soaked in ethanol at 50 °C for four hours to extract the paraffin oil, forming the lumen and pores of the micro-HFs.

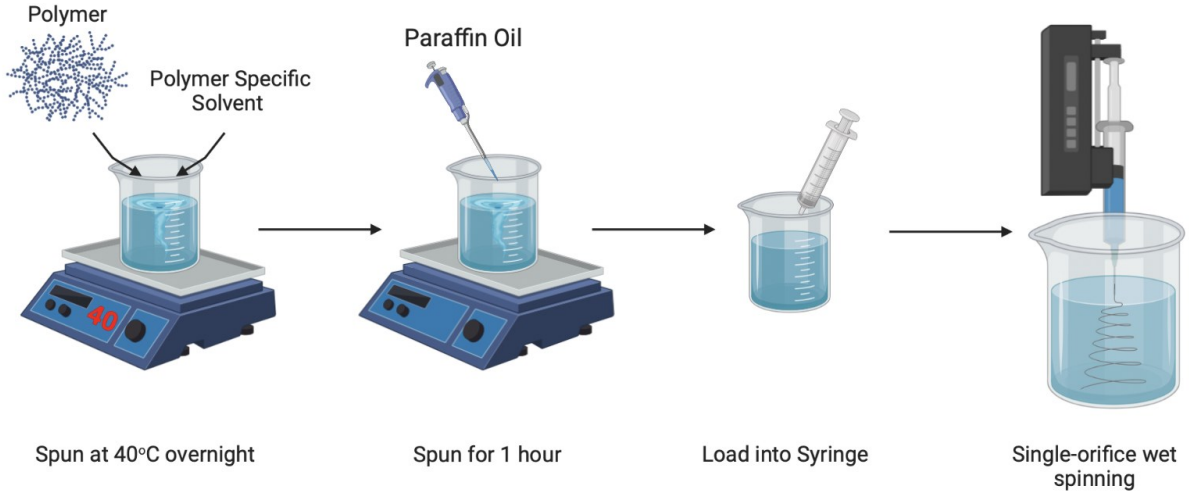

Figure 2: Experimental set-up for the fabrication of micro-hollow fibres via wet spinning using a single-orifice spinneret. Diagram created using BioRender (www.biorender.com).

3.2.2. Morphological characterisation of micro-hollow fibres

Morphological characterisation and quantitative analysis of the porosity of the novel micro-HFs were performed using scanning electron microscopy (SEM) performed at the University of Bath. The micro-HFs were immersed in liquid nitrogen and cut into

pieces of approximately 5 mm in length with a scalpel and were sputter-coated with gold (Edwards Sputter Coater 5150B) and analysed by SEM (JEOL JSM-6480LV) with an acceleration voltage of 10 kV. SEM micrographs of the outer surfaces and the cross-sections of the micro-HFs were obtained. The internal and external diameters, as well as the porosity were estimated using the free software *ImageJ* via image analysis. Ten measurements of both the internal and external diameters were taken manually and averaged. In the case of porosity, three representative sections of the SEM micrographs were considered, the threshold was adjusted to differentiate between clear and dark (pores) areas, and the percentage of the area covered by the pores was calculated and averaged.

3.2.3. Nuclear Magnetic Resonance (NMR) of micro-hollow fibres

NMR spectra of the whole micro-HFs, and their inner and outer parts individually, were recorded using a Bruker Avance III NMR spectrometer operating at 500.13 MHz for ^{1}H. Unless otherwise specified samples were analysed using $CDCl_3$ at 25 °C with standard Bruker pulse sequences (Topspin 2.1). ^{1}H spectra were acquired with a SW of 20 ppm, and 16 transients. Spectra were referenced using the residual solvent signal, at 7.26 ppm for ^{1}H. NMR analysis was provided by the Chemical Characterisation and Analysis Facility (CCAF) at the University of Bath.

3.2.4. Liquid permeation studies in micro-hollow fibres

To determine the permeation of water from the lumen of the micro-HFs through their pores, a custom-made glass bioreactor was used. It contained three micro-HFs of 6 cm in length, and a side port at approximately 2 cm from the inlet that allowed collection

of the permeate. Both the inlet and outlet of the glass module were sealed with silicon glue to ensure that the water flowed exclusively through the lumen of the micro-HFs, and not around them. A constant flow of deionized water was circulated through the lumen of the micro-HFs at a flow rate of 0.1 mL min^{-1} using a syringe pump (Cole-Parmer). This flow rate was sufficient to allow permeation to occur, giving the possibility to collect quantifiable volumes of permeate, but avoiding damage of the micro-HFs due to excessive pressure at the module inlet. Samples from the permeate port were taken every ten minutes for two hours, weighed, and the cumulative mass of permeate calculated. A schematic representation of the experimental set-up can be seen in Figure 3.

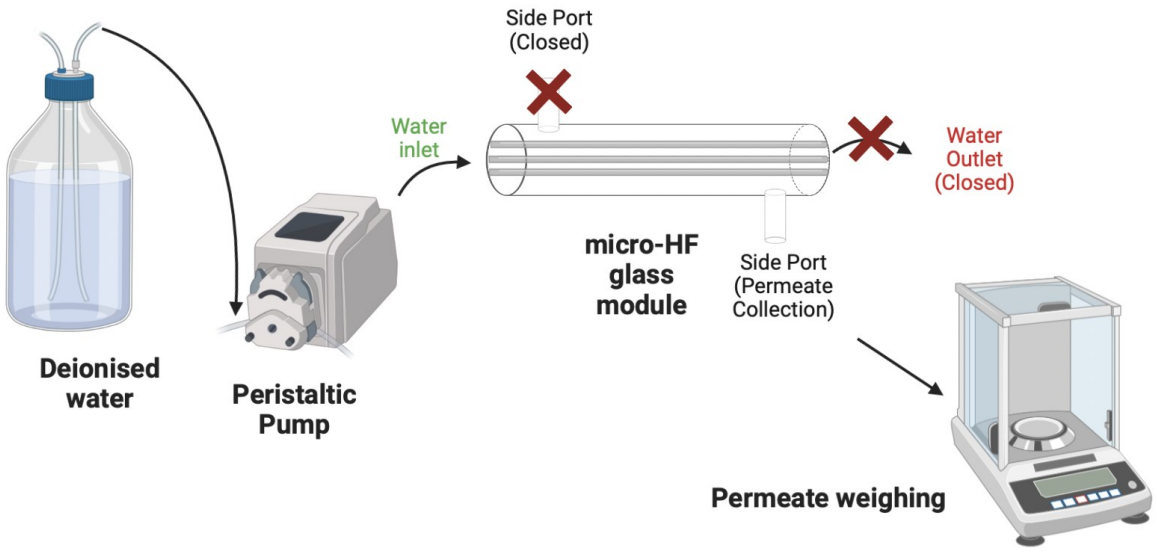

Figure 3: Experimental set-up for liquid permeation of deionised water through the lumen of micro-hollow fibres and out of their pores. Diagram created using BioRender (www.biorender.com).

3.2.5. Coating of micro-HFs for cell culture

Micro-hollow fibres were coated using the same methods as those for tissue culture plates and flasks, as described in Sections 3.1.1 and 3.1.5, with micro-hollow fibres

completely submerged in 1 mL of the coating solutions for full coverage of their outer surface in 1.5 mL Eppendorf tubes.

3.2.6. Mounting of micro-HFs on 3D printed mounts for cell culture

Square mounts were 3D printed in polylactic acid to fit in 5x5 square bacteriological Petri dishes (Sterilin, UK) with a diameter of 19 mm, using a 3D printer with the help of Divya Dhangar (Aston University). The printed ring mounts were then coated with Poly-HEMA (Sigma-Aldrich, UK) to inhibit cell attachment. Poly-HEMA was prepared by dissolving the commercial powder in 95% ethanol (Sigma-Aldrich, UK) at 37 ºC under agitation at 30RPM overnight. Rings were then submerged in the Poly-HEMA solution overnight on a roller. Finally, rings were laid out in a well plate lid and left in a laminar flow hood overnight to allow for complete evaporation with the UV on for sterilisation. Micro-hollow fibres were glued to the ring mounts using Super Glue (Loctite) to maintain alignment and allow for accurate imaging.

3.2.7. Fabrication of fluid gels

Gellan gum fluid gels were fabricated with the commercially available powder Gelzan® (Sigma-Aldrich, USA) used because of cost limitations and existing expertise. The preparation of the gellan gum fluid gels was conducted in a jacketed 250 mL beaker (Duran) for temperature control. Briefly, 99 mL of the desired gel suspension (see Chapter 4 for specific concentrations in each experiment) was weighed into the beaker, and 1 mL of penicillin/streptomycin (Fisher, USA) was added before being microwaved for 90 s, at which point the suspension would reproducibly reach 95°C. The beaker was then placed on a heated stirrer set to 95°C, with a magnetic flea, set to 500 RPM.

After 10 minutes, the heat was switched off and the gel was left until the flea began to bounce. This is around the temperature at which the gel sets, allowing for a semi-consistent stopping point. At this point, the gel was transferred to a falcon tube for storage and rheology. Gels were stored in 50 mL falcon tubes at 4°C

3.2.8. Fabrication of fluid gels for cell culture

Prior to fabrication, the jacketed beaker, with a tin foil lid and the magnetic flea, was autoclaved. 99mL of the desired sterile liquid was then added to the beaker with 1mL penicillin/streptomycin. This was then microwaved as above, leaving the lid open for as little time as possible, alongside using a Bunsen burner to reduce contamination. This was then transferred to the magnetic stirrer and the same process was followed. When complete, the beaker was sprayed into a laminar flow and stored sterile in falcon tubes or used directly in culture.

3.2.9. Morphological characterisation of fluid gels

Fluid gels were freeze-dried immediately after fabrication. 100mL of gel was placed in a round bottom flask and placed on a Edwards Freeze Drier Modulyo for 7 days until the gel mass remained constant. Scanning electron microscopy (SEM) was used to observe gel morphology.

3.2.10. Rheological characterisation of fluid gels

The viscoelastic properties of the fluid gels were measured using a rotational rheometer via small amplitude oscillatory shear testing, where the sample is oscillated

around its resting state, in a continuous cycle. A Malvern Kinexus Pro, stress-controlled rheometer (Malvern Instruments Ltd, UK) at the University of Birmingham (HTI) was used. The samples were loaded between the plates of the rheometer with a standard 1 mm gap and frequency sweeps were conducted with a serrated 25 mm parallel plate and serrated bottom plate. All frequency sweeps were obtained in controlled strain mode between 0.1 and 10 Hz. The ratio of the applied strain in the rheometer provides the complex modulus (G*), which is a quantitative measure of material stiffness or resistance to deformation. G* comprises the elastic (or storage) modulus, also known as Young's Modulus (G') and the loss modulus (G'') (viscous component). In this thesis, the value of interest was mainly G', and a frequency of 1 Hz was selected for comparison between the different fluid gels as seen in Chapter 4.

3.3. Cell Imaging

3.3.1. Live cell imaging

Live cell imaging was performed on an Invitrogen EVOS M5000 fluorescent microscope. This was used for day-to-day phase and live fluorescence imaging.

3.3.2. Fixed fluorescent imaging

Fixed samples were imaged on Zeiss Axiovert 200M epifluorescent microscope using Leica Application Suite Advanced Fluorescence (LASAF) microscopy software (Leica Microsystems, Milton Keynes, UK)

3.4. Data visualisation and statistical analysis

The data shown in this work has been plotted and analysed using Prism 9, Data are presented as mean ± standard error of the mean (SEM) unless stated otherwise in the figure legends.

For N=3, experiments were carried outwith three distinct wells (technical repeats), three separate times, with three separate differentiations (biological repeats) N=3. The number of repeats for each particular experiment is specified either in the text, in the figure legends or both.

The quantitative analysis of microscopy images was conducted using FIJI (Walter et al., 2010) (*e.g.*, micro-hollow fibre porosity, directionality, etc.). This varied depending on the experiment and the methodology is outlined in each specific Chapter.

For the majority of the data one way ANOVA with Tukey's multiple comparisons was used to determine statistically significant differences in the means amongst three or more groups. Equal variances and gaussian distribution were assumed throughout. A t-test was used to compare the means of two groups/populations. All statistical tests were carried out with a confidence level of 95% ($\alpha=0.05$). p values that are larger than 0.05 indicate no significant differences in population means. P values that are smaller than 0.05 indicate significant differences amongst the population means that are being compared. In all figures, a single asterisk (*) indicates $p<0.05$, two asterisks (**) indicate $p<0.01$, and three asterisks (***) indicate $p<0.001$. R^2 in linear regressions was calculated for the line of best fit that minimises the sum of squares of the Y-distances between the experimental points and the line of best fit.

Chapter 4

4. Biomaterials optimisation and characterisation

4.1. Introduction

Biomaterials can fill many roles in scientific research and treatments, with their tuneable properties being a key part in their varying applications. In tissue engineering, creating a 3D network which has the desired mechanical properties and also provides the structural support for cells to be suitably organised is the challenge that this Chapter aims to address, particularly oriented towards *in vitro* modelling of the SC and the glial scar that occurs after injury. Firstly, a more in-depth introduction to some of the characterisation techniques used in this Chapter is provided in Sections 4.1.1 to 4.1.4. This leads to the definition of the objectives of this Chapter, followed by a comprehensive description of the experimental results obtained with regards to the physical characterisation of the micro-hollow fibres that will constitute the scaffold for cellular alignment in the model proposed in this work (Sections 4.2.1 to 4.2.3. Finally, the optimisation and characterisation of the fluid gels that were selected as a mimic of the extracellular matrix in the SCI model are explained in Sections 4.2.4 to 4.2.7.

4.1.1. Rheology

The term rheology is literally translated from its Greek origin as “flow science”, but goes beyond this into the study of the mechanical properties of materials, and how the materials deform when specific forces are applied to them (Chen et al., 2010, Rao et

al., 1986). Soft materials, such as those used here, neither act as ideal solids nor ideal liquids. They have both elastic and viscous responses to forces and as such are described as viscoelastic. The goal of rheology on materials with these soft mechanical properties is to quantify the changes in viscoelasticity over a range of time and forces in order to further understand the properties of the material. These responses are complex in hydrogels and fluid gels due to the particulate, filamentous and other molecular organisations (Chen et al., 2010).

4.1.2. Rotational Rheometry

One of the many strategies to apply force onto a gel for rheological testing is through rotation. As seen in Figure 4, the gel is placed on the sensing plate with a specific geometry (bottom left), then the rotator with the matching geometry is lowered to a specific height on top of the sample (top left). In this setup, the mechanical properties are determined by the torque and rotation measurements. These pieces of equipment are capable of complex measurements with outputs of viscosity, elastic modulus, viscous modulus, complex modulus and others (Chen et al., 2010). The main outputs which rotational rheometers provide are stress and strain. Stress is the force per area that is applied to the sample, while strain is, simply, how much the material deforms. The elastic modulus, or Young's Modulus, is calculated from the ratio of the stress to the strain, the viscous modulus is the strain rate. With viscoelastic materials, both must be considered. The relation of stress to strain is measured over a wide range of strains and timeframes.

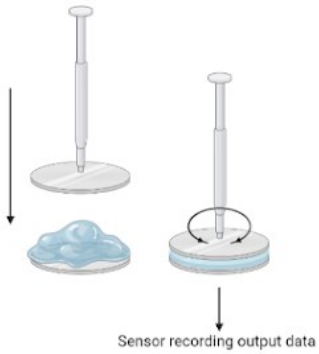

Figure 4: Schematic representation of a rotational rheometer. On the left-hand side, the sample is loaded onto a plate, and the rotator is lowered onto the sample, normally leaving a standard gap. On the right-hand side, the rotator is moving at a specific speed (measured in Hz, or 1/s) to determine the deformation of the sample material. Diagram created using BioRender (www.biorender.com).

4.1.3. Gellan Gum

Gellan gum is a sugar-based polymer, consisting of L-rhamnose, D-glucaronic acid and two D-glucose subunits. It is produced by *Sphingomonas* bacteria, being one of their major extracellular polymeric matrix. It is approved for food use almost worldwide, with diverse uses as a thickening agent, gelling agent, low calorie texturiser, amongst others (Morris et al., 2012, Sanderson and Clark, 1984). Furthermore, it has had long standing uses as an agar substitute for both bacteria (Lin and Jr, 1984) and plant culture (Shimomura and Kamada, 1986). Gellan gum can be polymerised and interlock the chains into a single network structure, when the gel cools in the presence of cations, as it goes through the sol-gel transition temperature, the chains go from a random coil state to 3-fold paired helical structures. Many of these helices are then able to aggregate, crosslinking the polymeric structures leading to a fully formed hydrogel; this forms a solid hydrogel structure (Stevens et al., 2016, Morris et al.,

2012). Applying a shear force to this as it cools through the gelation process leads to the formation of fluids gels (Garrec and Norton, 2012).

With this knowledge, and the conclusion shown at the end of Chapter 2, the specific aims for this Chapter are:

1. **Assessment of the structure, mechanical properties, permeability, and surface topography of newly fabricated micro-hollow fibres to determine their suitability for cell culture in *an in vitro* model of the SC/SCI.**

2. **Optimisation of the formulation and fabrication methods of gellan gum fluid gels based on their rheological properties to mimic the mechanical properties of the extracellular matrix in the spinal cord as seen in the literature.**

4.2. Results

4.2.1. Micro-hollow Fibre Morphology

Previously described methods for production of micro-HFs (Yao et al., 2012) were used in combination with different polymers to make micro-HFs with desired surface topography and utility. The polymers tested were PX (polystyrene), PCL (polycaprolactone) and PLGA, alone and in combinations. These polymers were then examined for their ease of use, and their biodegradability, to determine if they would retain their specific surface topography long enough for cells to attach and be able to align. After micro-fibre fabrication, PX alone was discontinued due to how brittle the micro-HFs were; upon removing from the liquid, the surface tension was sufficient to snap fibres. Equally, PCL alone was discontinued as the micro-HF formation was inconsistent. Combination of polymeric materials to fabricate micro-hollow fibres had the same drawbacks as the single polymer solutions. However, the combination of PCL with PX showed the most promise. The addition of the PCL to the solution, added more flexibility to the fibres without hindering the structure. The fibres produced had a stable surface with no change in topography as seen in through SEM in Figure 5. SEM images also showed the microstructure on and in the fibres themselves. The surface topography remained consistent in all batches fabricated. The micro-HFs' cross-section at a magnification of X500 can be seen in Figure 5A, and the micro-HFs' wall at a magnification of X5,000 is shown in Figure 5B. The most remarkable feature of these novel micro-HFs is clearly noticeable in Figure 5A; there is an inner structure present in the center of the micro-HFs that resembles a hollow fiber itself, and that is detachable manually (Figure 6). Figures 5C and 5D show the inherent grooves that

result from the fabrication process of the micro-HFs on their outer surface at a magnification of X600 and X1,500 respectively.

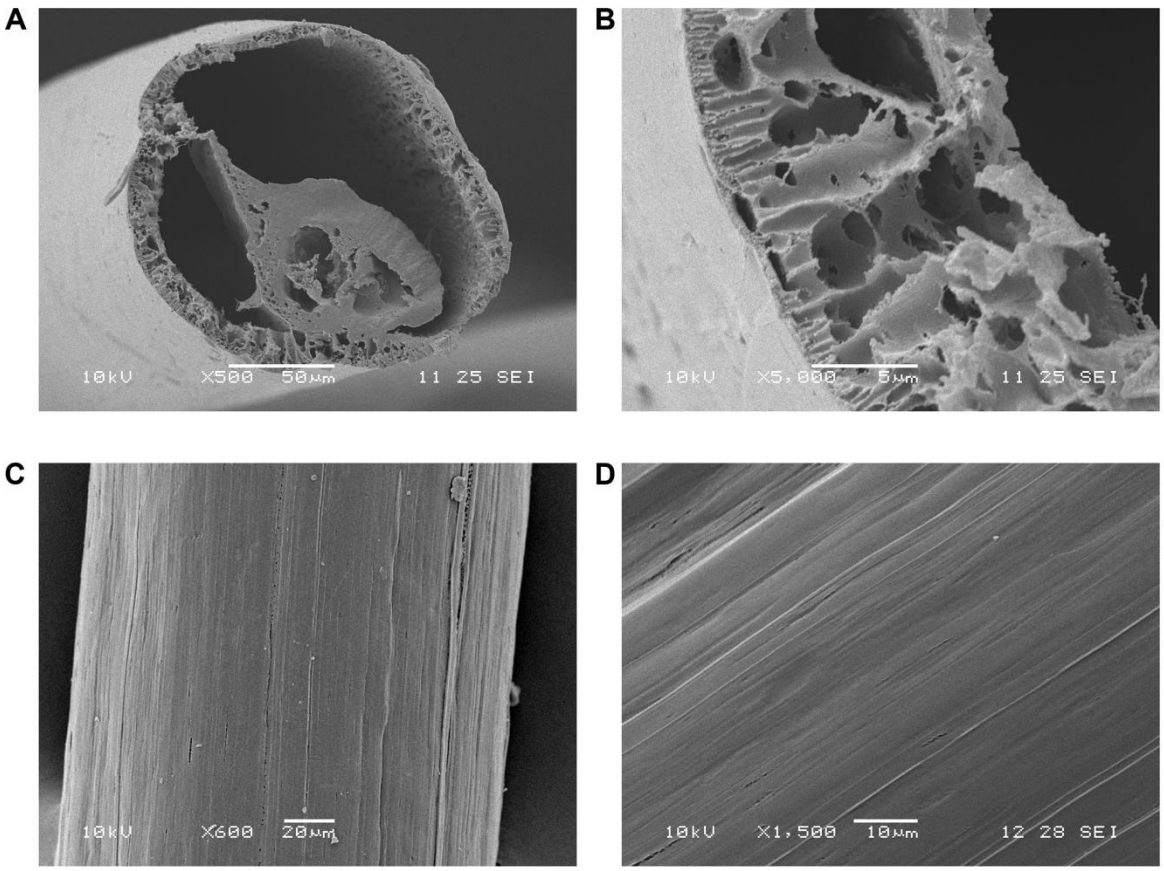

Figure 5: Representative SEM micrographs of PX:PCL micro-HFs. (A) Cross section (X500); (B) Close-up of the cross section to demonstrate the wall's porous structure (X5,000); (C) micro-HF surface, showing the characteristic striations (X600); (D) Close-up of the micro-HF's surface with visible parallel grooves (X1,500). Scale bars: 50 µm (A), 5 µm (B), 20 µm (C) and 10 µm (D). Images were obtained in the imagining facilities at the University of Bath.

Figures 5A and 5B highlight the porous structure of the outer layer of the PX/PCL fibres created, with fully interconnected sponge-like structures throughout the length of the fibre. The porosity was measured using ImageJ analysis (Haeri and Haeri, 2015) and is estimated to be 82 ± 3%. The pores here tend to be focused on the inner portion of the outer fibre, with a narrowing of the pores towards the outer surface. Aside from the

striated topography, the surface appears to be smooth, pores on along the surface as seen in Figure 5B. The inner fibre is shown to be inconsistent in width, with attachment shown on one side of the fibres outer layer shown in Figure 5A.

The addition of PCL to PX caused a formation of two distinct fibres, one within the other. These were detached manually, as seen in Figure 6. The process of separating the inner part from the outer fiber is clearly shown in Figures 6A and 6B.

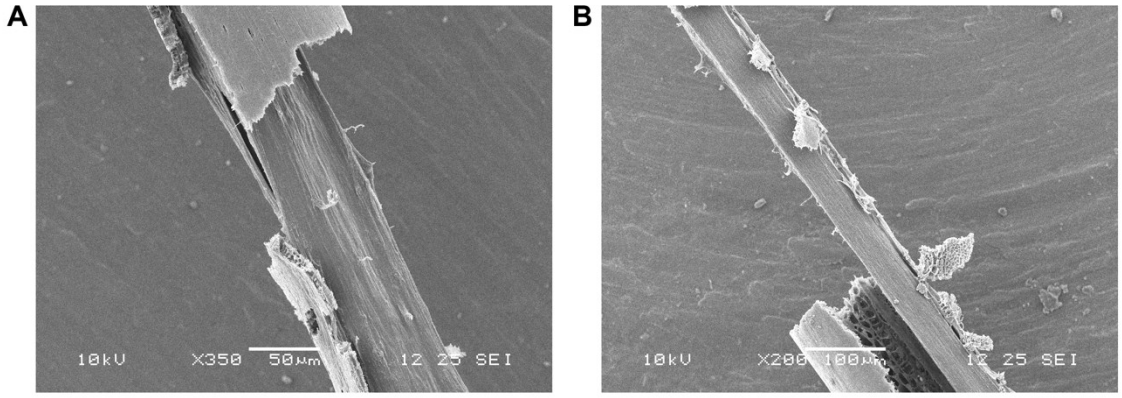

Figure 6: Representative SEM micrographs of PX:PCL micro-HFs. (A) Separation of the inner structure (X350), where the inner fibre peels off from the outer encasing micro-hollow fibre membrane; (B) Inner micro-fibre partially separated from the outer encasing micro-hollow fibre membrane, with a visible porous inner wall of the outer micro-fibre (X200). Scale bars: 50 µm (A) and 100 µm (B). Images were obtained in the imagining facilities at the University of Bath.

The inner diameter of the outer fibre was measured on ImageJ to 144 ± 15 µm (n=10) with an outer diameter of 170 ± 11 µm (n=10), resulting in a wall thickness of 10-13 µm. Fibres were produced using a needle with an internal diameter of 203 µm, showing an 83.7% size reduction once the fibres solidified. The inner fibre diameter was also measured on ImageJ, and the diameter was found to be 81 ± 10 µm (n=10), roughly 56% of the inner diameter of the outer fibre. This leads to around 68% of the inner diameter being empty space which could still be utilised for flow of liquid (*e.g.*, culture media).

4.2.2. Micro-Hollow Fibre Structural analysis via NMR

As seen in Figures 5 and 6, the micro-fibres formed two distinct regions, the outer hollow fibre, surrounding a second solid fibre. Further structural analysis was conducted to determine the molecular make-up of each discrete region of the fibre. Because the outer fibre appeared to have the brittle structure seen in 100% PX fibres it was suspected that the outer layer was largely composed of PX while the inner fibre was PCL. This can be seen in Figure 6, as this breakage was caused by a simple bend in the fibre, cracking the outer layer whilst leaving the inner fibre intact. PX and PCL have different molecular weights, at 280,000 and 80,000 respectively, as well as different viscosities when dissolved in NMP. These were determined experimentally via a high-revolution torque rebalance C-VOR rheometer by collaborators at the University of Bath who found their viscosities were 0.273 ± 0.008 Pa s and 3.543 ± 0.464 Pa s at 25 ˚C respectively. Furthermore, PCL does not fully dissolve at room temperature in NMP, whereas PX is fully dissolved.

The micro-HFs were then sent to the University of Bath for ^{1}H-NMR analysis as seen in Figure 7. Peak i at 7.26 ppm corresponds to the signal of the residual solvent, $CDCL_3$. Figures 7A, B and C show the spectra for the whole fibre, inner fibre and outer fibre respectively. Figure 7C shows a peak at 7 ppm, Peak ii, which is assigned to the aromatic hydrocarbons which are present in the PX structure (Bovey et al., 1965). In contrast, this peak is not present in Figure 7B, which indicates that there is a much smaller proportion of the PX in the inner core. Conversely, the peak at 4 ppm, and 3.3 ppm, Peaks iii and iv respectively, are characteristic of the presence of PCL (Kerman et al., 2005, Ramírez Hernández et al., 2013). Additionally, Peak v, another peak

assigned to PCL, at 2.2 – 2.5 ppm is around 8-fold higher in the inner fibre Figure 7B when compared with Figure 7C.

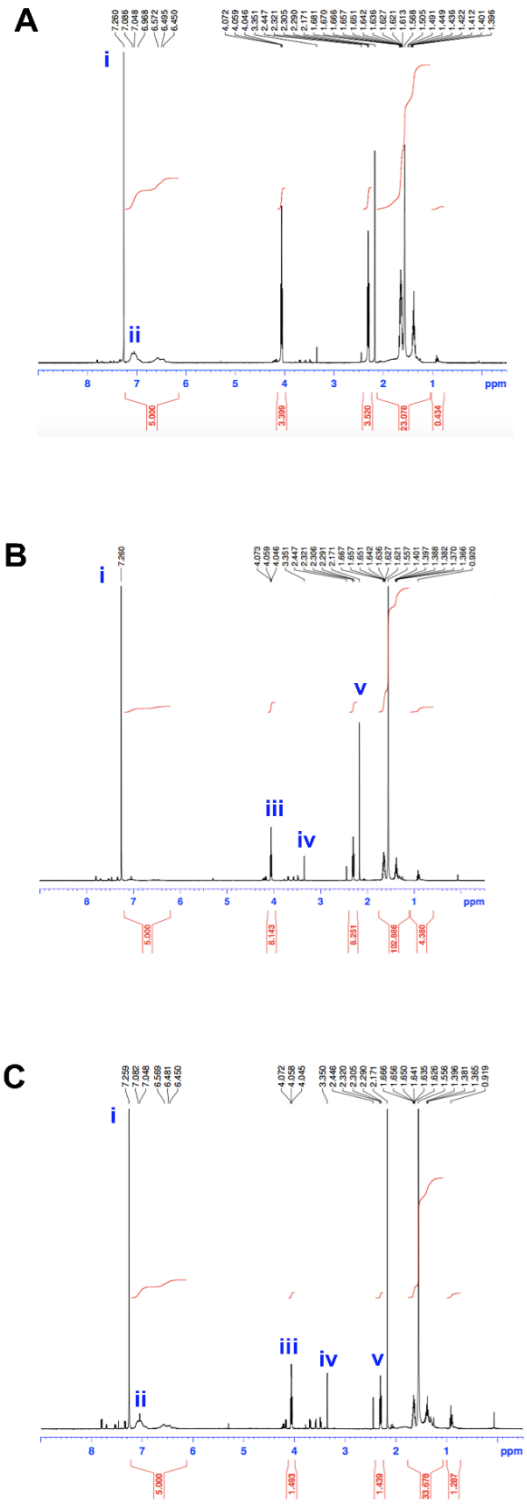

Figure 7: ^{1}H NMR spectrum of micro-HFs. (A) Whole fibre; (B) Inner fibre; (C) Outer fibre. Chemical shift of the peaks in the spectrum (ppm) is indicated at the top of each spectrum. The integration of relevant peaks is shown in red, and the approximate location in the spectrum of relevant peaks is annotated in Roman numerals in blue. i – $CDCL_3$. ii – aromatic hydrocarbons in PX, iii, iv and v – characteristic peaks of PCL.

4.2.3. Liquid Permeation of Micro-Hollow Fibres

Three micro-HFs had ddH_2Opumped through them, as shown in Figure 3 (Chapter 3) at a flow rate of 0.1 mL/min, which was distributed throughout the lumen of the PX/PCL fibres, for 2 hours. The cumulative mass of the permeate is shown in Figure 8, measuring the amount of ddH_2O able to perfuse through the wall of the fibre. At 60 minutes of the 6 g of water that had been pumped through the fibre (black squares), 19.6% of the water had managed to exit through the pores (black dots). Comparatively, at the 120-minute end point, 46.8% of the water had permeated through the pores.

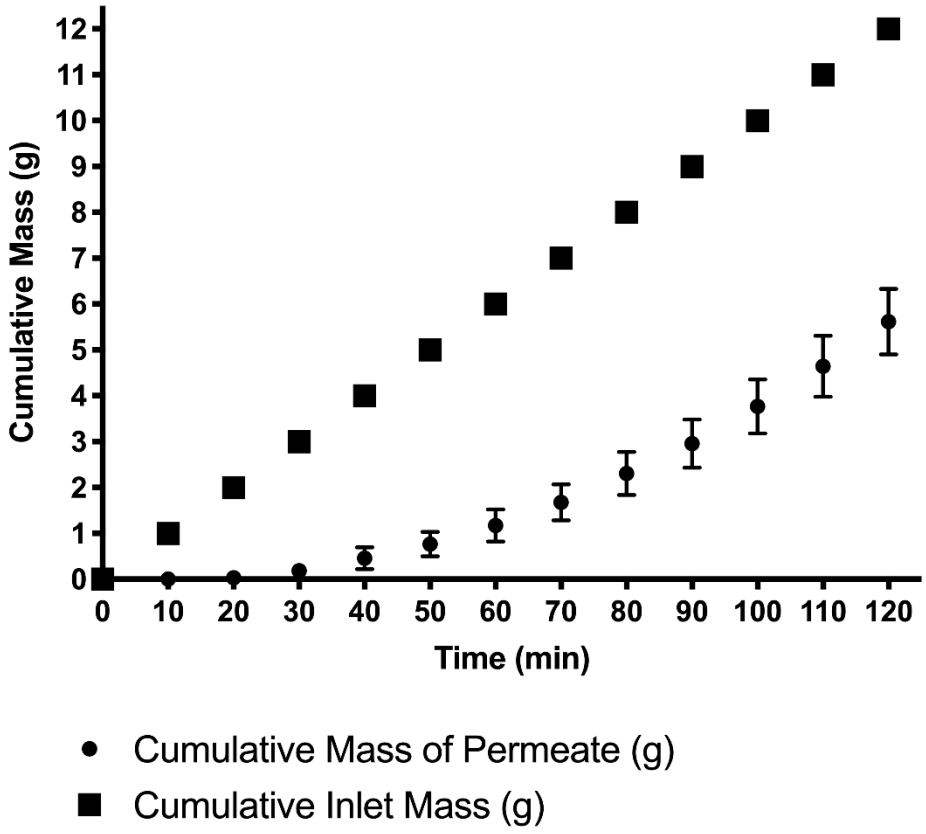

Figure 8 - Liquid permeation through the porous walls of micro-HFS determined as cumulative mass of permeate over time compared to the cumulative inlet mass for a flow rate of 0.1 mL per min pumped through the inner lumen of micro-HFs. (N = 3, Error bars represent the standard deviation of three independent repeats).

4.2.4. Optimisation of the fabrication method of Gellan Gum Fluid Gels

Fluid gels were prepared in a jacketed beaker in order to establish a method to control the rate of cooling. Previous work by colleagues used this method, which constituted a starting point for gellan gum (GG) fluid gel production. A calibration of the peristaltic pump that was used for this particular experiment was necessary in order to determine the flow rates (in mL/min) of cooling water pumped through the jacketed beaker for reproducibility. The use of RPM (settings of the pump) depends on the size and make of the pump and the tubing used, whereas flow rate in mL/min is standard for comparison. The calibration was performed by setting up different values of RPM on the pump (50, 100, 150 and 200 RPM) and weighing the amount of water that was pumped through in one minute. The mass of water (in grams) was then converted to mL by using the water density at the cooling temperature. The results of the calibration can be seen in Figure 9.

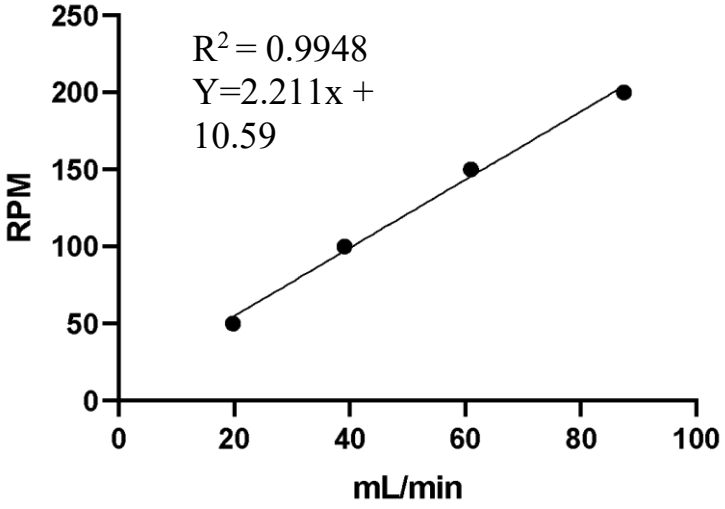

Figure 9: Calibration of the peristaltic pump used to circulate cooling water through the jacket of the beaker used for fluid gel fabrication. A linear regression was performed, and the equation correlates the speed at which the mechanism of the pump moves (RPM) with the flow rate of water pumped (mL/min) – Pump speed (RPM) = 2.211 x (Flow rate) + 10.59.

It was found that 20 mL/min of cooling water was optimal for soft fluid gels in previous work performed in our research group. The speed of the pump to achieve this flow rate was determined using the equation shown in Figure 9, which equates to 54.81 RPM. Iced water was pumped through the jacketed beaker during the cooling process, whilst shearing the fluid gels on a stirring plate at 500 RPM. This cooling method was tested with a GG fluid gel; however, these fluid gels were setting too quickly, leading to solid hydrogels being produced.

The next iteration to optimise the fabrication method of GG fluid gels was testing the cooling process without the water, merely placing the fluid gel for cooling in the insulated beaker, to achieve a slower cooling rate than that reached with flowing iced water. This allows for better temperature control than that provided in a standard single-walled beaker. Fluid gel cooling rates in this set-up were measured for varying concentrations of gellan gum as can be seen in Figure 10.

Figure 10A shows the rate of cooling of fluid gels in this setup compared with gels formed with water cooling at 20 mL/min. Cooling time was terminated when the magnetic flea was no longer able to efficiently spin, shearing the fluid gel evenly, which corresponds to a temperature close to the gelation point of the fluid gel. Fluid gels formed with water cooling reached this point after just 5 minutes (black dots), whereas fluid gels cooled ambiently took between 45 and 75 minutes depending on the concentration of gellan gum (red, green and blue dots). These fluid gels at different concentrations also cooled at similar rates to each other as seen in Figure 10A. The different gelation temperatures are shown in Figure 10B. The cooling water circulated through the jacked in the beaker for a 0.5% gellan gum fluid gel was shown to make a significant difference on the gelling temperature compared to the gelling temperature

of a 0.5% gellan gum fluid gel cooled in the jacketed beaker without cooling water flow ($p = 0.005$).

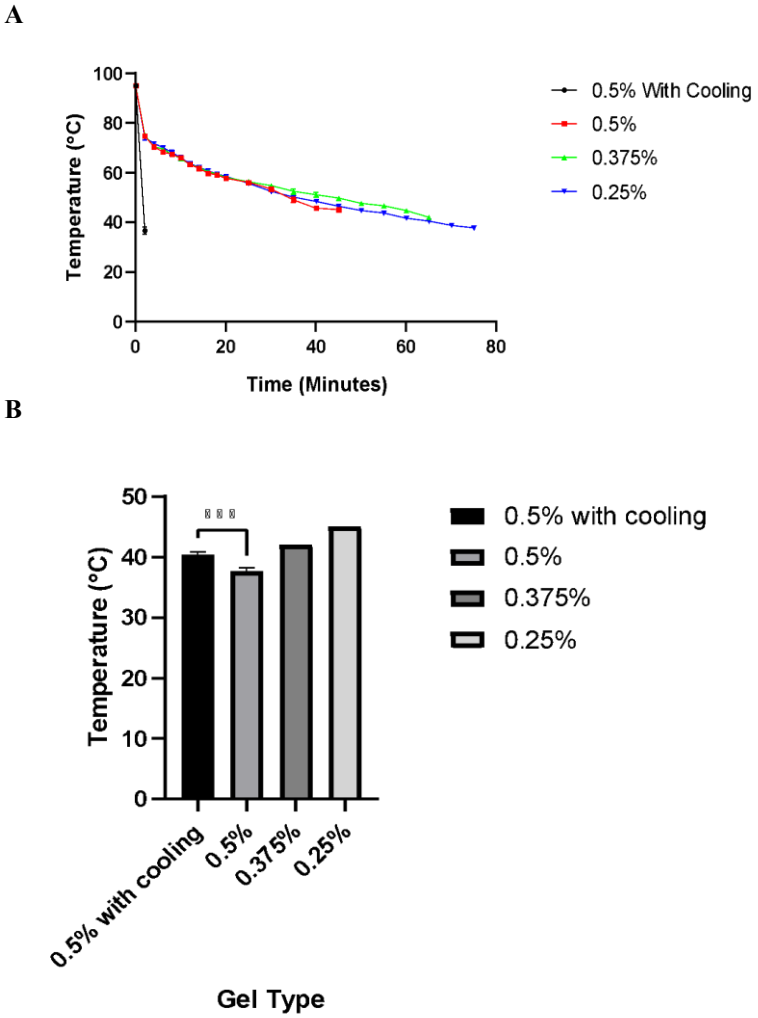

Figure 10: Cooling rates of gellan gum fluid gels in DMEM salt solution (A); Comparison of gelling temperatures of gellan gum fluid gels prepared in DMEM salt solution. (N = 3, Error bars represent the standard deviation of three independent repeats).

4.2.5. Morphological characterisation of gellan gum fluid gels

Fluid gels were freeze dried for SEM imaging, in order to determine their structure. Figure 11 shows ribbon-like structures after the fluid gels were dried, with separations between these ribbons within the fluid gel itself. It would have been beneficial to

perform the imaging without freeze drying, but access to an environmental SEM capable of imaging a substance at 99.4% water was inaccessible.

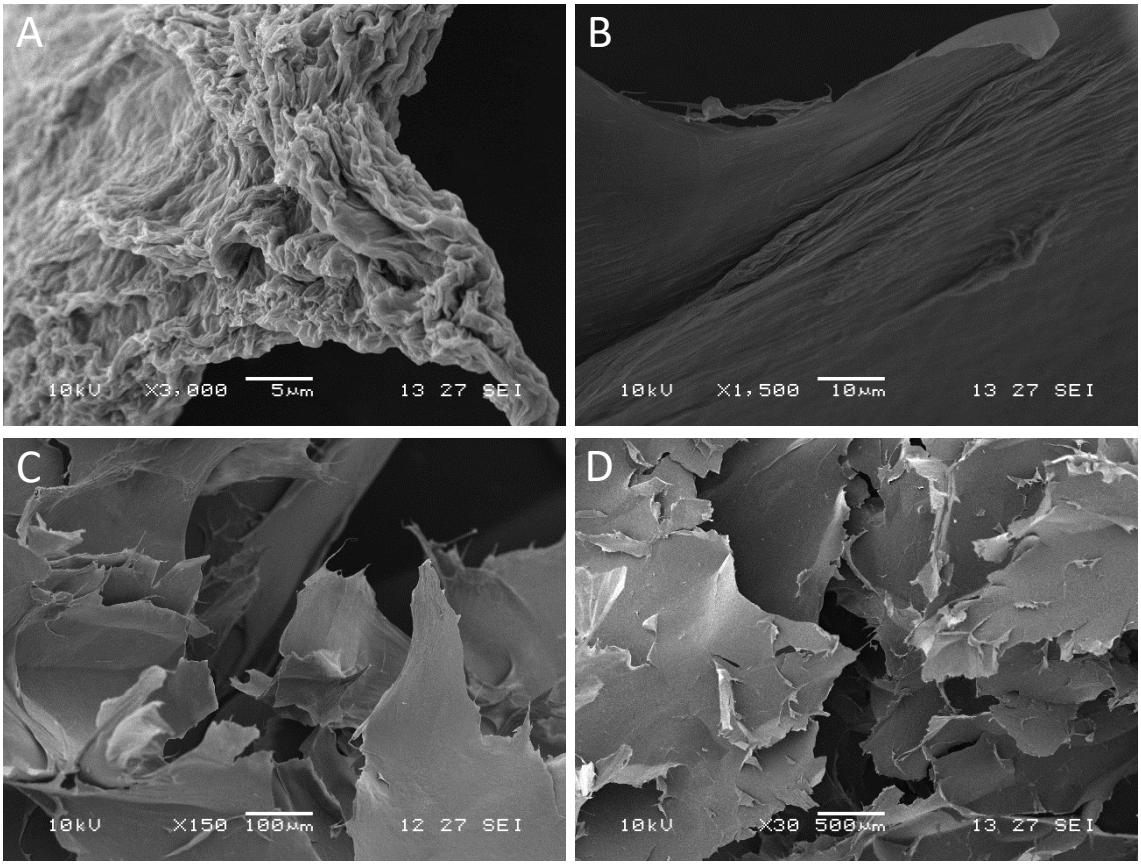

Figure 11: Representative SEM micrographs of 7-day freeze-dried 0.6% (w/w) gellan gum in PBS made in non-cooled jacketed beaker. (A) X3,000; (B) X1,500; (C) X150; (D) X30. Images were obtained in the imagining facilities at the University of Bath

4.2.6. Rheology of gellan gum fluid gels

To prepare fluid gels with a composition that is physiologically relevant, PBS was used, as well as a solution with the salt concentrations of DMEM/F12, using the ions present as crosslinking agents to set the gellan gum. This would also limit the amount of diffusion of salts through the fluid gel as the salt concentrations were similar between

the solutions and the cell culture media used. DMEM/F12 was decided upon as it is the base which is used for the majority of the cell lines used in this work.

Table 3: Salt concentrations used to fabricate fluid gels.

Salt	**Concentration in PBS (mM)**	**Concentration in DMEM/F12 (mg/L)**
NaCl	137	120.61207
KCl	2.7	4.1573334
Na_2HPO_4	8	0.50014085
KH_2PO_4	2	N/A
$CaCl_2$ 2 H_2O	N/A	1.0504504
$CuSO_4$ 5 H_2O	N/A	$5.2x10^{-6}$
$Fe(NO_3)_3$ 9 H_2O	N/A	$1.2376238x10^{-4}$
$FeSO_4$ 7 H_2O	N/A	0.0015
$MgCl_2$ 6 H_2O	N/A	0.30147368
$MgSO_4$	N/A	0.407
$NaHCO_3$	N/A	29.02381
NaH_2PO_4	N/A	0.50014085
$ZnSO_4$ 7 H_2O	N/A	0.0015

The literature was also analysed in order to determine the mechanical properties seen in living tissue, and the variability in data obtained using different mechanical testing techniques. Brain tissue was used as the sample size was larger (many more scientific articles were found), whilst still having similar mechanical properties. The analysis of the data found in the literature can be seen in Figure 12, where no significant differences were found amongst the measuring techniques for elastic moduli (one-way ANOVA).

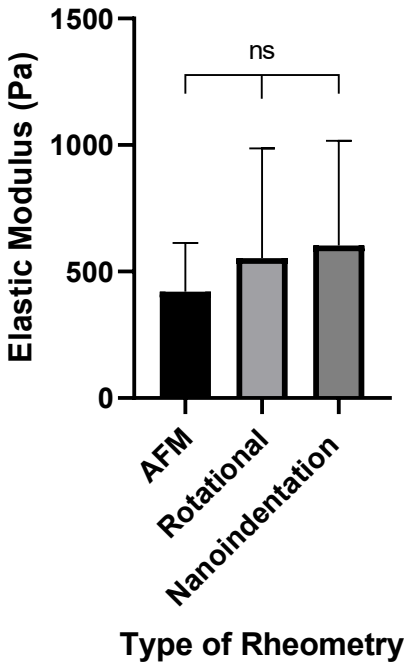

Figure 12: Comparison of mechanical testing of mammalian brain tissue. Numerical rheometry data was extracted from (JORBA et al., 2017, EBERLE, 2020, Ryu et al., 2021, Mijailovic et al., 2021, Budday et al., 2017a, Budday et al., 2017b, Weickenmeier et al., 2018, Parkins et al., 2021, Nicolle et al., 2005, Kruse et al., 2008, Hamhaber et al., 2007, Weickenmeier et al., 2016, Moeendarbary et al., 2017, Millward et al., 2015, Green et al., 2008, Vappou et al., 2007, Wuerfel et al., 2010, Riek et al., 2012). Error bars represent SD.

Additionally, the data shown in (Moxon, 2016) with regards to elastic moduli values of gellan gum fluid gels was analysed to determine the concentrations of gellan gum which should be tested in order to create a fluid gel with the appropriate mechanical properties to mimic the SC tissue (using the AFM data from Moeendarbary *et al*., 2017, as they provided the most detailed rheological data on the SC – 100 – 300 Pa). This was estimated to be within the range of 0.5% - 0.75%, as shown in Figure 13.

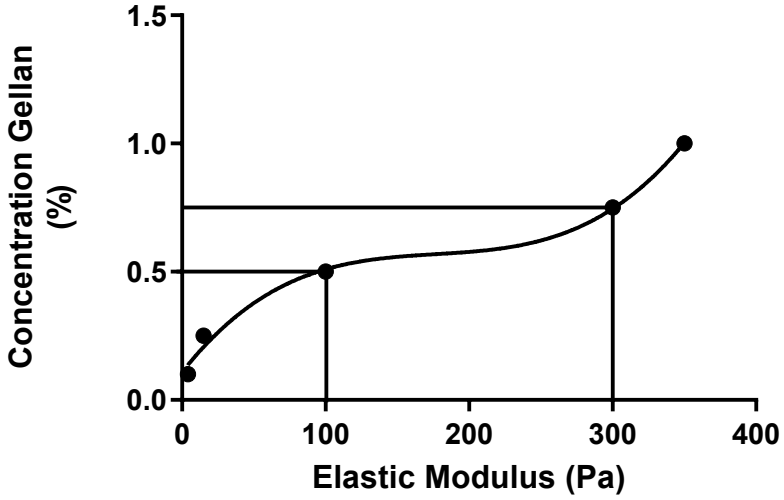

Figure 13: Data analysis from (Moxon, 2016) relating concentration (% w/w) of gellan gum with elastic module measured via rotational rheometry. The dots shown in the figure represent actual published data, joined with a curve of best fit. The vertical and horizontal lines represent the range of concentrations to match stiffness/elastic moduli values in the range of 100 – 300 Pa.

Rotational rheometry was undertaken on all fluid gels on a Kinexus Rotational Rheometer. Two main tests were performed on the fluid gels: frequency sweeps and amplitude sweeps. The frequency sweep was performed first, providing information to take forward for the amplitude sweep. The first gels made were made in PBS aiming to mimic the mechanical properties of the SC. Results of these frequency and amplitude sweeps for 0.6% (w/w) gellan gum fluid gels in PBS are shown in Figure 14.

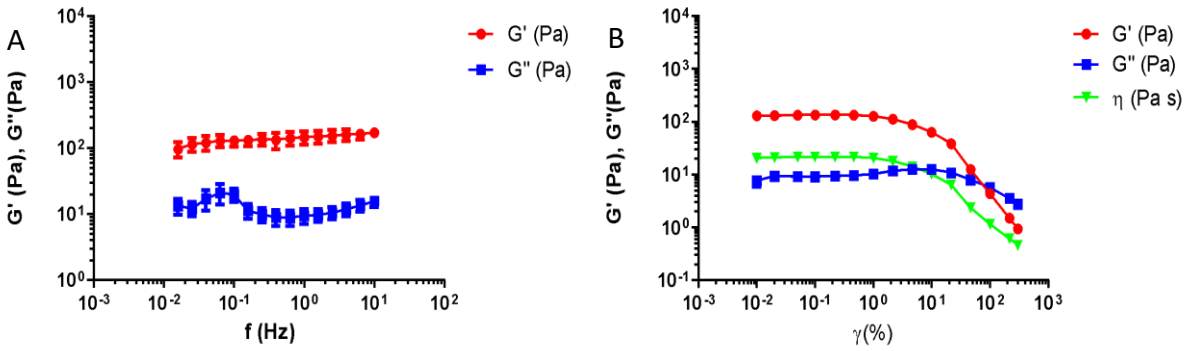

Figure 14: Rheology of 0.6% (w/w) gellan gum fluid gels in PBS. (A) Frequency sweep (0.1% Strain controlled); (B) Amplitude sweep (1Hz). (N = 3, three independently prepared fluid gels tested three times each).

Rheological tests found that 0.6% gellan gum prepared in PBS was within the stiffness range of the SC, and was used as the standard. The frequency sweep shown in Figure 14A showed the value of G' at 1Hz (10^0 Hz) was within the linear region and hence was used in the amplitude sweep (Figure 14B). The G' of the gel was found to be around 145 Pa in the linear region, placing it within the desired stiffness range.

This fluid gel was tested on cells in culture, and findings suggested that the lack of ions involved in cellular attachment caused cells to detach leading to anoikis (Ting-Yu Lai et al., 2022, Paoli et al., 2013). Alongside this, fluid gels were tested using DMEM/F12 as the solvent and the crosslinker. The addition of the extra cations led to stiffer gels, as such lower concentrations of gellan gum were used.

Gels made in DMEM:F12 were a stiffer material than those made in PBS. Figure 15 shows how the gels performed under the same mechanical tests as those shown in Figure 14.

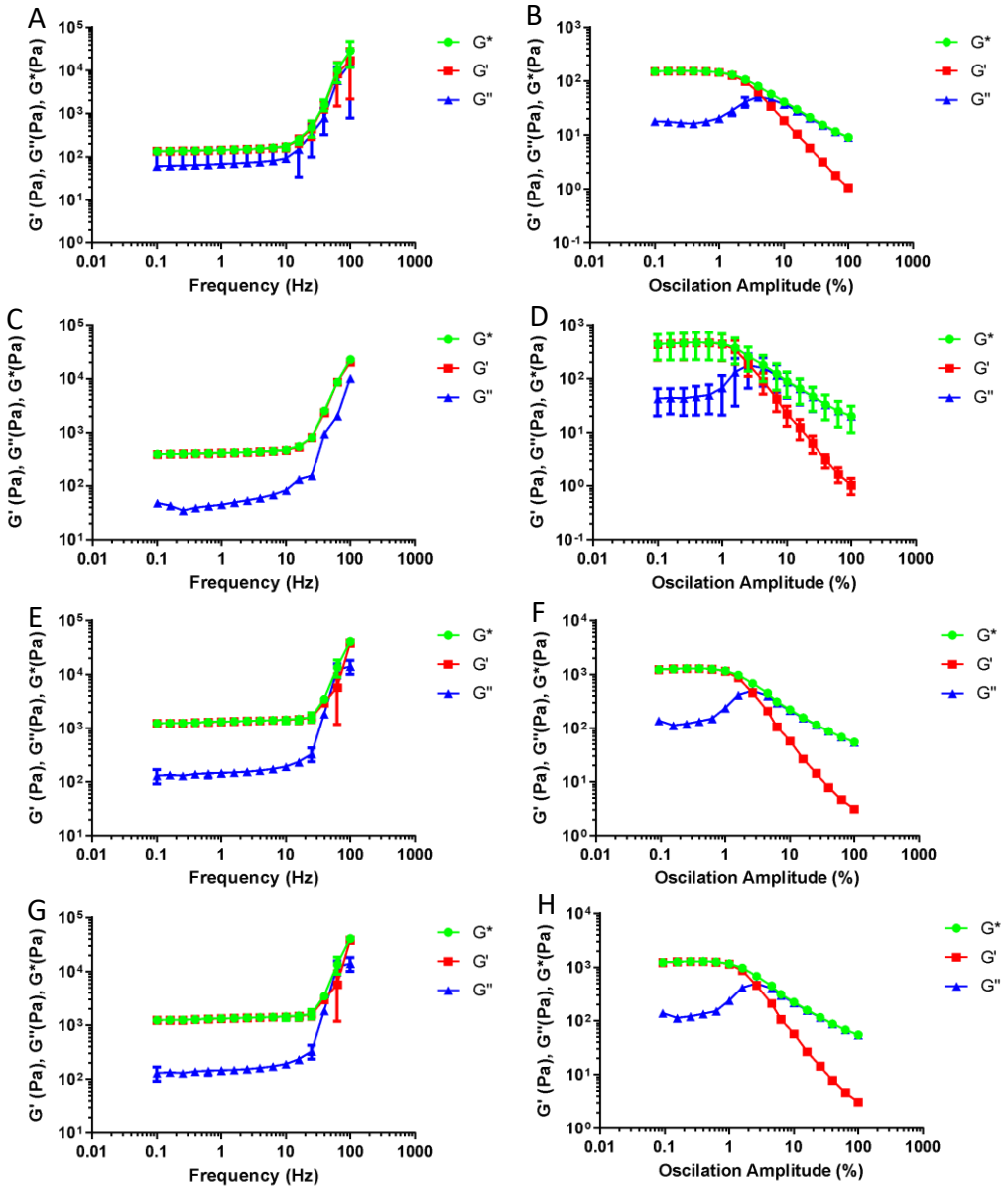

Figure 15: Rheology of gellan gum fluid gels in DMEM/F12. All percentages are (w/w). (A-B) 0.25% gellan gum, (C-D) 0.3175% gellan gum, (E-F), 0.375% gellan gum, (G-H), 0.5% gellan gum. A, C, E, G correspond to frequency sweeps (0.1% strain controlled), and B, D, F, H correspond to amplitude sweeps (1Hz). (N = 3, three independently prepared fluid gels tested three times each).

Figure 15 shows the rheological analysis of the GG fluid gels made in DMEM/F12 salts. The storage modulus G' (G prime, in Pa) (green) represents the elastic portion of the viscoelastic behaviour, which quasi describes the solid-state behaviour of the sample. The loss modulus G" (G double prime, in Pa) (red) characterises the viscous portion

of the viscoelastic behaviour, which can be seen as the liquid-state behaviour of the sample.

All fluid gels are clearly shear thinning, their dynamic viscosity decreases with increased stress. All panels in Figure 15 show a linear viscoelastic regime.

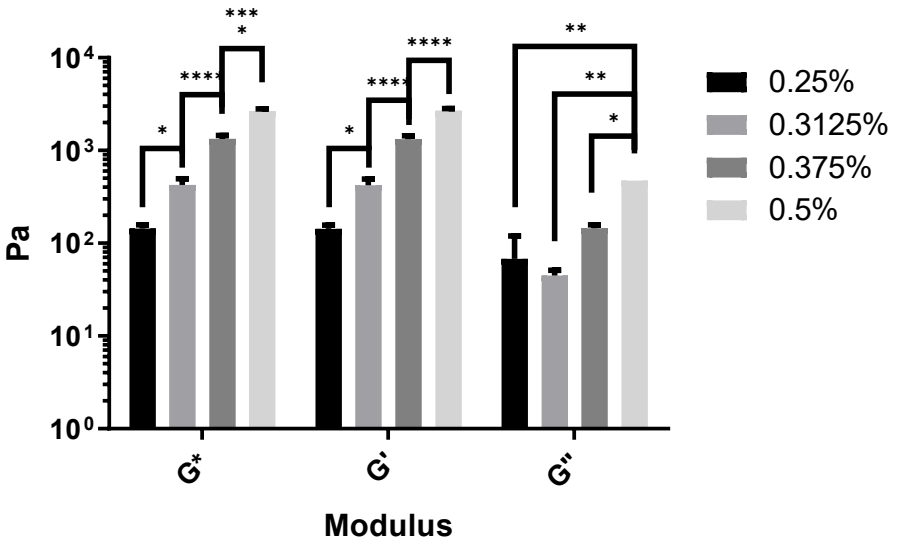

Figure 16: Comparison of elastic moduli values for gellan gum fluid gels prepared in DMEM/F12 salts. N=3 three separate gels measured three times. Data is shown as mean ±.SEM, an ANOVA was performed with Tukey's multiple comparisons.

Figure 16 compares the values of G' (elastic moduli) of the concentrations tested. These were the values seen in Figure 15 at a frequency of 1 Hz. These fluid gels were significantly different from each other, with stiffnesses ranging from 143 Pa to 2,683 Pa. 0.5% gels were made first, as they were a slightly lower concentration when compared to the 0.6% PBS fluid gels. However, it was apparent that the stiffness was vastly different. Lower concentrations of 0.25% at 143 Pa and 0.3125% at 422 Pa were similar to the stiffness values found for SC in an injured and healthy state respectively within the literature (Moeendarbary et al., 2017). These values were then used to mimic the extracellular microenvironment of the healthy spinal cord, 0.3125% (w/w) gellan gum, and the damaged spinal cord, 0.25% (w/w) gellan gum.

4.3. Discussion

Forming biologically relevant *in vitro* models is limited by their 3D nature and mechanical properties of the extracellular environment that can be achieved artificially. Particularly for the central nervous system, cellular alignment similar to what is seen *in vivo* is sought after, and often regenerative outcomes are linked to the cells' ability to align (Nectow et al., 2014).

The results presented in this chapter show that consistent micro-HFs and GG fluid gels can be produced with desirable surface topographies and mechanical properties respectively.

4.3.1. PX:PCL Micro-HFs Fabrication and Characterisation

Production of the micro-HFs was adapted from (Yao et al., 2012), with different polymers being tested for their suitability. Based on the application of micro-HFs for this work as a means of inducing cellular alignment and generating a scaffold for the precise location of cell types present in the spinal cord, it was decided that micro-hollow fibres should have long lasting specific surface topographies to facilitate cell alignment, should be flexible and durable enough to be handled with ease, and should have some level of porosity to aid cell feeding, oxygen and nutrients mass transfer.

Polystyrene has traditionally been used in tissue culture plastic and was therefore tested here as cells are known to be able to adhere and grow on it. Furthermore, the surface coatings used for the iPSC-derived neural cells in this work are known to be able to attach to polystyrene surfaces (Shi et al., 2012). ***The micro-hollow fibres in***

this thesis are not intended as an implant for regenerative medicine purposes, but as a tool for in vitro modelling. Therefore, the biodegradability of polystyrene was not an issue in the decision process for the selection of an appropriate material. This decision around the specific polymers to be used in the micro-hollow fibre formulation was based on their flexibility, handleability, surface topography and ability to promote cellular attachment. Considering all this factors, the 50:50 blend of PX:PCL was used.

With regards to the fabrication method, there are various techniques that can be used to fabricate membranes with dimensions in the micro-scale, such as electrospinning and dry/wet spinning with single or double concentric orifices. Although electrospinning is widely used and has been shown to be an efficient technique for the fabrication of micro- and nanofibers as well as nanotubes, it has some drawbacks in terms of reproducibility and accuracy, mainly due to the complex physical processes that occur within the electrified jet, and also environmental parameters such as temperature and humidity (Luana Persano et al., 2013). Furthermore, the presence of additives in the electrospinning process involves fast solvent evaporation, which makes the porous structure of the hollow fibres difficult to control and leads to the selection of other methods (such as non-solvent induced phase separation) over electrospinning (Chen et al., 2015). These solvents may also be toxic if the constructs are to be used as cell culture platforms (Hong et al., 2019) . Single orifice wet spinning, on the other hand, has the potential to reduce the diameter and thickness of the hollow fibres, and the lack of a bore solution yields a more porous inner wall compared to double orifice spinnerets (Fashandi et al., 2015). Additionally, there are fewer control variables in single orifice wet spinning when compared to coaxial spinning – there is only one dimension to be considered (the diameter of the single orifice), and only one flow rate

to be optimized as opposed to the flow rates of the inner and outer fluids (*i.e.*, the polymer dope and non-solvent) in double concentric orifice spinning***. In this work, the production of micro-hollow fibres was performed using a single orifice spinneret via wet spinning due to its simplicity compared to electrospinning or the conventional concentric orifice spinning process***. Avoiding the inner needle in the fabrication process eliminates the challenge of achieving a uniform central lumen, which is particularly important to attain a robust and reproducible process.

It is known that surface topographies are able to direct protein adsorption. This protein orientation is crucial to the integrin binding, which can in turn direct cellular growth (Lim et al., 2005, Lord et al., 2010). Furthermore, surface topographies have been used to direct cells of multiple lineages include neural (Fan et al., 2002, Rajnicek et al., 1997). Fan et al. found that specific surfaces could positively or negatively affect cellular attachment and survival. Furthermore, osteoblasts have been used with similar surface topographies as the ones generated in this Chapter (Figure 5) (Jung-Yen Yang et al., 2008). The striations created in the fabrication process of the micro-hollow fibres shown in this thesis are therefore expected to cause cellular alignment on neural cell cultures.

SEM imaging (Figures 5 and 6) highlighted the thin outer wall with a porous structure caused by the paraffin oil in the polymer dope. This is desirable as is facilitates the permeation of compounds in or out of the fibre, with shorter diffusion distances aiding this (Taskin et al., 2010). The highly porous outer, and particularly inner wall are not often seen in conventionally spun fibres. These methods have the inner wall in contact with the non-solvent bore fluid yield a less porous wall in general (Chen et al., 2015). The use of paraffin oil to create this sponge-like structure leads to an asymmetric

porous assembly, with pores becoming smallertowards the outer surface. Figure 5 shows the smooth surface, with randomly distributed pores, and it also highlights the slight irregularity in the thickness in the walls. This does not pose any issues in terms of nutrient distribution as cells attached to the fibres are to be fed from the outside. However, if these micro-HFs were to be used in another format such as a hollow-fibre bioreactor, this may need to be a consideration in terms of optimising feeding regimes. Oxygen diffusion has a limit of 100 - 200 μm, with these fibres having a radius of around 100 μm; this would not be a limitation to these fibres without considering porosity and tortuosity. The addition of the paraffin oil to the polymer dope usually leads to a reduction in mechanical strength of the micro-HFs, even with the sponge-like structure being formed (Puppi et al., 2012). This structure is preferred to the finger-like macro-void pores seen in other micro-HF fabrication processes as it improves the interconnectivity of the pores (Fashandi et al., 2015). The reduction in mechanical strength has been overcome through the introduction of the PCL into the polymer dope to confer flexibility into the fibre produced. (Bahareh Azimi et al., 2014).

NMR was conducted on the micro-hollow fibres to determine how the polymers were distributed. Upon examination, it was suspected that the outer fibre was formed primarily of PX whilst the inner was primarily PCL; this was due to the properties that were observed. During handling, the outer fibre was slightly flexible; however, it was prone to cracking when stretched. Conversely the inner fibre was much more flexible and was elastic in nature. NMR confirmed this hypothesis (Figure 7) showing close to a 90% pure inner fibre of PCL and outer fibre of PX. This slight mix in the outer fibre explains some increased flexibility when compared with PX alone, as this fibre was extremely brittle, with breakages occurring upon removal from the ddH_2O bath during fabrication.

This quaternary membrane-forming system, consisting of the nonsolvent (water), solvent (NMP), and the two membrane forming polymers (PX and PCL) is thermodynamically complex. The polymers mix well, indicated by their similar Hidebrand solubility parameters: PX, 18.61 $MPa^{1/2}$ (W.Welker, 2012) and PCL, 20.57$MPa^{1/2}$ (Madsen et al., 2015). Due to this, they can be considered as an intertwined network which is 'swollen' with the solvent and the nonsolvent molecules. During the initial stages in the phase inversion process, the movement of the polymers is negligible when compared to that of the water and NMP. Over time the polymers being to separate due to their relative entropy, having a very low entropy of mixing (Boom et al., 1994). This explains the inner fibre formation as the PCL moves away from the PX due to thermodynamic favourability. This phenomenon can be utilised effectively for tissue engineering applications as it can be exploited to achieve specific spatial distribution of two or more different cell types on different fibres and topographies for applications such as blood vessels or BB models.

The liquid permeation experiments performed on the PX:PCL micro-hollow fibres showed that the porous structure allows for flow of water through the fibre walls. This permeability of small water molecules would therefore allow for these fibres to be used to feed cells growing on the surface from the inside if used in a hollow fibre bioreactor format. Furthermore, as these micro-hollow fibres will be submersed in cell culture media (refer to Chapter 6), this morphological feature could prevent necrotic cores forming if used as a structure for organoid type structures (Grebenyuk and Ranga, 2019, Qian et al., 2019, Allenby et al., 2018).

4.3.2. Gellan Gum Fluid Gel Fabrication and Characterisation

Data from the literature was plotted and analysed (Figure 12) with the aim to determine how rotational rheometry differed from other mechanical testing techniques, when comparing mammalian brain stiffness. The data showed that there was no significant difference between the three techniques shown. In conclusion, the rotational rheometry data was presumed to be comparable to the AFM data from Moeendarbary et al. (2017). There is a wide range of rheological outputs throughout the literature in terms of the CNS; however, this paper was very detailed and had the most extensive testing found. Further to the literature analysis, data was analysed from Moxon (2016), who conducted extensive work on the mechanical properties of GG fluid gels. Some of this data was graphed in order to gather an understanding of a starting concentration of GG to begin with, however, this was not fully accurate due to the different salt solutions the gels were created in.

The resulting material from fluid gel fabrication needed to be both mechanically relevant and consistent. Initial production used a jacketed beaker with a water-cooling system. However, fluid gels set (crosslinked, gelated) too quickly, which did not allow for time for the conversion of the hydrogel into a fluid gel through the consistent shearing throughout the gelation process (Figure 10). Fluid gels were then still produced in the jacketed beaker, without the water cooling, which was found to produce consistent fluid gels. There was a significant difference in the setting temperature of the 0.5% GG fluid gel whether it was cooled rapidly or ambiently. This highlights the mechanical differences between fluid gels and hydrogels produced with the same gelling agent and salts. Hydrogels forming a solid-like structure present a higher value of G' than the viscoelastic fluid gels have (Compaan et al., 2019). Initially,

gels were produced with PBS as the setting agent. It was found that 0.6% GG rendered the most mechanically relevant gel when its mechanical properties were compared to those found in the literature. This particular fluid gel was tested on cells and caused cellular detachment and death by anoikis. This was likely due to the lack of calcium in the fluid gel, which is known to be required for cell attachment (Paoli et al., 2013). Without calcium in the fluid gel, it is hypothesised that the osmotic gradient formed forces the calcium out of the fluid gel, which would affect the cellular attachment, but also, would stiffen the gel by introducing divalent cations into the gel which set the gel exponentially more than monovalent cations (Juming Tang et al., 1995). These fluid gels were also imaged through SEM in order to get a small understanding of how they are structured. This required the gels to be dehydrated through freeze-drying. Although the freeze-drying process would have altered the structure, some level of organisation was likely conserved. The SEM images (Figure 11) show a ribbon like structure, with distinct spaces between them, which are likely to be deflated pockets of hydrogel, known to form in fluid gels. They also appear to be similar in structure to GG hydrogels which have been imaged by SEM in the literature (Rupenthal et al., 2011a, Rupenthal et al., 2011b). The small processes that can be seen off the main structures are the characteristic hair-like projections seen in fluid gels. These are where the fluid gel gains structure, as these projections interact with each other with weak forces, allowing for the fluid gel's viscoelastic properties. These also provide the fluid gel its self-healing properties, as they can break down and then reform.

With the lack of calcium seemingly causing problems, fluid gels were then prepared in a different salt solutions, one resembling the salts found in DMEM:F12. This was chosen as this is the base media for the majority of the cell lines used in this work, from the SY5Ys to the iPSC derived CNS cells. Table 3 highlights the differences in the salt

concentrations that were used between the PBS and the DMEM:F12, with the main one being the addition of the divalent cations, or magnesium and calcium. As previously stated, the addition of these divalent cations causes a drastic change in the structure of the gel (Juming Tang et al., 1995), and such the percentage of the GG used needed to be altered. Fluid gels made at the same concentration were unable to form fluid gels, as their setting time was too quick (data not shown) but upon reducing the GG concentration, fluid gels were fabricated within the desired parameters with regards to their mechanical properties. Rheological tests were performed (Figure 15) and compared, finding that the 0.25% and the 0.3125% GG fluid gels could be used for the damaged and healthy SC respectively. All gels tested had a similar breakdown point during the amplitude sweep. This suggests that all gels could be handled similarly, and therefore could be pipetted when required, allowing for their precise uses. This feature was a requirement, as the eventual goal was to incorporate a fluid gel in fluid gel system, allowing for a mechanical gradient to be placed into the model once cells had grown and potentially been damaged. This concept is similar to suspended layer additive manufacture (SLAM), and is useful for printing complex shapes within hydrogels (Jessica J. Senior et al., 2019). Furthermore, as there is a mechanical gradient, the ability to add different gels with varying mechanical properties is useful for altering the model in line with the research. As there has been differing opinions as to how the SC alters post injury, these types of tuneable, pipettable, self-healing fluid gels, can easily change in line with our current understanding of the SCI microenvironment (Boulet et al., 2011, Cooper et al., 2020, Moeendarbary et al., 2017).

Chapter 5

5. Planar (2D) Cell Culture and Differentiation of Neuronal Cell Types for SCI Modelling

5.1. Introduction

5.1.1. SH-SY5Y

SH-SY5Y cells are a neuroblastoma cell line developed which have been sub-cloned three times from the SK-N-SH neuroblastoma cell line (ATCC, 2022). They are used extensively as a neuronal model due to their differentiation potential into partially functioning neuronal cells (Xicoy et al., 2017, ATCC, 2022). These cells have a history of use in SC modelling, both for injury and other aspects, leading to their use in this work (J.Tucholski et al., 2001, Wei et al., 2021). This cell type is capable of large-scale expansion due to their ease of growth, cost effectiveness and their rapid doubling time (Ross et al., 1983, Kovalevich and Langford, 2013). Another advantage of this cell line over other neuronal cell lines is that it is derived from human cells, meaning that they express many of the same proteins and their isoforms, which are not seen in rodent model cell lines (Xicoy et al., 2017).

The differentiation potential of SH-SY5Ys has been widely studied, and countless papers have used various methods to differentiate them into a viable neuronal cell line (Kovalevich and Langford, 2013). This is mainly conducted through the use of retinoic acid (RA), a vitamin A derivative. RA is known to reduce cell proliferation and induce

differentiation (Kovalevich and Langford, 2013). The differentiation process synchronises the cell cycle, creating a more homogeneous neuronal-like population (Melino et al., 1997). Furthermore, the addition of RA to SH-SY5Y promotes their survival through the phosphatidylinositol 3-kinase/Akt pathway and Bcl-2 upregulation (Itano et al., 1996, Gracia López-Carballo et al., 2002).

The predominant differentiation process directs the cells towards a cholinergic neuron phenotype. This is seen by the increase in choline acetyl transferase (ChAT) and vesicular monoamine transporter (VMAT). Phorbol esters, another, less common, method of differentiating SH-SY5Ys alongside RA can push cells towards a dopaminergic phenotype. This has been utilised extensively in Parkinson's disease research as they have similarities with the dopaminergic neurons affected in this disease (Xicoy et al., 2017, Presgraves et al., 2004).

Once differentiation has occurred, there are many markers which can be used to identify them. SH-SY5Ys are positive for many mature neuronal markers, such as βIII-tubulin (Tuj) MAP2, synaptophysin, NeuN, SAP-97 and NSE. During this study Tuj was used as it highlights the cellular phenotype best. (Gracia López-Carballo et al., 2002, Lopes FM et al., 2010, Cheung YT et al., 2009)

5.1.2. iPSCs and NPCs

iPSCs are a useful tool for forming human *in vitro* models both in 2D and 3D. with their potential to be differentiated into any cell in the body they can be used to mimic a wide variety of tissues. For the CNS, differentiation goes through NPC stage, this is a pluripotent stem cell with the potential to differentiate into neurons, glia and

oligodendrocytes. (Hong and Do, 2019). They are readily used for their differentiation potential, which allows complex structures to be formed.

In this Chapter, the proliferation and differentiation of neuron-like and neuronal cell types in planar culture will establish the basis for their culture in a 3-dimensional environment towards the mail goal of this thesis – modelling the extracellular setting in SC and SCIs. Therefore,

All experimental methods regarding these cells are outlined in section 3.1.

The aims for this chapter are to:

1. **Determine the 2-dimentional growth and differentiation potential of neural cell lines and iPSC derived neural precursor cells and neurons.**
2. **Understand the biocompatibility and toxicity of the biomaterials on the 2-dimensional cell cultures**

5.2. Results

5.2.1. 2-Dimensional Cell Line Culture

As a proof of concept, two main neuronal cell lines were tested, NG108s and SH-SY5Ys. NG108s were first used as a standalone cell type without any differentiation potential. As the project aims to incorporate iPSC-derived CNS cells, which require laminin coating, the growth of SH-SY5Ys was tested on the same coating in order to determine attachment to the micro-hollow fibres later on (see Chapter 6). SH-SY5Ys were grown both differentiated and undifferentiated in 2D (regular planar culture in tissue culture plastic flasks and well plates) as a control in order to determine if growth was altered when cells were expanded on micro-hollow fibres as a scaffold for cellular alignment. As seen in Figure 17, it was found that the doubling time over 120 hours in 2D was around 28 hours when undifferentiated. When differentiated, cells doubling time over 72 hours increased over 2-fold, showing the effect of the RA on cell growth (Figure 17). The SH-SY5Ys cell line use had also been genetically modified to express GFP (George et al., 2018).

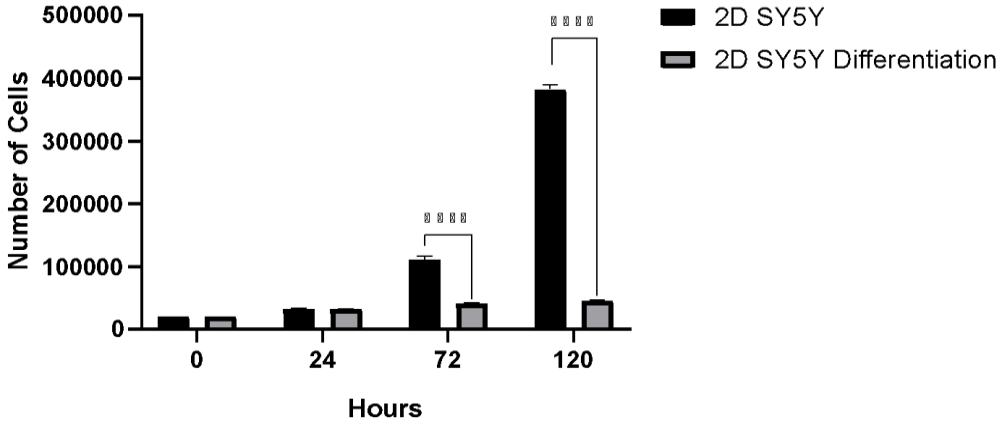

Figure 17: Growth curve of undifferentiated SH-SY5Y cells versus differentiated SH-SY5Y cells. Cells were seeded at 20,000 cells per cm^2 and counted at 24-, 72- and 120-hours post-seeding. RA was added after 24 to begin differentiation (N = 3). Statistical analysis was performed using ANOVA with Sidak's multiple comparisons post hoc test.

Figure 17 shows a significant reduction in cell proliferation when SH-SY5Ys were differentiated using RA, both 72 hours and 120 hours after seeding.

In the three-dimensional growth experiments that will follow on Chapter 6, cells were to be attached to micro-hollow fibres, with the micro-hollow fibres being glued onto 3D-printed squares (see Chapter 3, Section 3.2.6.) in order to facilitate sample handling. The 3D-printed squares were then placed into square bacteriological plates for cell culture. This process allowed for tracking of the cells over time avoiding undesired movement of the scaffolds – micro-hollow fibres are very small and light, and therefore floated and swirled randomly when added to culture media. In order to determine the toxicity of various types of commercially available glues, the micro-hollow fibres, squares and glue were tested with an AlamarBlue® assay as shown in Figure 18. SH-SY5Y cells were seeded at 20,000 cells/cm^2 in 24-well plates and test compounds an materials were incubated with the cells for 24-hours.

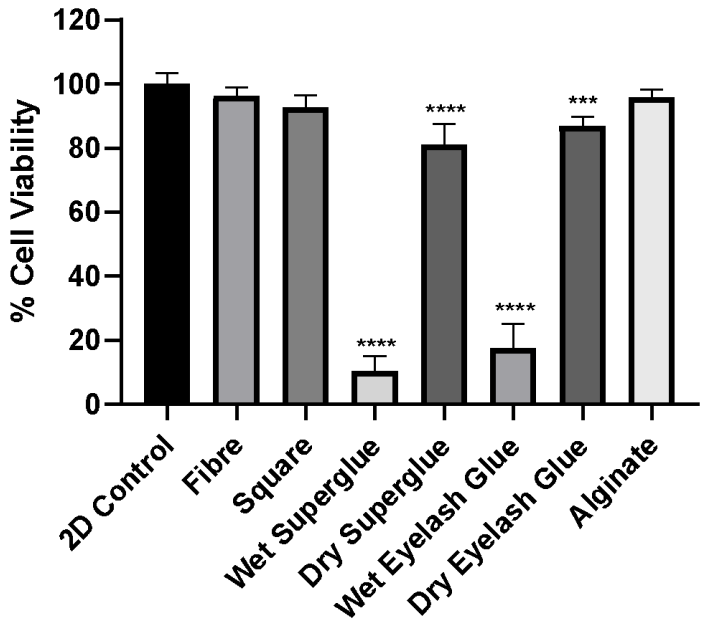

Figure 18: AlamarBlue® assay assessing cell viability. SH-SY5Ys were seeded with their respective condition, 10% AlamarBlue® was added to the respective media and normalised against fully reduced regent and the media to work out a % viability (N=3 independent repeats). ANOVA with Tukey's multiple comparisons was done comparing each condition to the control (regular 2D culture, black bar).

It was found that all types of glues, when wet, were very toxic as indicated by the significantly reduced viability of cells. However, the reduction of viability was not statistically significant when the glues used were dried. It was also observed that eyelash glue had a much faster drying time than superglue, which had varying drying times. Cell viability for the superglue and eyelash glue dropped to 10.5% and 17.5% respectively when wet but remained at 81.1% and 87% when they were dry. These were still significant drops in cell viability, and as such they were no longer used. It should be noted that the micro-hollow fibres and 3D-printed squares did not reduce cell viability significantly, with only a slight drop to 96.3% and 92.3% viability respectively, hence indicating the appropriateness of micro-hollow fibres for cell culture from a biocompatibility point of view. The results shown in Figure 18 also confirm that the presence of 3D-printed squares to hold the micro-hollow fibres in place did not have an effect on cell viability. It was then decided that alginate could be a suitable option to glue the micro-hollow fibres in place, due to its biocompatibility. Alginate gels were prepared by dissolving 5%(w/w) alginate powder (Sigma-Aldrich) in ddH_2O, followed by addition of 200mM KCl to chemically crosslink the gel. As can be observed in Figure 18, alginate as a glue showed little cell toxicity as evidenced by the minor reduction in cell viability. However, it was not a long-term way to stick the fibres to the squares for the experiments performed in Chapter 6 due to fibre detachment.

5.2.2. PSCs Form Colonies Which Express Oct4 and Sox2

Two pluripotent cells lines were used for the CNS cells. The first is a genetically engineered embryonic stem cell line with a GFP tag on Olig2, as such it should fluoresce green when the motor neuron precursor marker Olig2, is expressed. This line was able to make NPCs.

The second line used was LN5 iPSCs, which are formed from cord blood taken from a neonatal male. This line formed the characteristic colonies that are seen with PSC lines, with smooth edges and no cell differentiation (Figure 19). Furthermore, staining of colonies showed both stains to have over 98% of cells to be positive for iPSC markers, Oct4 and Sox2.

5.2.3. Neural Induction

iPSCs underwent neural induction using a modified method from Shi et al. (2012), in which they generate NPCs through formation of neurectoderm, then they are able to differentiate further into the excitatory neurons and motor neurons. NPC differentiation was characterised through ICC staining for Sox2, Pax6 and Nestin. Cells were also stained for Ki67, Tuj and MAP2.

These cells were grown on both mouse and human laminin to determine if mouse laminin, the cheaper option, was suitable for these applications. Expression of Sox2, Pax6 and Ki67 was quantified as a proportion of DAPI for each coating.

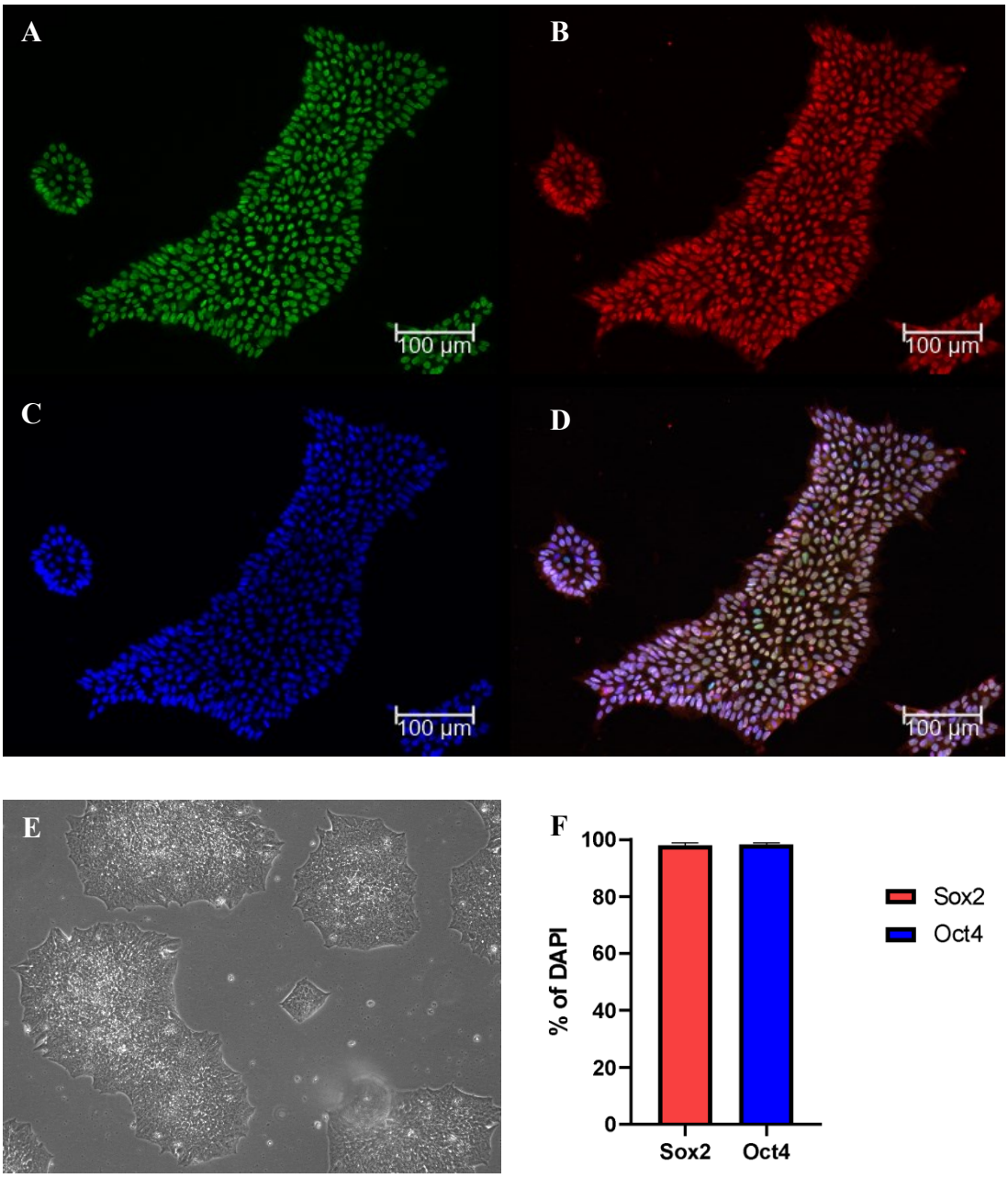

Figure 19: Representative ICC staining and quantification of LN5 iPSCs. LN5 iPSCs were cultures and expanded on human vitronectin in Essential 8 media. A, Sox2, B, Oct4, C, DAPI, D, merge, E, phase contrast, F quantification of iPSCS expression of Sox2 and Oct4 as a proportion of DAPI, n=3 ± SD, a t-test was performed, no statistical significance.

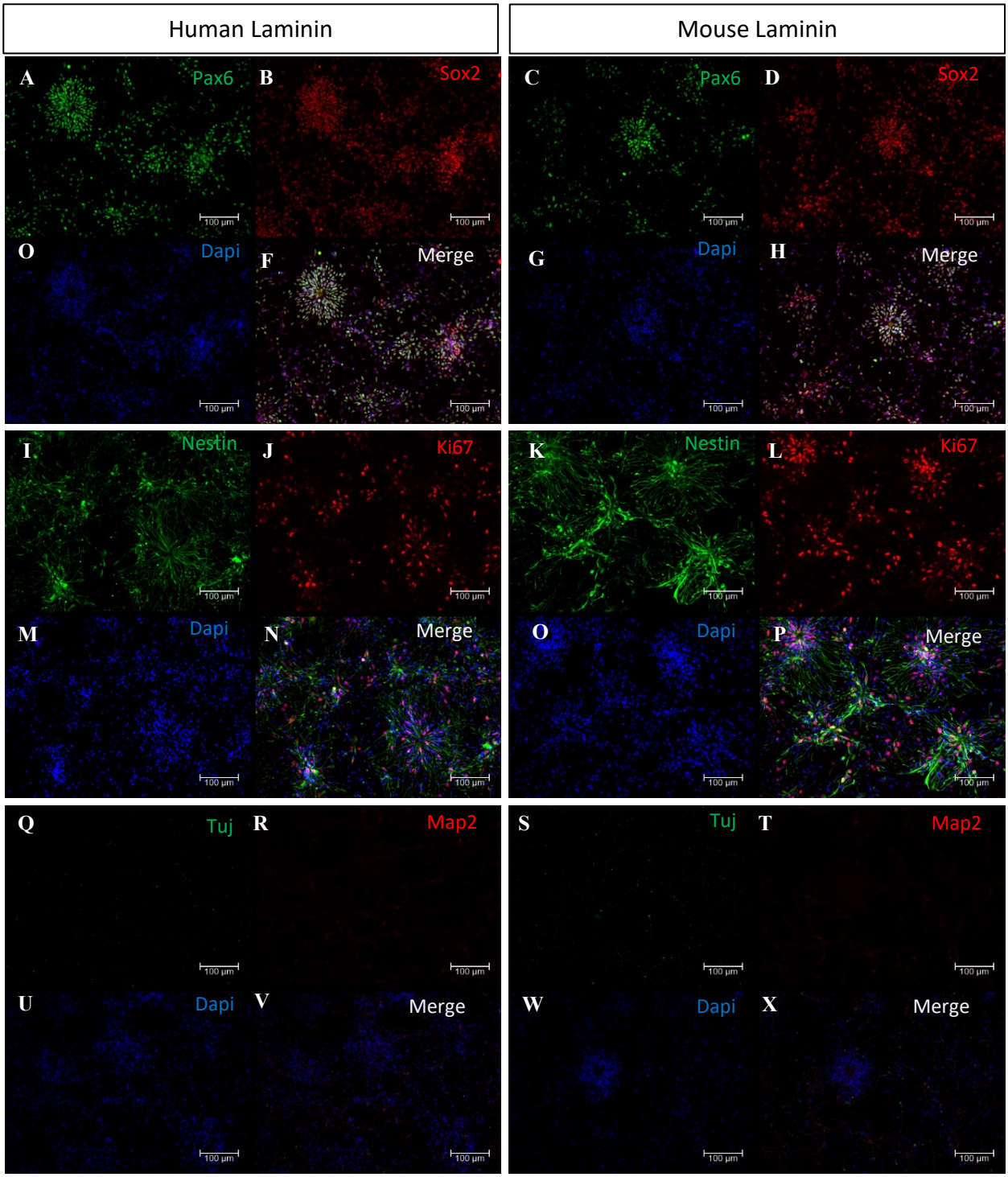

Figure 20: ICC of LN5 NPCs on human and mouse laminin. A, B, E, F, I, J, M, N, Q, R, U, V, mouse laminin C, C G, H, K, L, O, P, S, T, W, X, human laminin. A and C show Pax6 staining, B and D show Sox 2 staining I and K show nestin staining, J and L show Ki67 Staining, Q and S show Tuj staining and R and T show MAP2 staining. DAPI is shown in E, G, M, O, U and W. Merges are shown in F, H, N, P, V and X. Images are representative of n=3, taken at 20x objective, scale bar is 100µm.

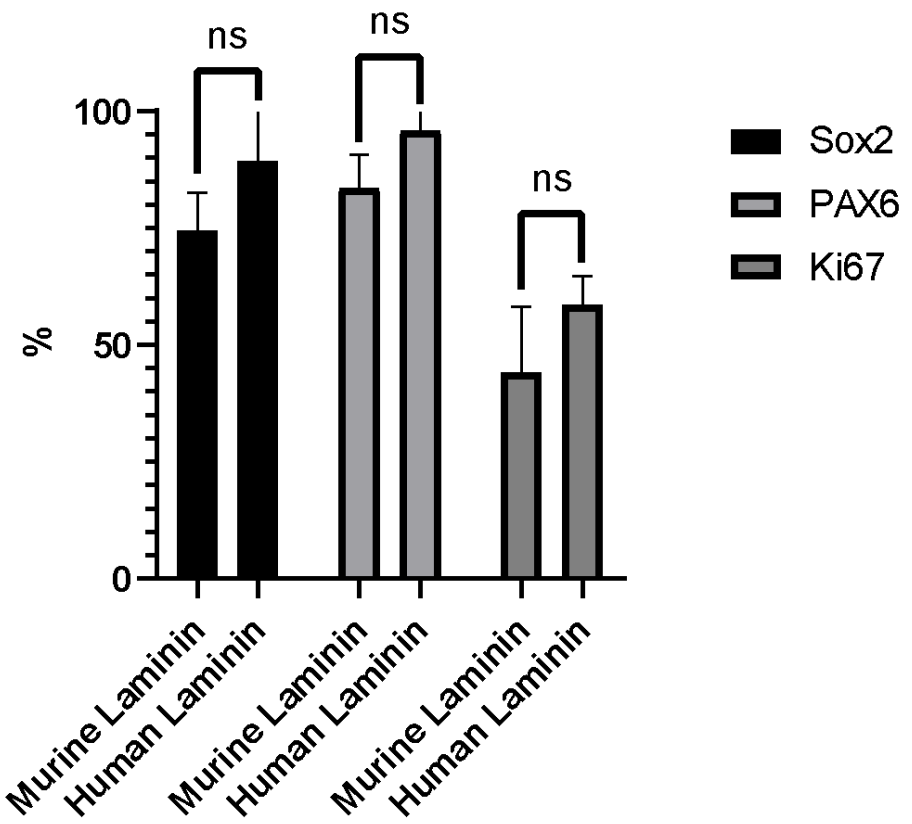

Figure 21: NPC ICC quantification. NPCs were stained with Sox2, Pax6 and Ki67 and positive cell expression was quantified as a percentage of DAPI, n=3 SD shown with ANOVA and Sidak's multiple comparisons.

Results showed that for all three stains, there was a non-significant reduction in expression when going from human laminin to murine. Sox2 had a 15% change in expression, Pax6 had a 12% change and Ki67 had again a 15% change. As the change was non-significant, and the price difference was an issue, all further work was carried out with murine laminin. Nestin (Figure 20) was not quantified due to the morphology of the cells, however, it was present on both coatings. The neuronal cytoskeletal protein, Tuj and MAP2 were very weakly expressed at this NPC stage. Phenotypically, the NPCs had the distinct neural rosettes which are unique to NPCs, mimicking the neural tube found in development. These NPCs could then be taken forward to be differentiated into the motor neuron precursors and then mature motor neurons, as well as excitatory neurons.

5.2.4. Motor Neuron Differentiation

Olig2-GFP ESCs were initially wanted to be used to form motor neurons. However, some difficulties arose. Differentiation was attempted three times, with limited success, with only a small fraction of the cells expressing the Olig2-GFP tag before the first passage (Figure 22). After this, cells were cultured for 30 days, with very little increase in the expression of the GFP tag (Figure 23). Alongside this, differentiation was undertaken in the LN5 iPSCs, to confirm whether the tag was working correctly, and for more complex co staining (Figure 24). It was found that through multiple attempts, Olig2 and HB9, the MNP and motor neuron markers were not substantially expressed in the cultures. In addition to this, the cells were still expressing the immature NPC markers Sox2 and Pax 6.

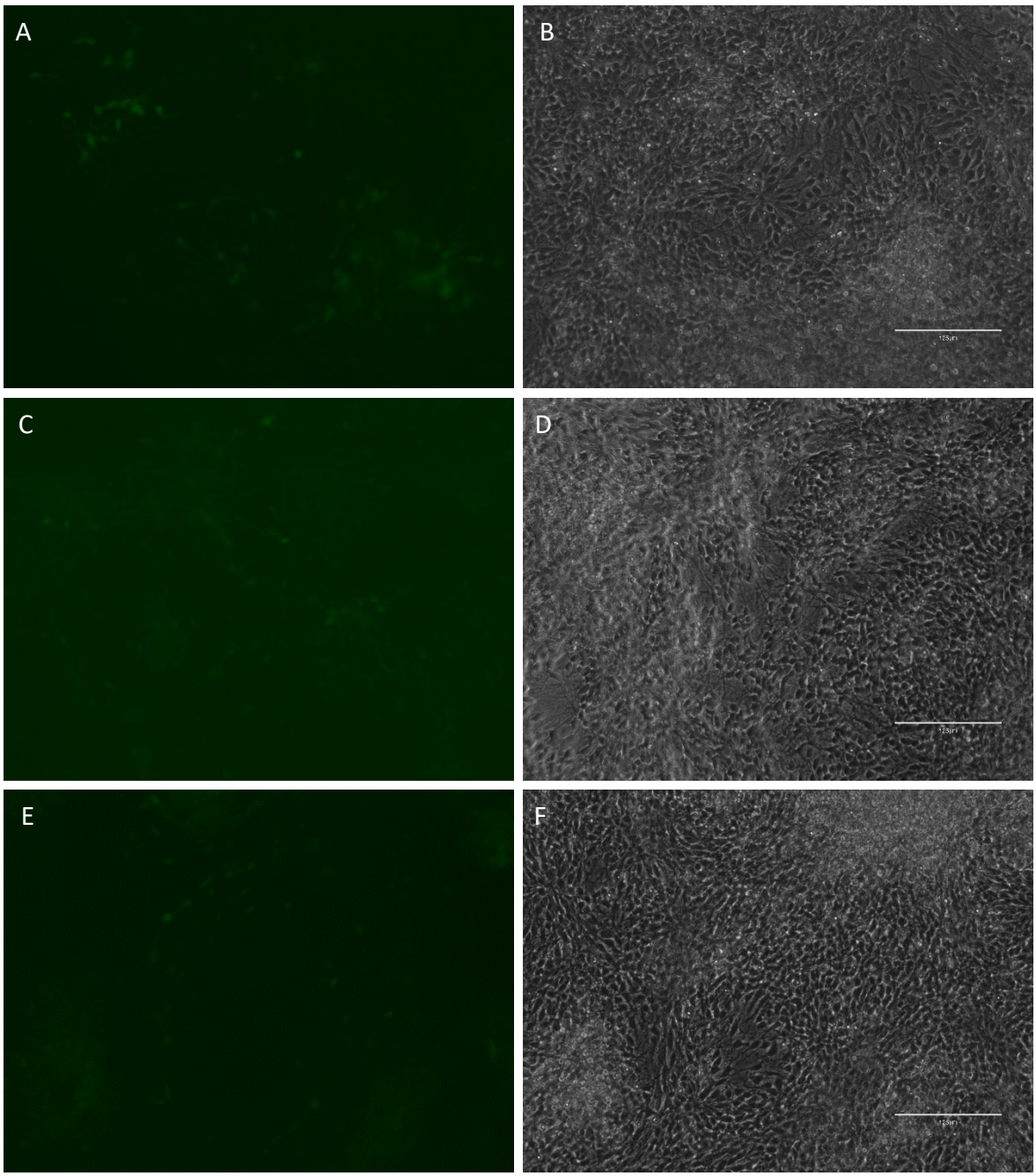

Figure 22: Motor neuron induction. An Olig2-GFP reporter line was used to test a motor neuron induction. Images taken at day 2 (A-B), day 4 (C-D) and day 6 (E-F) on a fluorescent EVOS M5000 scale bar = 125µm.

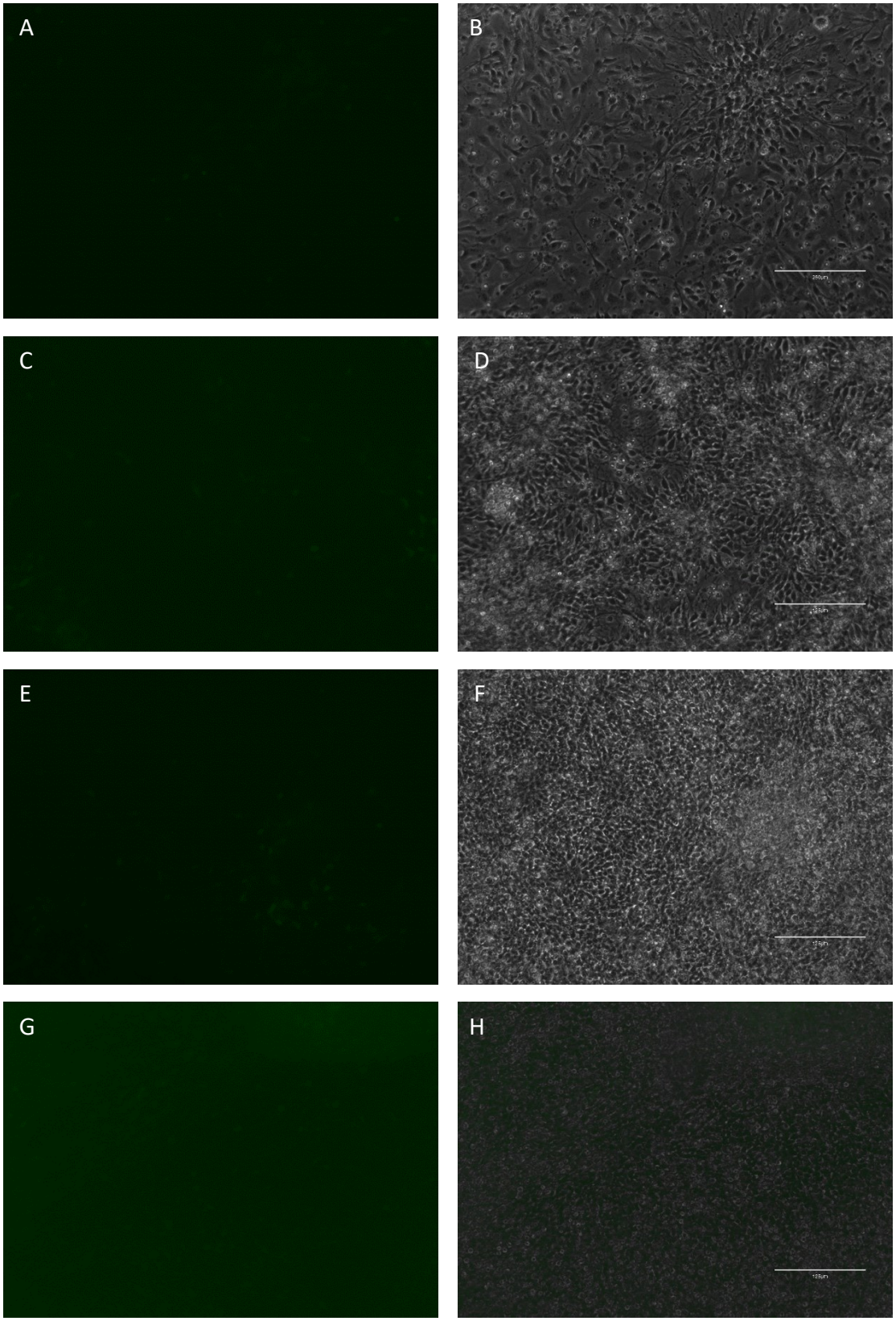

Figure 23: Motor neuron induction. An Olig2-GFP reporter line was used to test a motor neuron induction. Images taken at day 1 (A-B), day 4 (C-D), day 9 (E-F) and day 12 (G-H) after being passaged. Left hand images appear blank due to a lack of GFP expression. Images taken on a fluorescent EVOS M5000 scale bar = 125µm.

Tuj and S100β staining in Figure 24, showed that cells were all expressing the neuronal marker, Tuj, and there was some expression of the mature astrocyte marker, S100β. However, another main issue was around attachment. Cells did not seem to stop their proliferation and as such overgrew the culture, peeling off as a sheet. This slowed progress, meaning many differentiations did not reach their desired and point. Figure 24 (panel I) shows some of the pealing, with areas around the cells being bare due to detachment and death. Due to time constraints caused by the COVID-19 pandemic, and the cost of motor neuron differentiations, this was abandoned, and excitatory neurons were used in their place. Excitatory neurons were chosen due to their similar morphology and their comparative ease and cost reduction.

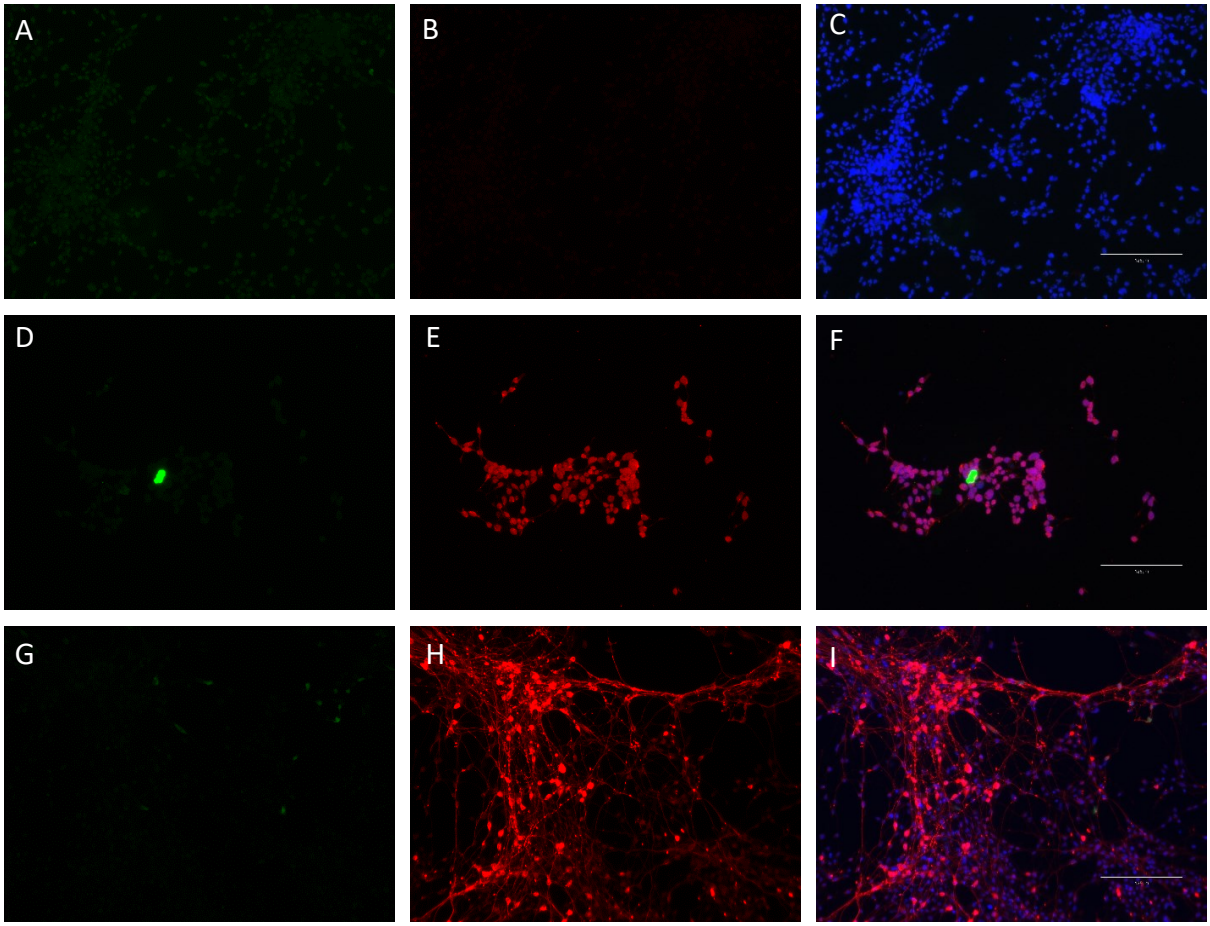

Figure 24: LN5 iPSC Motor neuron differentiation at 30 days post passage. A, Olig2, B, HB9, D, Pax6, E, Sox2, G, S100β, H, Tuj. C, F, I Merge. Images taken at 20x objective on Leica-epifluorescent microscope, scale bar 125µm.

5.2.5. Excitatory Neuron Differentiation

Excitatory neurons were differentiated from LN5 iPSCs, using a method optimised by Dr James Crowe (personal communication, Aston University), wherein NPCs are forced to synchronously differentiate through the use of the gamma-secretase inhibitor, Compound-E. This causes cell cycle arrest leading to neurons without glial contamination. Neuronal differentiation was monitored for 12 days, and images were taken the monitor differentiation (Figure 25). The images show an increase in cell connectivity, with a noticeable rise in the number of neurites seen between days 3, 7 and 12, which will be quantified in the following Chapter (Chapter 6) as a 2D control. The CellTrackerTM Green was imaged to determine if the dye remained stable during the ICC staining process. This was then quantified further in Figure 26.

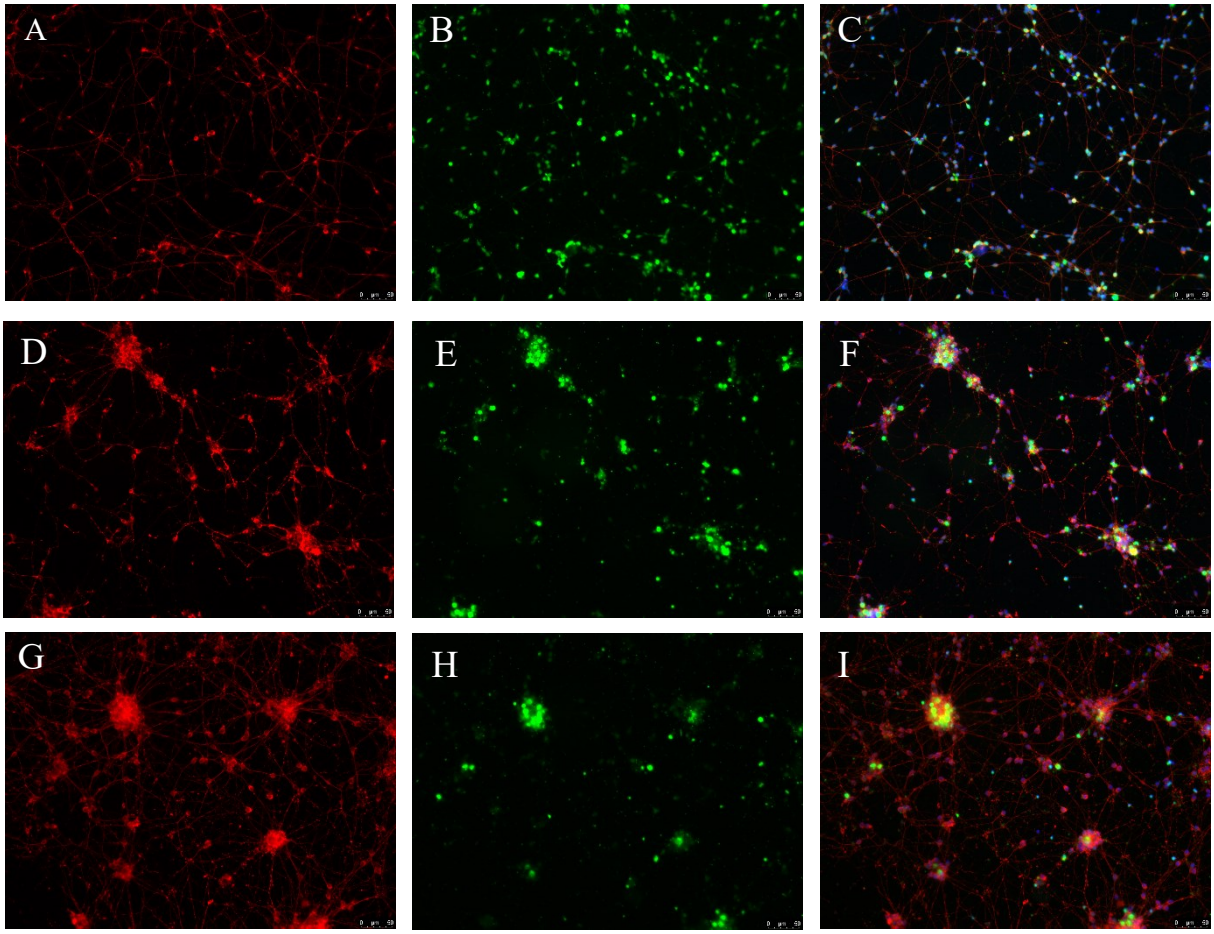

Figure 25: ICC of neuronal differentiation from LN5 iPSCs. A, D, G show Tuj staining, B, E, H show CellTrackerTM Green staining and C, F, II show the merge with DAPI included. Images taken at 3 days (A-C), 7 days (D-F) and 12 days (G-I) after treatment with Compound E treatment began. Compound E treatment lasted for 7 days. Representative images from n=3, scale bar is 50µm, taken on Leica epifluorescent microscope.

5.2.6. Live Cell Tracking

The micro-hollow fibres used in the following chapter for cellular alignment are opaque, which causes issues in terms of imaging. The GFP tagged SH-SY5Y were used to counteract this problem as they can be seen with live fluorescent microscopy. This was another reason for the choice of the Olig2-GFP reporter line. Live CellTrackerTM Gree dye was chosen as a non-toxic alternative to be used during neuronal differentiation of NPCs. This was tested to determine its longevity in these cells over the 7-day

differentiation and up to day 12 (Figure 26). It was found that although the brightness was reduced over time, it was not a significant decrease. The images also show the location of the dye becoming more centralised in the soma of the cells rather than the extensions over time.

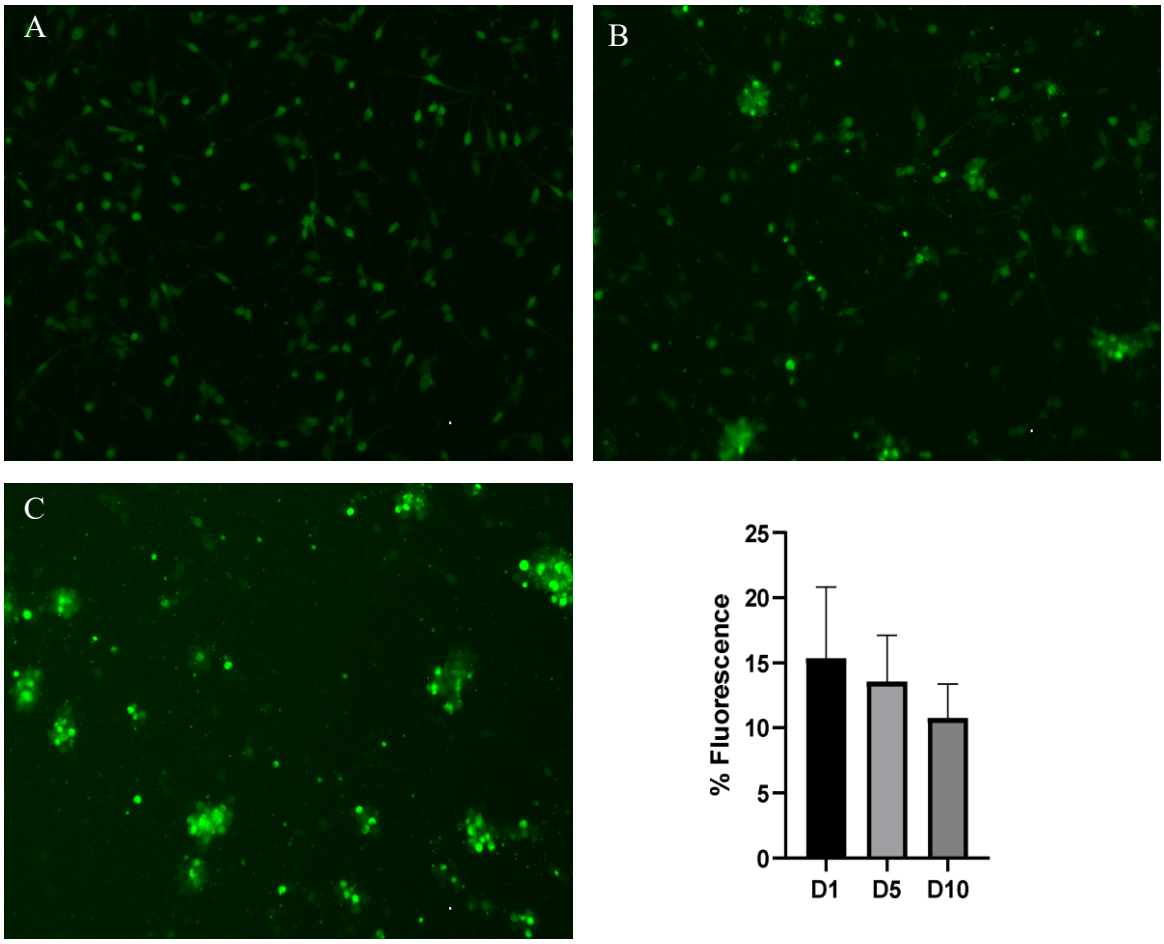

Figure 26: Images and quantification of CellTrackerTM Green dye in culture during neuronal differentiation. CellTrackerTM Green was used in order to be able to see the NPCs whilst on the fibres. This was assessed in 2D to determine if it would last throughout the 7-14 day cultures. Cells were imaged after 1, 5, and 10 days, and analysed on ImageJ to determine how many pixels remained above the chosen threshold. n=3 An Anova with Tukey's multiple comparison post hoc test was carried out finding no significant difference. Scale bar 50 µm

5.3. Discussion

The results presented in this chapter demonstrate SH-SY5Y cells can be reliably differentiated in 2D to neuronal-like cells, and LN5 iPSCs can be differentiated to excitatory neurons with a similar morphology to motor neuron cells.

5.3.1. 2D Growth of SH-SY5Y Cells

SH-SY5Y cells were grown in 2D to determine how their growth was affected during the differentiation process. The results obtained in this Chapter were then used to ensure an appropriate number of cells was seeded on the micro-hollow fibres in the following Chapter. The ideal situation would allow cells to form networks, whilst still maintaining space to be able to assess individual cell morphology. The 2D cell growth kinetics observed on the pORN/Laminin coating were consistent with the literature as to how they grow on TCP (Figure 17) (Kovalevich and Langford, 2013, Feles et al., 2022).

5.3.2. Cell Viability for 3D Culture Preparation

In order to determine the growth of the SH-SY5Y cells on the micro-hollow fibres, each individual element of the 3D culture was tested in order to determine if they were toxic to the cells. There are difficulties in manually counting cell numbers when adherent cells are placed in a three-dimensional environment, and therefore a surrogate measure of viability was necessary. Viability measurements were performed via fluorescent measurements through an AlamarBlue® assay. This assay was chosen over other cell viability assays as it is not an end point assay, and the media is added

for 4 hours and then removed. The benefit of this is that would theoretically be possible to do this assay on the cultures with the GG fluid gels present. This was not used here, but literature suggests that it can be done with some modification to the protocol (Bonnier et al., 2015). The substances that are added to the culture are the micro-hollow fibre itself, a plastic polymer square to attach the micro-hollow fibre for easiness of handling and imaging, and a glue to stick the micro-hollow fibre to the ring. The micro-hollow fibre itself is made of well-known biocompatible polymers, PX and PCL. These are known to have minimal cytotoxic effects, especially as PX is used to fabricate tissue culture plastics (Salgado et al., 2012, El Fray et al., 2006). It was found that although there was a slight reduction in cell viability, it was not significant. Similarly, the polylactic acid (PLA) which was used to form the mounting ring caused no significant cell death.

Cell culture compatible glue was not easily accessible; however, non-toxic glues such as food-safe silicon glues were not suitable for this application as they took too long to dry. The next option that was investigated was surgical super glue, but it was not possible to purchase it due to its high cost. Finally, commercially available superglue was tested, as it dried quickly, was sterile and was cheap and easily accessible. When added to cultures it caused a widespread and significant amount of cell death quickly; however, when completely dried, this toxic effect was drastically reduced whilst still causing a significant amount of death. As the results show in Figure 18, the standard deviation (error bars) is quite large, and therefore it was assumed that the superglue may not have been 100% dry in all cases even after 24-hour drying times. In order to try to shorten the drying times, eyelash glue was tested as it has a drying time of a few seconds. Eyelash glue provided slightly better results with regards to cell toxicity, but there was still a significant drop in cell viability. It was therefore concluded that standard

glues would not be suitable for this application. When surgical grade glues are used *in vivo* and *in vivo*, there is still some cell death surrounding the application area (Pascual et al., 2016, Thumwanit and Kedjarune, 1999). As such, alginate was selected as an alternative. Viability testing showed that there was only a slight decrease in cell viability. This result is consistent in the field, as alginate has been used extensively for years as a biocompatible hydrogel (Urzedo et al., 2020). Micro-hollow fibres slowly detached throughout the culture time, which meant that they could not be used in their intended ways. These reasons meant that the idea of mounting the micro-hollow fibres on the squares was abandoned, and micro-hollow fibres were fixed and imaged individually rather than tracking cellular growth over time. Additionally, a Sartorius IncuCyte™ (Sartorius) was going to be used for live imaging. The challenge was that, on this piece of equipment it is not possible to choose where the images are taken as the software has pre-sets for the location of image capture, meaning that it was not useful for tracking cell growth.

5.3.3. iPSCs Could Efficiently Generate NPCs

LN5 iPSCs were confirmed to express pluripotentency associatedmarkers through ICC of Oct4 and Sox2 with a purity of over 98% seen (Figure 19). The markers of Sox2 and Oct4 were chosen as they have been shown to be the most reliable markers to prove pluripotency. Gene analysis using PCR has previously shown that Sox2 and Oct4 are highly expressed in iPSCs whilst having reduced expression in other cell types (Bharathan et al., 2017). Once this was confirmed, these could then be differentiated to NPCs through a modified version of commercially available media from Chambers et al. (2009). This process was carried out in 2D as this line (LN5) had been used previously with a very similar method within the lab by Dr James Crowe (personal

communication, Aston University). This proved successful and was the method used going forward. 3D neural induction has been suggested to lead to a purer NPC population. The method chosen here had been proven to create functional neurons through neuro and electro-physiological methods. This proved that this 2D method was sufficient for this study (Chandrasekaran et al., 2017).

Sox2 was again used to identify NPCs as they retain expression of this transcription factor, with it being an early marker of CNS development, maintaining this precursor phenotype and simultaneously inhibiting further differentiation (Graham et al., 2003). Sox2 has a dual function wherein it is necessary for maintaining pluripotency, but it can also function as a neural factor, with this change occurring depending on the environmental inputs. Furthermore, Oct4 and Pax6 may also have functional interactions with Sox2 facilitating this change (Zhang et al., 2019). In addition to this, Pax6 is another transcription factor which is expressed by *in vivo* human NPCs, showing that these iPSC derived NPCs have similar protein expression (Zhang et al., 2010). Expression of these markers for this iPSC line was assessed (Figure 21), showing a high purity of over 75% on murine laminin and over 89% on human laminin.

Further to this, Ki67 was used to determine cell proliferation, which NPCs should be positive for, as they have not yet become post-mitotic as is the case for differentiated neurons, both iPSC derived (Kim et al., 2012) and primary human (Seki et al., 2019). NPCs on human laminin, again had 59% of cells expressing Ki67, compared with 44% on mouse laminin. These difference, although not significant, shows that human laminin may be the preferred substrate for NPC expansion and differentiation. Cells were also stained for Nestin (Figure 20), which was not quantified due to the morphology in which it presents but was highly expressed throughout. Finally, cells

were stained for the mature and maturing neuronal cytoskeletal proteins, MAP2 and Tuj respectively, these had low levels of expression, showing the cells were still in their immature state.

5.3.4. Motor Neuron Differentiation

Motor neurons are the prominent data transmitters in the spinal cord. As such they were the desired cell type to use in this model (Stifani, 2014). The Olig2-GFP reporter line was chosen to be used as they would provide instant feedback as to whether the cells were differentiating correctly, whilst also having a fluorescent tag so they could be imaged on the opaque micro-hollow fibres. Olig2 is a marker used to distinguish motor neuron precursor (MNP) cells, which then is reduced again when they mature. The mature marker chosen was HB9. HB9 was stained for using ICC to determine if mature motor neurons were present in culture (Shimojo et al., 2015). Differentiation was first carried out in 2D to ascertain whether the methods chosen were appropriate. Multiple variations of methods were chosen, resulting in minimal Olig2 expression (Figures 22 and 23). One of the main issues found was that the cells did not exit their cell cycle, which should happen with the introduction of RA. The addition of RA causes MNPs to express GDPD5, whose downstream activation leads to exiting of the cell cycle in order to begin the maturation to motor neurons (Stifani, 2014, Rao and Sockanathan, 2005). Olig2 expression was incredibly limited in this reporter line, and therefore the method was again tried with the LN5 iPSC line (Figure 24). Again, HB9 marker expression was not seen, and cells did not appear to exit the cell cycle. Similar to excitatory neurons, which are treated with a gamma-secretase inhibitor in order to get them to exit the cell cycle, the presence of RA should have this effect. The fact that the cell cycle was not exited led to excessive over-growth of the cultures, which may

have caused an issue with the differentiation as well as causing cellular detachment, meaning that cells never got through the full differentiation protocol. Due to the length of time (approximately 45 days) and the cost of conducting this protocol, and with extra time limitations added due to the COVID-19 pandemic, the motor neuron differentiation was stopped, and excitatory neurons were used instead due to their similar morphology.

5.3.5. Synchronous Neuronal Differentiation

LN5 NPCs were synchronously differentiated into excitatory neurons using the gamma-secretase inhibitor Compound E. This acts on the Notch/Delta signalling pathway, leading to an extremely pure population of neurons. Compound E was added for 7 days, being optimised for this cell line by Dr James Crowe (personal communication, Aston University), leading to the neurons seen in Figure 25. Neurite growth appeared to increase throughout the 12 days during which cells were imaged. Tuj expression increases with neuronal differentiation, with it being almost exclusively neuronal in expression, as cells become more mature and further down the neuronal lineages, Tuj expression increases, and more neurite outgrowth occurs (Katakura et al., 2009, Katsetos et al., 2003).

5.3.6. Cell Tracker Green Remained Stable During Differentiation

As the PX:PCL micro-fibres to be used are opaque, cells being fluorescent in some way allows their visualisation when they are attached to a surface, which is otherwise not possible. This was overcome with the SH-SY5Y cell line as they have a GFP tag in them. With the iPSC-derived neurons, the addition of a cell tracker dye was needed.

CellTracker™ Green was chosen as it is non-toxic and can typically last 3-6 cell cycles (ThermoFisherScientific, 2022). As iPSC-derived neurons are post-mitotic, it was hypothesised that the dye would last longer as it would not be diluted out into daughter cells. This was found to be correct; the cells retained their dye in the soma, as shown in Figure 26. However, it was no longer present in the neurites. This was likely due to their size, as the neurites are so thin, the dye was concentrated at the soma and was therefore no longer visible in the cells' extensions.

Chapter 6

6. Biomaterials in action

6.1. Introduction

Tissue engineering for repair, regeneration and recreation of physiologically representative and functional tissues involves integrating certain physical scaffolds to guide cell growth, particularly when cell orientation is essential. In the case of the central nervous system (e.g., spinal cord), the aim of these scaffolds is to allow for signal conduction to be resumed, while retaining cells in a parallel configuration (Alizadeh et al., 2019). For instance, SC motor neurons are the longest cell type in the human body and encouraging their growth to extreme lengths whilst maintaining their morphology in vitro is a challenge (Stifani, 2014, Hagemann et al., 2022). Scaffolds may be used to generate highly organized structures that resemble the in vivo (Lizarraga-Valderrama et al., 2019, Miller et al., 2002, Rajnicek et al., 1997). Recently, similar biomaterials have been able to achieve iPSC derived motor neuron alignment over 1 cm (Hagemann et al., 2022)

Methods of achieving cell alignment *in vitro* include mechanical stimulation such as uniaxial strain and stretching of substrates, electrical stimulation, and the manipulation of the mechanical properties of the substrate, such as stiffness and surface morphology through the introduction of specific topographic features to support contact guidance (Vandenburgh and Karlisch, 1989, Engler et al., 2004, Tamiello et al., 2016, Bettinger et al., 2009, Wilkinson et al., 2002, Hosseini et al., 2012, Hume et al., 2012,

Hagemann et al., 2022). Contact guidance from surface topography has been shown to be a result of both the geometry and size of surface features, with parallel grooves the most widely used feature to align muscle cells in a uniform direction (Hume et al., 2012, Ostrovidov et al., 2014).

The application of hollow fibre membrane technology is very well established in the field of tissue engineering (Eghbali et al., 2016). Hollow fibre membranes constitute, among other kinds of three-dimensional (3D) constructs, the scaffolds required for cell proliferation and differentiation both as a platform for scaled-up expansion and maintenance of culture for the production of viral vectors and recombinant proteins (hollow fibre bioreactors), and as support structures for tissue repair. A 3D culture scaffold where cells are grown around hollow fibre membranes holds a number of advantages over traditional planar (2D) cultures, since they are able to better represent the in vivo environment and the complex cellular interactions that occur between cells and their surroundings (Wung et al., 2014). The macro-architecture of the hollow fibre membrane provides a highly permeable barrier that can act as a scaffold for adherent cells while maintaining their constant requirements in terms of oxygen and nutrients (De Napoli et al., 2011).

The changes in the mechanical microenvironment are an important factor in the cellular behaviour after SCI. Particularly, the differentiation of NPCs is highly dependent on the mechanical cues that they receive from their surroundings. Here, we will use GG fluid gels to closely mimic such microenvironments in both healthy and injured tissue.

The aims for this chapter are to:

1. **To perform cell culture of all selected cell lines on micro-hollow fibres.**
2. **To determine the degree of alignment of all selected cell lines when cultured and differentiated on micro-hollow fibres.**
3. **To include mechanically relevant gellan gum fluid gels surrounding the 2-dimensional cultures and the micro-hollow fibres.**
4. **To ascertain the effect of the gellan gum fluid gels surround the 2-dimensional and 3-dimensional cultures in terms of cell alignment and wound closure and migration.**

6.2. Results

6.2.1. Multiple Cell Types Align Along Micro-Hollow Fibres

As a proof-of-concept various cell types were tested to see the effect of the micro-hollow fibres fabricated in Chapter 4 on cell directionality and alignment. Before gaining access to the GFP-SH-SY5Y cell line and prior to starting work on the PSC lines, NG108-15 cells and OECs were used to test general attachment and alignment initially. NG108s and OECs were cultured individually and as a co-culture for 6 days, and stained with Live/Dead staining on days 3 and 6. Images showed that all cell types were able to attach to the micro-hollow fibres, and low numbers of dead cells (in red) were seen through a Live/Dead assay (Figure 27).

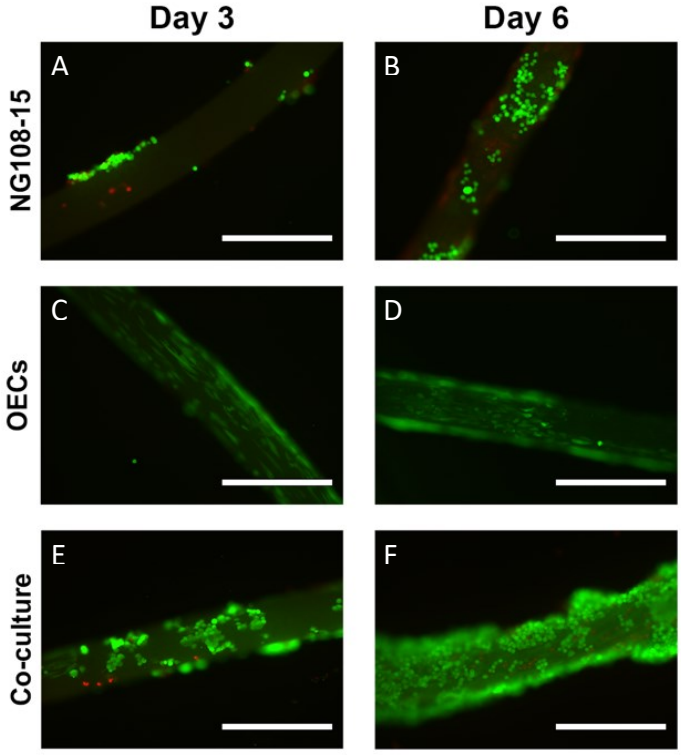

Figure 27: Fluorescent micrographs of Live/Dead stained NG108-15s, OECs, a co-culture of NG108-15s and OECs (calcein-AM/ ethidium homodimer (EH)). All cell types were grown on micro-HFs for 6 days in three independent biological repeats each. Images were taken at day 3 and day 6. Green cells are live cells (Calcein-AM stain), and red cells are dead cells (EthD-III stain). Scale bars: 400 µm.

Images showed cell alignment during this preliminary study, which was backed up by directionality quantification using *ImageJ*'s Fast Fourier Transform (FFT). Cell alignment was quantified using directionality analysis. Briefly, five images were obtained per condition per biological repeat after Live/Dead staining. Images were modified in Adobe Photoshop® using shake reduction to sharpen the images. Images were rotated until the micro-HF was at 180° across the screen. This ensured that the peak that occurred due to the micro-HF would be at 0° and therefore would not impact the results. Images were cropped to remove any white spaces on the edge of the image that were present after rotation. *ImageJ* was used to convert the images to 8bit and normalize the contrast (set to 0%) to account for different brightness settings of the images. Once all the images had been normalised, they were run through *ImageJ*'s 'Directionality' plugin using the Fast Fourier Transform (FFT) algorithm method (Fourier components methods, within the 'Directionality' plugin). FFTs are widely used for image analysis of polymer systems and have been shown to be valid for differentiating polymer structures and alignment (Zhu et al., 2018, Leila F. Deravi et al., 2017). Directional filters were used in the Fourier domain to process images composed of linear patterns, such as cell alignment along fibres as used in this research (Liu, 1991) . The plugin splits the image into pixels and calculates the Fourier power spectra of the pixel which generates the spatial frequencies of cells/fibres present between 0-180° (Leila F. Deravi et al., 2017). These values are analysed using polar coordinates and the power is measured for each angle using spatial filters (Zhu et al., 2018). These raw data can be extracted from the programme for comparative analysis. Micro-hollow fibre directionality was compared with a 2D control over the same time period. The results can be seen in Figure 28 for all cell types, where the frequency, effectively the normalised number of cells (ratio of total cells) that are oriented at a specific angle with respect to the micro-HF's axis, is shown. Cells that are completely in line with the

micro-HF's axis will produce a value of 0 degrees (°), whereas cells in any other orientation will appear at various values of angle in the x-axis. Frequencies were normalised to the highest value in order to be able to compare between cell types (Figures 28A-C), with the highest number of cells at a specific angle having a frequency of 1.

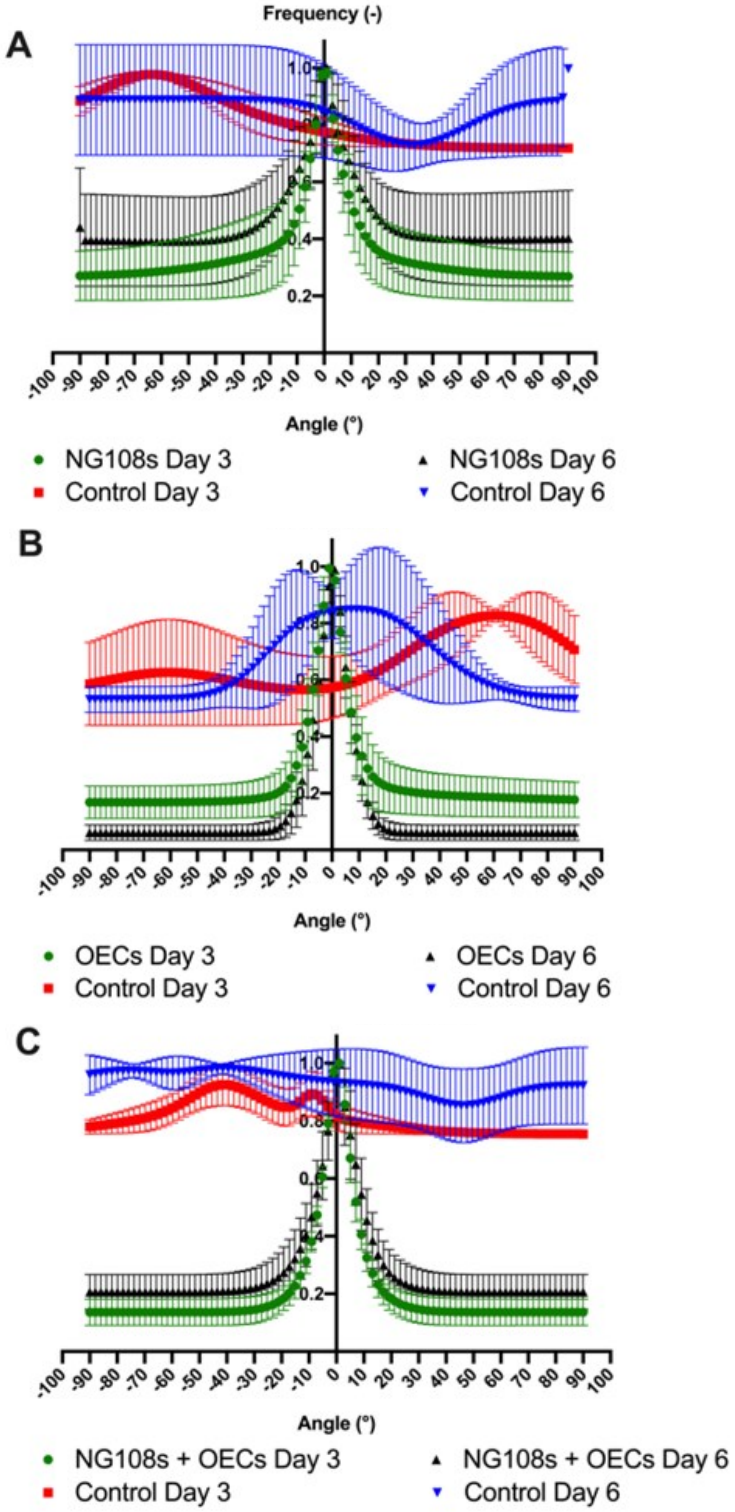

Figure 28: Quantification of cell directionality using the Fast Fourier Transform algorithm method, with cells grown on micro-HFs on day 3 (green), in planar culture on day 3 (control, red), on micro-HFs on day 6 (black) and in planar culture on day 6 (control, blue). (A) Directionality of NG108-15 cells. (B) Directionality of OECs. (C) Directionality of co-culture of NG108-15s and OECs. Data are normalized means to the largest frequency value ± SEM (N=3 independent biological repeats with 15 images analysed for each repeat).

The controls shown in all panels in Figure 28 represent cell growth on regular planar culture (T-flasks) at the same seeding densities (20,000 cells/cm^2) over the same culture time (6 days). It is evident that cell directionality in two-dimensional planar systems is random (red and blue in Figure 28A-C); all cells analysed were oriented at different angles, covering the whole spectrum of orientations. For all cell types grown on micro-HFs at both time points (day 3, green and day 6, black), there is a very remarkable peak of frequency around 0°, indicating that the majority of the cells are aligned with respect to the micro-HF's axis. To further demonstrate the effectiveness of the alignment achieved with these micro-HFs, the statistically significant differences were quantified between cells grown on planar culture versus those grown on micro-HFs at day 3 and day 6 by comparing the values of the angles corresponding to the highest frequency (without considering the angle's sign) – the absolute value of the peak. This is a measure of the most frequent angle of alignment, or in other words, the preferred angle at which cells orient themselves. An absolute value of the peak of 0° represents complete alignment. The results are shown in Figure 29.

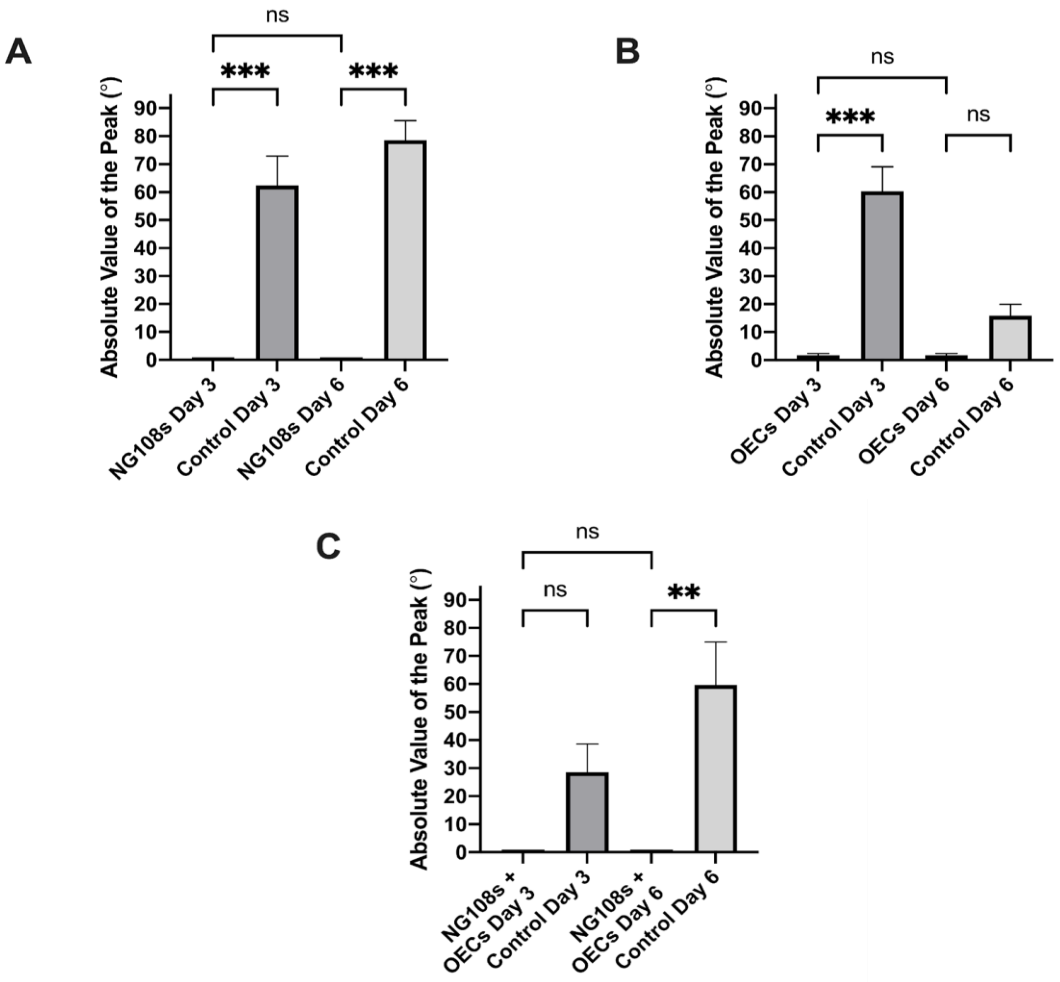

Figure 29: Absolute value of the orientation angle with respect to the micro-HF axis for the highest frequency directionality peak for (A) NG108-15 cells; (B) OECs; (C) Co-culture of NG108-15s and OECs; (D) C2C12 Myoblasts. Controls refer to cells grown on 2D. Data are means ± SEM (N=3 independent biological repeats with 15 images analysed for each repeat). ANOVA with multiple comparisons, 95 % confidence, was carried out on the data shown (P values: ***P < 0.001, **P = 0.001 to 0.01, *P = 0.01 to 0.05, ns = not significant, P ≥ 0.05).

Achieving attachment of the SH-SY5Y cells consistently required some optimisation of the growth conditions. Initially micro-hollow fibres and cells were placed in ultra-low attachment plates, which led to inconsistent attachment and formation of cell aggregates. The same experiment was performed but placing plates on a rocker

incubator, yielding similar results. Finally, cells were placed in an Eppendorf tube with micro-hollow fibres in the incubator over-night. These micro-hollow fibres were then transferred into square bacteriological plates for culture. Cell numbers were counted using DAPI and estimates of how many cells were attached were determined by doubling the number counted to account for the opposite side of the micro-HF, and averaging per cm of micro-hollow fibre. It was found that pORN/laminin was the best option for coating as shown in Figure 30, which is the same coating to be used for the iPSC-derived NPCs, as all other coatings had negligible cell attachment (Figure 30). Various amounts of cells were tested for initial seeding, but 2,000,000 cells/mL, although had the highest level of attachment, also had inconsistent cell attachment, with high numbers of cell clumps wherein cells attached to each other rather than the fibre itself. This led to 1,000,000 cells/mL to be used as it yielded a consistent single cell layer.

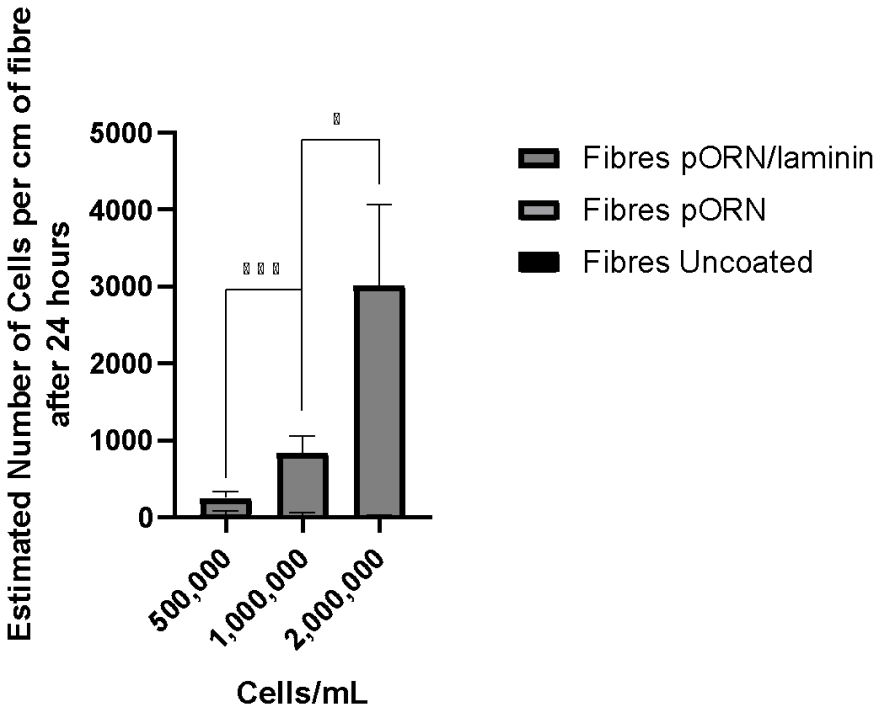

Figure 30: Number of cells attached to PX:PCL with different coatings and seeding densities. Cells were suspended in 1mL of media with the cell number required and 5 fibres were added. Fibres were stained with DAPI and the number of cells per cm of fibre was estimated. N=3 Anova with Tukey's multiple comparisons. Significance shown compares pORN/Laminin coatings to each other.

Once SH-SY5Y cells were known to be attached to the micro-hollow fibres, they were grown and differentiated on micro-HFs to determine neurite alignment. SH-SY5Y cells went through the same differentiation protocol as the one performed in planar culture (2D) to be able to compare them directly, and the directionality was tested in the same way as that for the NG108-15s and the OECs as explained previously in this Chapter.

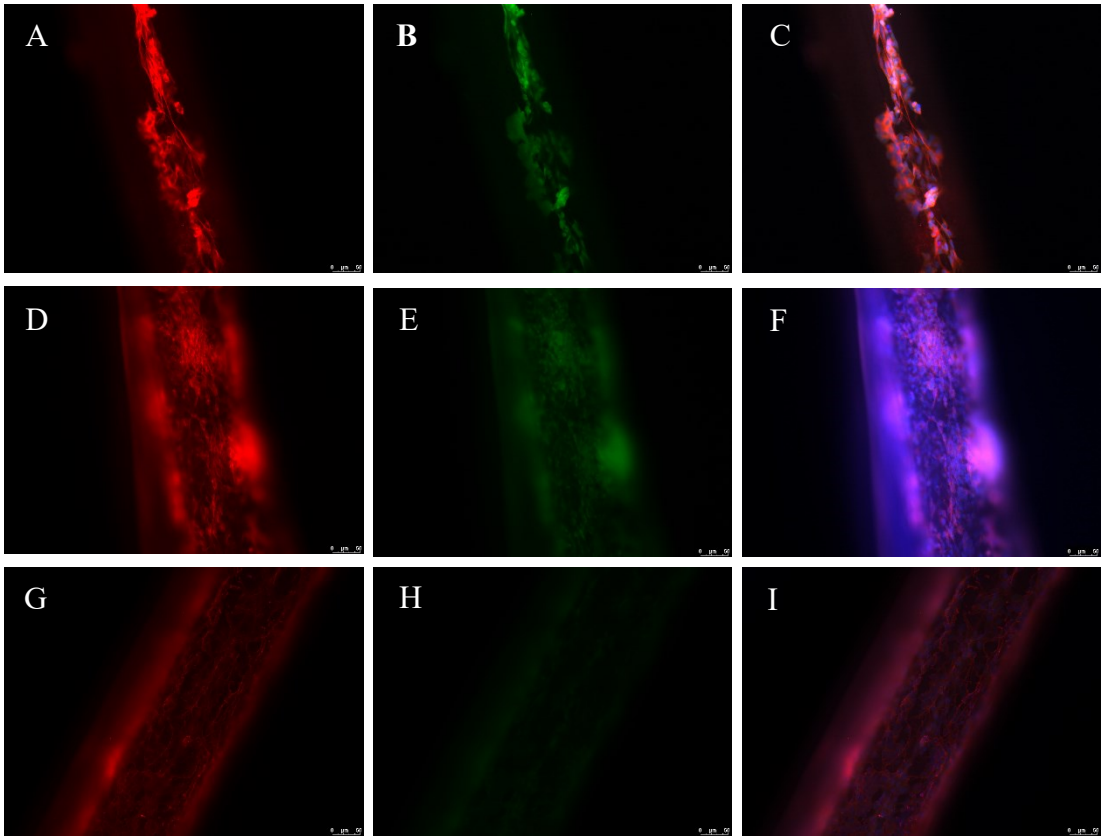

Figure 31: SH-SY5Y differentiation on PX:PCL micro-HFs. Cells were seeded at 1,000,000/mL in Eppendorf tubes. After 24 hours they were transferred to square bacteriological plates and into differentiation media. Representative images taken at D3 (A-C), D7 (E-F) and D12 (G-H). Stains shown are Tuj (A, D, G), CellTrackerTM Green ™ (B, E, H) and Merge with DAPI (C, F, I). Images taken on Leica Epifluorescent microscope with 50 µm scale bar.

Alignment of SH-SY5Y cells was seen through fluorescent microscopy (Figure 31), with cells genetically tagged with GFP and stained for Tuj (red) (Figure 31). These images show the neurite extensions growing along the micro-HFs. This was further quantified through *ImageJ* directionality analysis, using the Fast Fourier Transform

(FFT) algorithm. The 2D control was seen to have no alignment (Figure 32), with no distinct peaks seen anywhere (Figure 32A). This was then plotted as the absolute value of the peak (Figure 32B) in order to directly compare the directionality of the fibres over time and to the 2D controls. Both graphs show that the alignment of the cells increased over time as more neurites grew with further alignment along the fibres. When compared to the control there were significant differences at all time points. It should be noted that error bars for the 2D controls are larger as there is no distinct peak, the absolute value changes drastically from picture to picture.

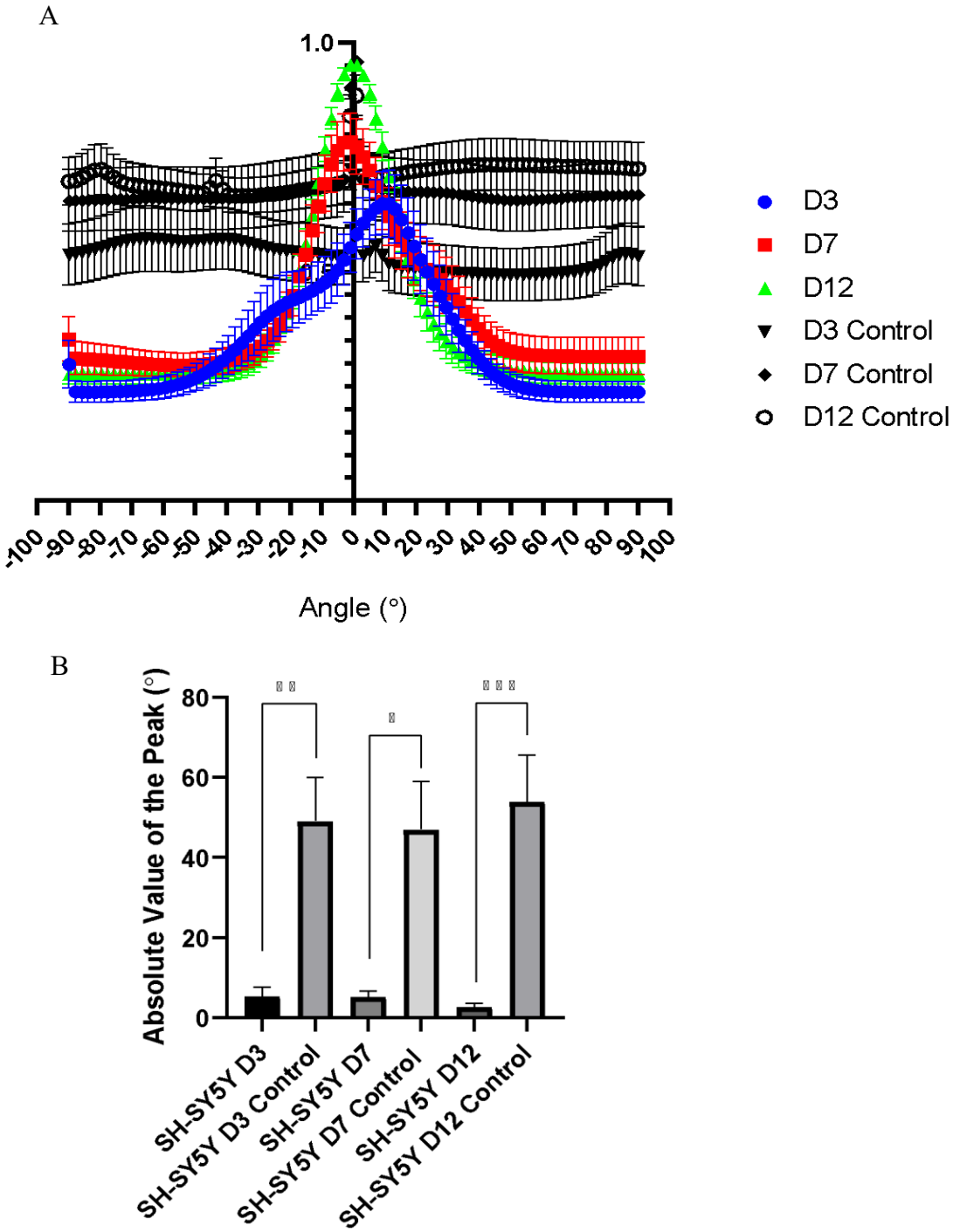

Figure 32: A, quantification of cell directionality using the Fast Fourier Transform algorithm method, with cells grown on micro-HFs on day 3 (blue), on micro-HFs on day 7 (red) and on micro-HFs on day 12 (green). 2D planar controls are shown (black). (A) Directionality of NG108-15 cells. Data are normalized means to the largest frequency value ± SEM (N=3 independent biological repeats with 15 images analysed for each repeat).

B, Absolute value of the orientation angle with respect to the micro-HF axis for the highest frequency directionality peak for all conditions. N=3 ±SEM, Anova with Tukey's multiple comparisons was performed.

The same experiments were repeated using NPCs that underwent neuronal differentiation on the micro-HFs, showing promising results, similar to what is seen for SH-SY5Ys, although it was only repeated once (N = 1) due to time constraints related to the COVID-19 pandemic. The NPCs were seeded on the PX:PCL micro-hollow fibres using the same protocol as described above. In 2D they were differentiated to excitatory neurons and their alignment was measured using the same parameters. Fluorescent microscopy (Figure 33) shows a slightly lower cell coverage; however, the same alignment is observed. Furthermore, neurite length looks to be increased at the early time points when compared with 2D NPC culture and even 2D differentiation.

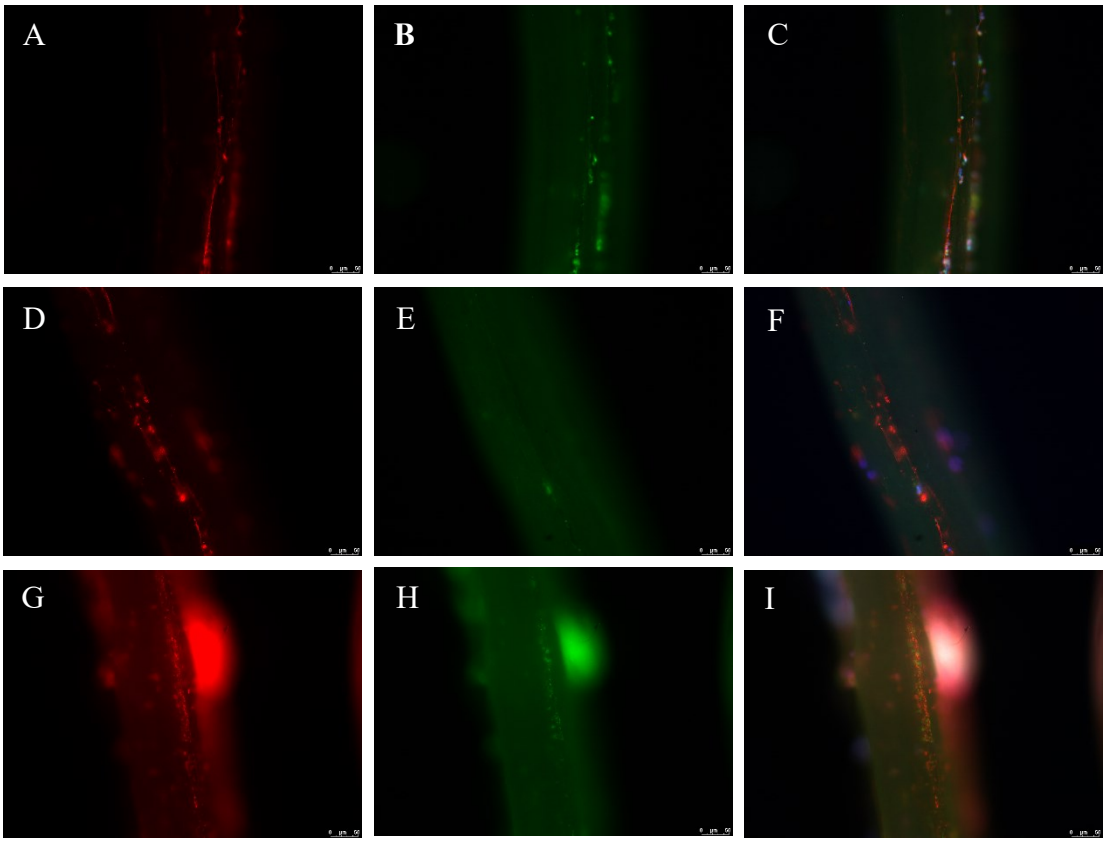

Figure 33: NPC neuronal differentiation on PX:PCL micro-HFs. Cells were seeded at 1,000,000/mL in Eppendorf tubes. After 24 hours they were transferred to square bacteriological plates and into neuronal differentiation media. Representative images taken at D3 (A-C), D7 (E-F) and D12 (G-H). stains shown are Tuj (A, D, G), CellTrackerTM Green TM (B, E, H) and Merge with DAPI (C, F, I). Images taken on Leica Epifluorescent microscope with 50 µm scale bar.

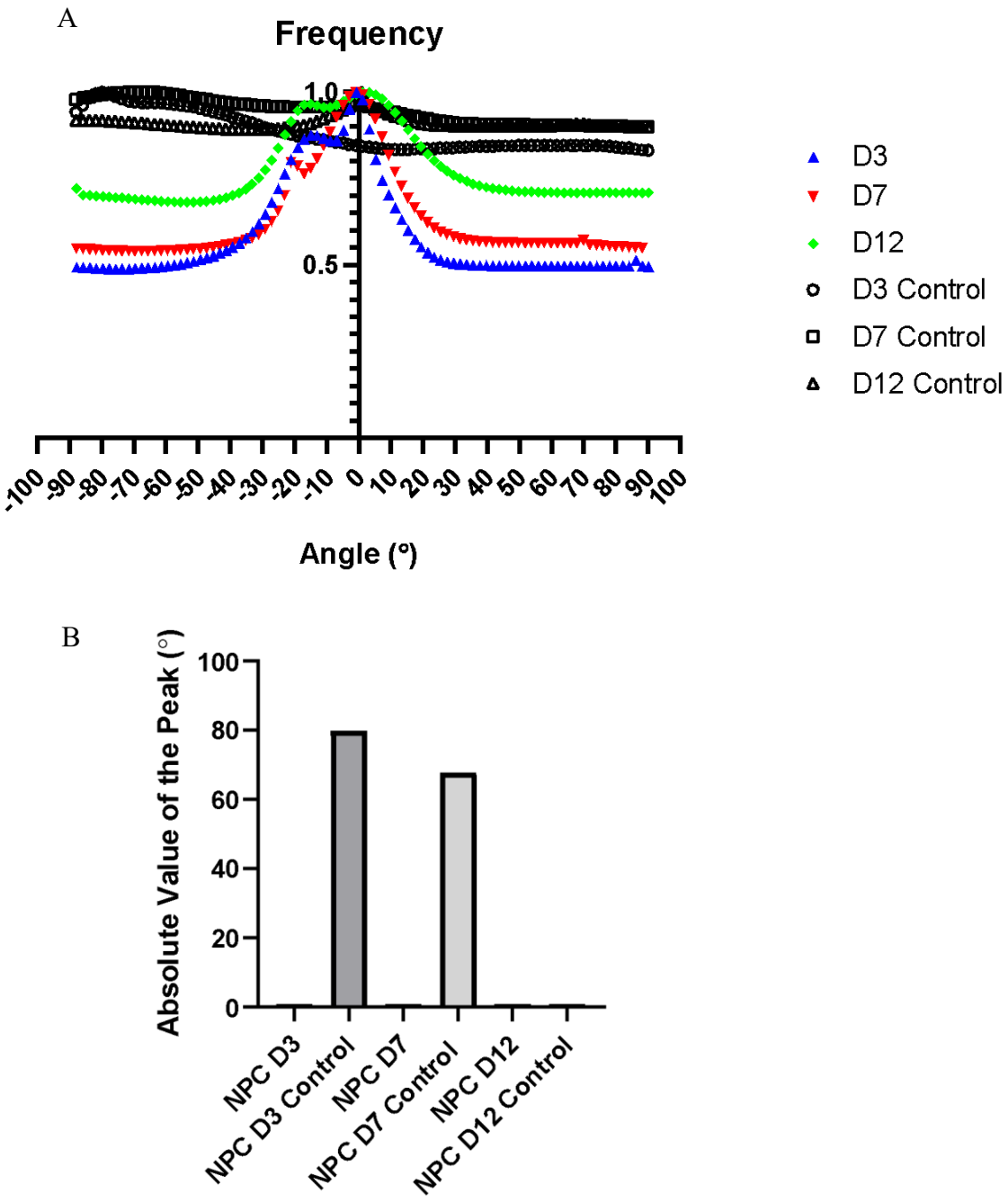

Figure 34: A, quantification of cell directionality using the Fast Fourier Transform algorithm method, with cells grown on micro-HFs on day 3 (blue), on micro-HFs on day 7 (red) and on micro-HFs on day 12 (green). 2D planar controls are shown (black). (A) Directionality of NG108-15 cells. Data are normalized means to the largest frequency value N=1. B, Absolute value of the orientation angle with respect to the micro-HF axis for the highest frequency directionality peak for all conditions. N=1.

The quantification of the results observed in Figure 34 showed a similar result to the alignment observed for NG108s, OECs and SH-SY5Y cells, with 2D controls showing no peaks (Figure 34A), which indicates a lack of alignment, and those cells grown and differentiated on the micro-hollow fibres being aligned in the same direction as the micro-HF's axis (Figure 34B). This suggest that the micro-hollow fibres' topography have the same alignment effect on the NPCs as they do on the SH-SY5Y cells.

The optimal concentration of gellan gum to prepare GG fluid gels found in Chapter 4, 0.3125% (w/w) GG fluid gel was added to 2D cultures and the micro-hollow fibres with both SHSY5Y cells and iPSC-derived neurons in order to see its effect on the cells. The SHSY5Ys experienced minimal changes, with some slight detachment as seen in Figure 35. The alignment of the cells was measured using the same parameters for the FFT algorithm as previously mentioned in this chapter. This found no significant change between the fibre alone and the addition of the gel as shown in the analysis performed in Figures 36 and 37. Furthermore, there appears to be little change to the directionality of the cells once the fluid gel was added into the culture system, with the peak even appearing to be steeper, the absolute values remain around the 0˚ point, even the control.

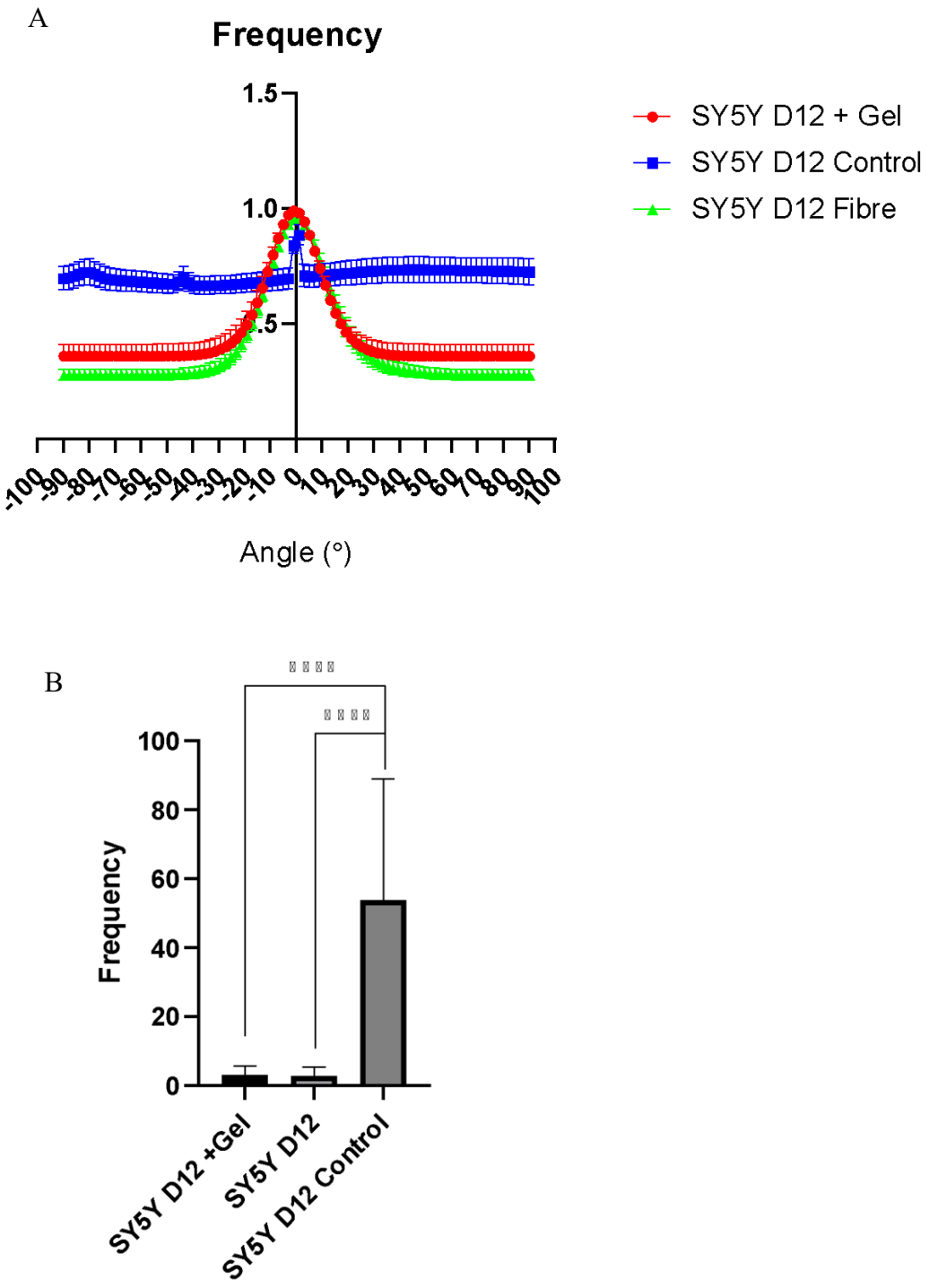

Figure 35: A, quantification of SH-SY5Y cell directionality using the Fast Fourier Transform algorithm method after 12 days of culture, with cells grown on micro-HFs (blue), on micro-HFs with 0.3125% GG fluid gel (red) and 2D control (green). Data are normalized means to the largest frequency value N=3; B, Absolute value of the orientation angle with respect to the micro-HF axis for the highest frequency directionality peak for all conditions. N=3.

A

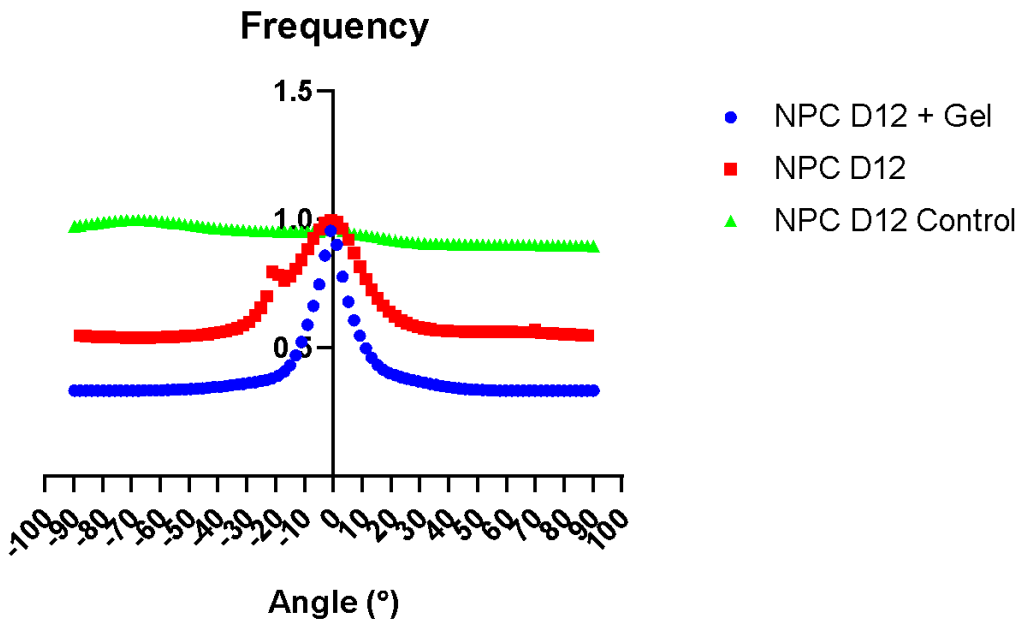

B

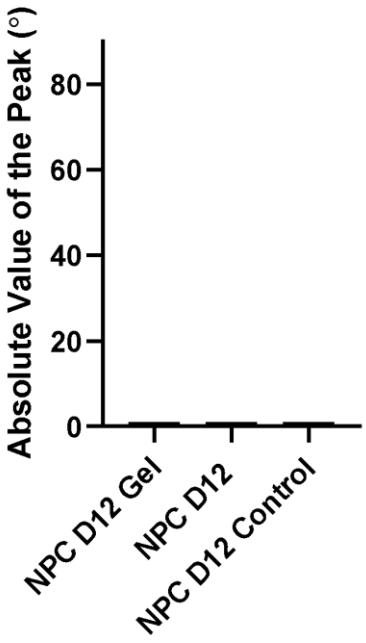

Figure 36: A, quantification of iPSC derived neuron directionality using the Fast Fourier Transform algorithm method after 12 days of culture, with cells grown on micro-HFs (red), on micro-HFs with 0.3125% GG fluid gel (blue) and 2D control (green). Data are normalized means to the largest frequency value N=1; B, Absolute value of the orientation angle with respect to the micro-HF axis for the highest frequency directionality peak for all conditions. N=1.

Finally, iPSC-derived neurons were cultured in 2D and the GG fluid gel (0.3125% (w/w)) was added to the culture 10 days after cell seeding, As seen in Figure 38, iPSC-derived neurons began to detach. However, although some cells detached from the surface, iPSC-derived neurons remained attached to each other, with 3D neurite connections remaining present.

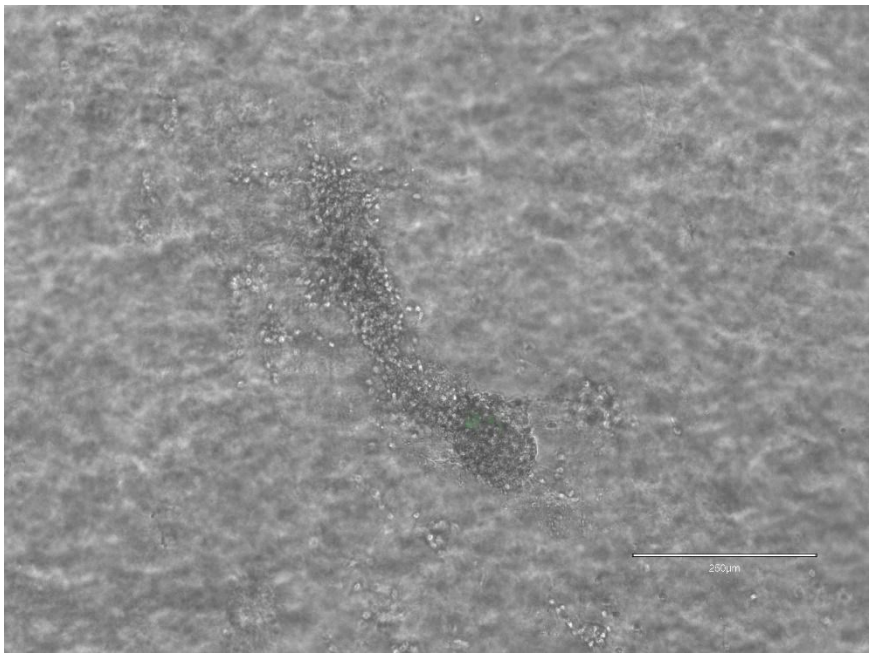

Figure 37: Phase contrast and CellTracker™ Green of D12 Neuronal differentiation 2 days after the addition of gel. Image is not focused on the surface of the plate showing that some colonies of neurons detached but their neurite connections to each other remained in-tact. Scale bar – 250 µm

6.2.2. Scratch wound assay

Scratch wounds were performed on the SH-S5Ys after differentiation with RA to determine their migration potential with and without the presence of the fluid gel. This experiment was performed in order to see whether GG fluid gels at healthy and damaged stiffnesses would affect wound healing potential and migration of SH-SY5Y cells.

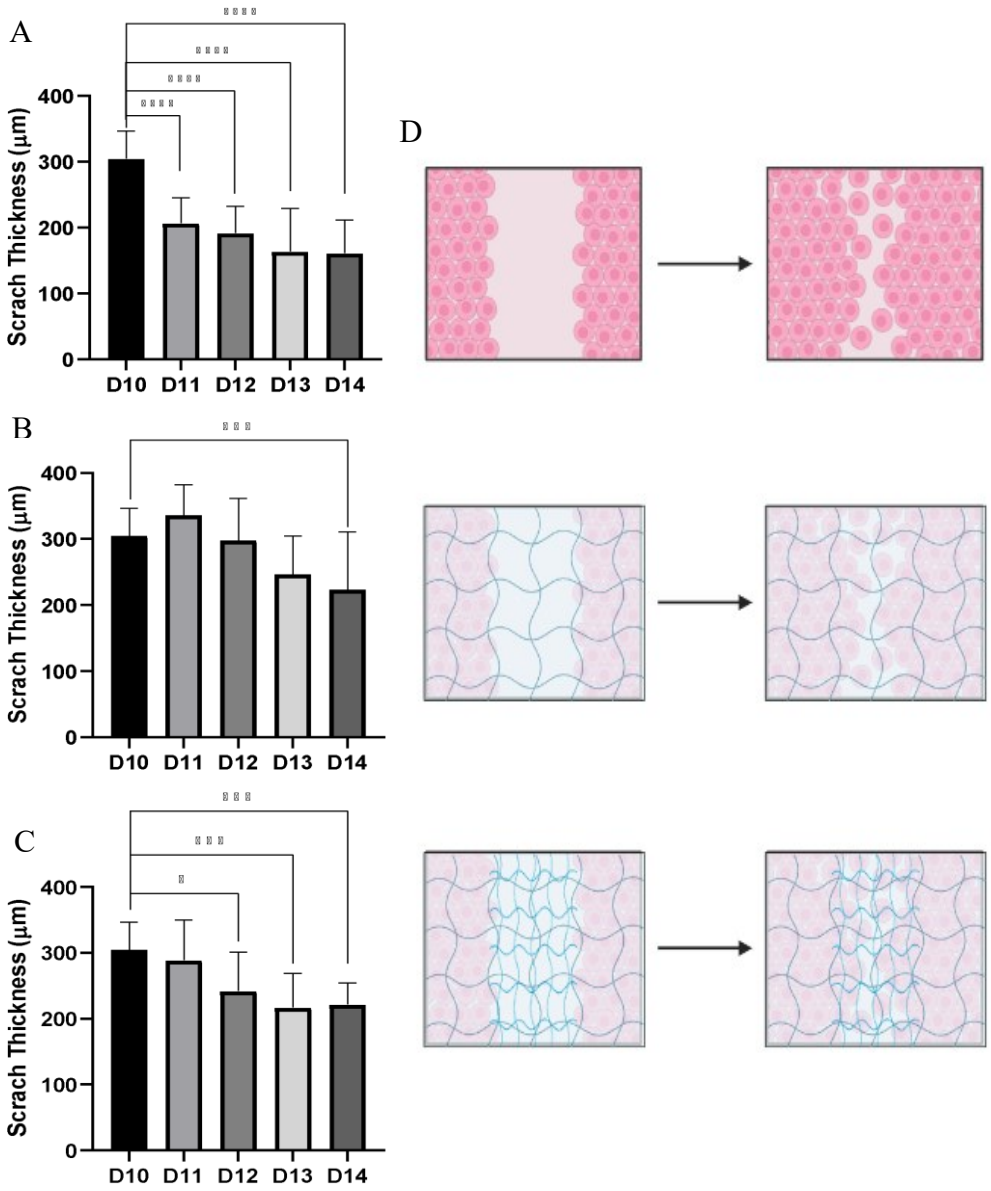

Without the fluid gel, over the 5-day time period (days 10 to 14 post- initial seeding), the cells had a steady closing rate, with the width of the "scratch" changing from 304 µm down to 161 µm. Most of this closure occurred within the first 24-hours, with almost 100 µm of closure developing within this time frame.

Figure 38: Scratch wound assay of differentiated SH-SY5Y cells., A, 2D control scratch assay, scratch was performed on D10 of differentiation. B, scratch was performed with 0.3125% GG fluid gel added on the cells to see effect on repair. C, scratch was performed with 0.3125% GG fluid gel added on the cells to see effect on repair, and 0.25% GG fluid gel was pipetted into the wound as the scratch was performed to mimic the mechanical differences in the spinal cord. Wound size was measured using ImageJ, N=3, Anova with multiple comparisons was performed. D, schematic showing the hydrogel and injected hydrogel on the scratch wound, image created using BioRender (biorender.com).

6.3. Discussion

In this Chapter the alignment of neural cells, facilitated via the use of micro-HFs as scaffolds, is assessed in conjunction with gellan gum fluid gels, which were fabricated as indicated in Chapter 4 to mimic the extracellular environment of the SC/SCI from a mechanical point of view.

6.3.1. NG108-15s and Olfactory Ensheathing Cells align along the micro-hollow fibres

Preliminary data for this thesis was carried out on NG108-15s and OECs. NG108-15s are a rat-mouse hybridoma line commonly used in current animal based SC research (Maeda et al., 2021, Otsuka et al., 2021) and furthermore in tissue engineering applications of SCI (Bedir et al., 2020, Lu et al., 2022). OECs were then chosen for their well-documented ability to regenerate CNS cells, with their primary function being in the olfactory system, but with regeneration being documented through transplantation in other areas of the CNS to guide axonal reconnection, particularly the SC (Raisman and Li, 2007).

Figure 27 shows that the NG108-15s and the OECS progressively aligned to the axis of the micro-HF in the culture period of 6 days. Moreover, they proliferate, as evidenced by the qualitatively higher number of cells that can be seen in all panels in Figure 27. Scarce dead cells (shown in red) can be seen in some instances, possibly due to attachment issues or lack of cell-cell interactions because of their spatial distribution. The number of dead cells observed is, nevertheless, very small, indicating high cytocompatibility and adhesion to the micro-HFs. In order to quantify the extent of this

alignment, image analysis and directionality calculations were performed, based on the Fast Fourier Transform algorithm. This method has previously been used to assess directionality in other fields (N.Molina et al., 2019). Five images per well, with three wells per biological repeat were analysed. The results can be seen for all cell types, where the frequency, effectively the number of cells that are oriented at a specific angle with respect to the micro-HF's axis Figure 28. These results show that the fibres appear to influence the directional growth of the cells, causing them to align along the fibres. Similar results were obtained for the other cell types in this work, with SH-SY5Y cells and iPSC-derived neurons having a marked increase in cellular alignment during their differentiation. Literature has shown that surface topographies are capable of inducing differentiation (Behnaz Sadat Eftekhari et al., 2020) through the activation of specific signalling cascades, which are determined by surface topographies (Czeisler et al., 2016). The images of both differentiation protocols may show the same effect with what looks like increased Tuj expression and neurite outgrowth. These mechanical cues can be utilised as a tool to enhance the efficiency and directionality of both differentiation and outgrowth. The alignment of the SH-SY5Y cells and iPSC-derived neurons provides a platform to differentiate these cells with a specific morphology in mind.

Some studies have attempted the alignment of neural cells on or encapsulated in electrospun fibres (Soliman et al., 2018, Quan et al., 2019, Lizarraga-Valderrama et al., 2019, Ranjan et al., 2020, Sun et al., 2019), in multi-channel architectures (Sun et al., 2019), and hydrogel tubes (Dumont et al., 2019, Muangsanit et al., 2021), but never on micro-porous hollow fibres with the advantages of the micro-scale, characteristic surface patterning without the need of specialised equipment, and porosity for mass transfer of oxygen and nutrients (Morelli et al., 2022, Tuin et al., 2014). We have achieved the same effect here, but in the micro-scale. Fibre alignment has been

previously attempted, focusing only on the physical distribution of several fibres with respect to each other. Here, it is hypothesised that the inherent parallel grooves on the surface of the micro-HF that result from the fabrication process, consequently, induce cell alignment and preferential orientation via contact guidance, eliminating the need for further surface patterning.

GG fluid gels were added to the micro-HF scaffolds to aim for a surrogate representation of the extracellular space in health and injured SC tissue.

The detaching of some cells was a disappointing outcome in the experiments shown in Figure 37. The use of GG fluid gels was never chosen for its cell interactions, rather the lack thereof. There is a plethora of more biologically relevant gelling agents which could be used to have a more physiological model. With gels being made from decellularised CNS ECM proteins (Medberry et al., 2013), functionalised hydrogels (Walczak et al., 2021) and many others. However, the cells detaching, yet remaining intact is an interesting result not yet described in the literature. This has possibilities of forming a functional 2D network and then having the ability to change its conformation without breaking the mature connections and transferring it to a new surface or 3D culture system.

The scratch assay shows that the gels do not significantly hinder regeneration, furthermore, there is a slight increase in repair when the softer gel is introduced. This could be due to the soft surface promoting the differentiation, maturation and migration of neuronal cells, allowing for them to be able to more readily migrate through the softer structures (Li et al., 2014).

Chapter 7

7. General Discussion and Conclusion

The main aim of this thesis was to develop a mechanically relevant *in vitro* model of the SC pre and post injury, with the hope to establish it as a high-throughput drug testing system in the future. The use of micro-HF to align neuronal cells in order to obtain a system which spatially resembles the SC is completely novel, and has the potential to be used to study all aspects of the spinal cord, from development to damage to regeneration. Additionally, this work aimed to include an artificial surrogate of the extracellular matrix seen in the SC that matches the mechanical properties of the *in vivo* tissue. We selected fluid gels, which are effectively dispersions of hydrogel microparticles, made of natural polymers. The reason for our interest in fluid gels is their unique rheological behaviour - they behave in a solid-like fashion at rest but are able to flow (their stiffness decreases) when they are subjected to stress or compression. This is exactly what happens in damaged tissue after a SCI and glial scar formation derived from compression or contusion. In this work, we have performed rheological analysis of our gellan gum fluid gels, and we have demonstrated that we can tune their mechanical properties by simply modifying the concentration of gellan gum and/or the concentration of salts involved in the gelation process.

There are vast considerations in the creation of an in vitro model of a tissue as complex as the spinal cord, and furthermore the glial scar that is generated after injury. Many of these considerations have been addressed here, including the micro-HF fabrication, fluid gel optimisation, seeding methods, cell type, differentiation and alignment.

Common techniques from the literature and the expertise within the lab group have been assessed in order to optimise the *in vitro* model described. This chapter will briefly summarise the experimental chapters and their findings, before providing an overall discussion of the results. Beyond this the final conclusions, limitations and the future directions within the field will be addressed in Chapter 8.

7.1. Summary of Experimental Findings

In Chapter 4, the main aim was to optimise biomaterial production and characterise their mechanical properties. The characterisation of the micro-HFs was undertaken via SEM and NMR, showing the specific striated surface topography, which is the cause of cellular alignment as evidence in Chapter 6. Different polymer dopes were tested, concluding that a 50:50 blend of PX:PCL was the best for this application due to the reproducibility of the fabrication process, the robustness of the micro-hollow fibre and the relative flexibility that allows for easy manipulation and handling. However, there is room for adaptations of this method to fit other gaps in the literature in the field of Tissue Engineering, not only focused on *in vitro* modelling of the CNS, since the micro-hollow fibres obtained in this work were porous and therefore allowed for liquid flow through their lumen and pores on their outer surface. Biodegradable polymers were tested, finding that they formed micro-hollow fibres; however, their topography was unstable. A plethora of polymers with different mechanical properties can be used for this application to fit a variety of experimental needs, and even hydrogel micro-fibres can be fabricated using this process.

GG fluid gels were optimised to be suitable for cell culture and mechanically relevant. The literature was analysed in order to find the mechanical properties of the SC that

we could mimic *in vitro*. It was found that between 50 and 500 Pa was the range for the injured to the healthy spinal cord. When GG fluid gels were made in PBS, 0.6% GG was sufficient to achieve these values of stiffness as demonstrated via rheology measurements. Nevertheless, due to the lack of calcium, the presence of these fluid gels in cell culture caused cell detachment. GG fluid gels were then made in DMEM/F12 salts, the same media that is used in the majority of the cell culture performed in this thesis, concluding that 0.3125% (w/w) and 0.25% (w/w0 GG to be the two fluid gels to be used to mimic the extracellular matrix in healthy and injured SC respectively. GG fluid gels were characterised via rheology in order to determine their stiffness (Young's Moduli) and through SEM imaging to observe their structure.

Chapter 5 was focused around the 2D cell culture and differentiation of multiple cell types. Here, the cells were assessed for differentiation markers from the point of pluripotency through to mature differentiation. It was found the SH-SY5Ys reliably differentiated and extended complex neurites in 2D. Motor neuron differentiation was attempted with little success, progenitor markers had little expression and expression of mature markers was very low. Cultures also seemed to over grow, with cells not exiting the cell cycle where they should, leading to excess cell death and detaching of the cultures because of overgrowth. Due to the length of time of this specific differentiation, and the adverse effect of the COVID-19 pandemic on available lab time and the lead times of some very niche cell culture supplies, motor neuron differentiation was abandoned. It was decided that excitatory neurons would be used, which are derived via a simpler differentiation process with prior expertise in the lab, due to their similar morphology and biological roles. These cells were able to be readily differentiated, producing neurons in 7 days, with no apparent glial contamination. As the GFP tagged ESC line for motor neuron differentiation was no longer used, it was

apparent that an alternative fluorescent tag was required. Viral transduction was avoided due to time constraints, and CellTracker™ Green was used, finding that it remained in the cells throughout the duration of the full experiment. These finding allowed for the progression to 3D culture onto the micro-HFs and with the GG fluid gels.

Following the optimisation of the cellular component and the biomaterial component individually, they were then brought together in the 3D culture experiments in Chapter 6. Chapter 6 determines how the different cell types behave when cultured in conjunction with the biomaterials, assessing the cell morphology and cell alignment on the micro-hollow fibres and in conjunction with the fluid gels. It was found that all four cell types used in this work (NG108-15s, OECs, SH-SY5Ys, NPCs) grow in line with the micro-hollow fibres, using their surface topography to align and proliferate. Their alignment became more evident over time, as more neurites were extended. This was compared with 2D controls, leading to a statistically significant increase in alignment. The GG fluid gels were then added to mimic the extracellular microenvironment from a mechanical point of view, which led to some detachment of cells, but in general had a minimal effect on the alignment of cell cultures as a whole, which was again quantified using the FFT algorithm. Finally, scratch wound assays were performed in order to evaluate the effect of the GG fluid gel on the cells' ability to migrate and resurface a "scratch". It was found to have a slight decrease in repair potential, and this appeared to be improved when a softer gel was added into the scratch itself.

7.2. General Discussion

SCI research is heavily focused on animal models which do not directly mimic the environment seen in humans. The use of *in vitro*, humanised models can help to bridge the gap between the animal models and the injuries we see in humans (Lucia Slovinska et al., 2015, Sharif-Alhoseini et al., 2017). The glial scar poses as a barrier to regeneration and repair as it changes the biological (Yuan and He, 2013) and mechanical properties (Moeendarbary et al., 2017) of the tissue. The cell culture system which has been describes here could, with increased complexity, mimic this *in vivo* scenario.

7.2.1. Biomaterials

The materials used here are low cost, biocompatible, with a high level of versatility and tunability (Coutinho et al., 2010). The project had a limited budget, meaning that many other options for materials could not be considered. As such, GG was chosen as the main component in the fluid gel formulations. Its sugar based structure is generally not sutiable for cell attachment, as there are no stable anchoring points that the cells are able to adhere to (Cameron J. Ferris et al., 2013). This leads to low levels of cell attachment and anoikis. The approach here used GG fluid gels as an external structure, not the growing surface. This spatial distribution will not produce the same effects as if they were bound to the soft structures; however, cells are mechanosensitive to all of their surroundings (Sun et al., 2022). GG provided a highly tuneable fluid gel, with properties allowing very specific mechanical parameters to be met. This thesis has highlighted the influence of GG concentration, salt concentration and cooling rates on the fabrication method as a means to tune the mechanical

properties (stiffness) of fluid gels. There are many more techniques which can be utilised in order to further tune the fluid gel, such as sheer force during cooling, mixing time and sonication (Moxon, 2016). These can all lead to a fluid gel with relevance across different tissues, different diffusion rates and many more outcomes.

The micro-HFs in this work aim to grow the cells in the same conformation as seen in the human spinal cord. The motor neurons of the SC are the longest cell type in the body. They are specifically orientated in order to be able to bridge the gap from the periphery to the brain (Stifani, 2014). Due to the specific surface topography that is seen in the micro-HFs which have been produced, it is possible to orientate the cells in the same conformation as is seen *in vivo*. The very organised structures which are seen in the body, not just the spinal cord, are often a limiting factor when it comes to *in vitro* modelling (Moroni et al., 2018). Utilising surface topographies is a well-established method for directing growth, differentiation and activity (Behnaz Sadat Eftekhari et al., 2020) of neurons in 2D (Kulangara et al., 2014, Repic et al., 2016, Behnaz Sadat Eftekhari et al., 2020). These micro-HFs were designed with this principle in mind. It was attempted to fabricate the micro-hollow fibres from biodegradable polymers, which would possibly allow for the formation of the 3D structure, with cells aligned along the fibres. The degradation of the fibre could then leave the cellular structure intact, having a 100% cell 3D structure. This, however, was not possible due to the fast degradation of the fibres fabricated with biodegradable polymers. As the surface topographies are in the nano scale, these were lost much quicker than the cells could attach and align, leaving a non-uniform structure without striations.

7.2.2. Cell Optimisation before the incorporation of biomaterials

A baseline in 2D needed to be determined in order to assess how the 3D cultures performed. It was here that the differentiations were carried out. It has been mentioned throughout that the aim was to use iPSC derived motor neurons within the model. This process takes several weeks to complete and involves very costly supplements, making media costs increase significantly. With this in mind and the impact of the COVID-19 pandemic, the differentiation into motor neurons was not possible. The protocol followed to begin with was similar to a some of the published literature (Xue et al., 2009, Shimojo et al., 2015, Faye et al., 2020). This protocol was chosen because of the detailed description of each step, alongside the fact that the differentiation procedure was performed in planar culture (2D). There were two main reasons for selecting a 2D differentiation protocol. Firstly, there was specific experience in the research group surrounding 2D differentiations which would aid in troubleshooting. This was not the case for 3D differentiation protocols. Secondly, since it was unclear at which point during differentiation cells would need to be transferred onto micro-hollow fibres, it was thought that a 2D protocol would ease the process, rather than attempting to attach embryoid bodies to the micro-HFs evenly, for example.

SH-SY5Y cells are a commonly used neural cell line which has the ability to be differentiated into neuron-like cells (Cheung YT et al., 2009). This was utilised as a fast and cheap alternative to the iPSC-derived neuronal cells in order to determine how the micro-hollow fibres affected their directionality during differentiation.

Excitatory neurons were chosen as a similar cell type which would best mimic the morphology that would be exhibited by motor neurons. This process utilised

Compound E in order to achieve a pure neuronal population without glial contamination (Li et al., 2011). This is a possible way to better induce motor neurons which was not tried during this study (Okubo et al., 2018). The excitatory neurons could be reproducibly generated in 2D, as seen through ICC. These cells could then be moved to the cell culture systems with biomaterials.

7.2.3. Bringing all the elements of the model together

Considering all the positive results obtained in Chapters 4 and 5, the early stage of the full model was now ready to be tested. Preliminary data with NG108-15s and OEC showed promising results, with alignment along the axis in the micro-hollow fibre. We were able to quantify this phenomenon for all cell types, which was an exciting and novel finding on this type of biomaterial. Furthermore, the alignment of the OECs means that there could be a possibility of using this model to test the effects of these cells as therapeutics (Kueh et al., 2012). Beyond this the SH-SY5Y cells and iPSC-derived excitatory neurons were tested on the micro-HFs, finding that they also aligned along them. This was a particularly thrilling result as the cells were therefore in the conformation desired for a SC model. Other research found in the literature has achieved similar results on 2D substrates through protein patterning, topography and chemical gradients (Chelli et al., 2014, Deumens et al., 2004, Adrien Casanova et al., 2018), but never on a 3-dimensional scaffold. Additionally, our newly fabricated micro-HF represent a cheap, easy and reproducible method to push cells towards an aligned phenotype on a tuneable 3D micro-HF structure.

The addition of GG fluid gels to the model had little effect on the cell directionality; however, it did cause some cell detaching. As GG is not biologically active it may have

an effect on the cell attachment. Furthermore, it was hypothesised that the detachment of cells in the PBS fluid gel was due to a lack of calcium. This may still be the case here, meaning that more calcium and possibly other salts may need to be added to the gel to reduce its effect on the cells. The GG fluid gel also had a minimal effect on the scratch assay. It showed that the wound closure slightly slowed, but the introduction of a softer gel that mimics the mechanical properties of the injured SC slightly improved wound closure. This is consistent with the literature, as neurons prefer softer substrates, the soft GG fluid gel may have caused this effect on the wound closure (Akcay and Luttge, 2021).

7.3. Conclusion

In this thesis, several topics have been addressed and brought together into a cohesive *in vitro* modelling system. Micro-HFs have been designed, fabricated and optimised, showing they have a desirable, stable surface topography which is capable of aligning cells along with, involving minimal numbers of cells wrapping around them. GG fluid gels fabrication has been optimised in order to produce a gel which is capable of mimicking the *in vivo* mechanical properties of both the healthy and the injured spinal cord. These have been assessed rheologically to show that they have similar mechanical properties which are desirable for this application. 2D cell culture has been optimised to efficiently and reliably differentiate SH-SY5Y cells and iPSC-derived excitatory neurons, these were assessed morphologically and through ICC.

These methods were then combined, utilising the optimised biomaterials and differentiation protocols to grow the SH-SY5Y cells and iPSC-derived excitatory neurons in a 3D culture environment on the micro-HFs surrounded by GG fluid gels. It

was shown that this induced cellular alignment similar to what is seen in the SC *in vivo* and in the presence of the mechanically relevant GG fluid gel.

Chapter 8

8. Future Work

Having established the micro-HFs and GG fluid gels technologies as tools to develop an appropriate 3-dimensional culture method with potential uses in drug testing for SCI, there are many further steps which could be addressed during ongoing and future work.

8.1. Motor Neurons

The inability to differentiate human PSCs into functional motor neurons is a flaw in this project. The further optimisation of the differentiation method would be the initial step to improve the model by using iPSC-derived motor neurons instead of the excitatory neurons that were included in this work. There are a lot of different methods available throughout the literature, each with varying degrees of success with the cell lines available. This would be a trial-and-error process in order to see how well each method worked.

8.2. Measures of Differentiation

Further analysis of the differentiation would be a great addition to the data set presented here. Utilising RNA sequencing would allow for a detailed overview of how far and efficiently the cells have differentiated. This would allow a more in-depth exploration of the effects of cellular alignment along micro-hollow fibres on cell differentiation. Beyond this, 3D imaging of the cells cultured on micro-hollow fibres,

which was attempted with poor results, could be utilised in order to track neurite numbers and their length along the micro-hollow fibres, comparing them with those observed in 2D planar culture. Furthermore, SEM imaging of the cells on the micro-hollow fibres could be used in order to determine how the cells are interacting with the surface topography.

Additionally, functional investigation of the cells behaviour on the micro-hollow fibres would aid to determine the differentiation yield, and if cells are functional in the ways that motor neurons should be, not only in 2D, but if they more closely resemble their *in vivo* behaviour. This could be done initially through calcium imaging and patch clamping.

8.3. Electrical signalling and recording

The functional assessments could be improved through multi-electrode arrays (MEA), which are able to electrically detect the action potentials of cells in culture. Work is being done at the moment to create 3D arrays that are capable of assessing the electrical activity of organoids (3Brain, 2022, Shin et al., 2021, Lam et al., 2021). It is highly possible that these micro-HFs could be adapted to be made from an electrically conductive material, such as graphene. Furthermore, the hollow space in their lumen could be used as a port for wiring, allowing for the fibre itself to be used as a multielectrode array. There is similar work being done with graphene, and its ability to assist regeneration in SCI (Dominguez-Bajo et al., 2020, Dominguez-Bajo et al., 2017).

8.4. Micro-fluidic chamber to induce damage

Work is currently being conducted within the research group, utilising microfluidic devices to hold the micro-HFs in place for cellular migration studies. These could be used here, as holding the micro-hollow fibre in place was one of the big issues with the way data was able to be collected and analysed. If micro-HFs were able to remain in place, damage could be caused to the fibre itself, and the cells attached in order to simulate an injury effectively and reproducibly *in vitro.* This could then be assessed to determine how the cells react to the damage and the repair and regeneration methods. This would also have a small footprint with the ability to upscale drastically for drug testing ang cell therapy testing.

8.5. Increasing the variety of cell types in the model

Last but not least, increasing the complexity of the model through the introduction of more cell types. There are a lot more cell types present in the spinal cord, and the glial scar in particular (Yuan and He, 2013). Here the focus was on the neuronal cells, which are responsible for the electrical activity and the data transfer. Beyond this however, there are astrocytes, microglia, and oligodendrocytes to name a few. The addition of these to the system would increase the complexity and the similarity to the biological environment which is being mimicked. This could be expanded on with bioprinting of specific cell types into specific regions of the model.

This thesis opens up a myriad of avenues which can be further explored in terms of a more detailed understanding of the cellular and mechanical changes that occur in trauma of the spinal cord.

Chapter 9

9. References

3BRAIN. 2022. *Accura-3D* [Online]. Available: https://www.3brain.com/technology/accura-3d [Accessed].

ADRIEN CASANOVA, MARIE-CHARLINE BLATCHE, CÉCILE A. FERRE, HÉLÈNE MARTIN, DANIEL GONZALEZ-DUNIA, LIVIU NICU & LARRIEU, G. 2018. Self-Aligned Functionalization Approach to Order Neuronal Networks at the Single-Cell Level. *Langmuir,* 34**,** 6612-6620.

AHMED, E. M. 2015. Hydrogel: Preparation, characterization, and applications: A review. *Journal of Advanced Research,* 6**,** 105-121.

AHMED, E. M., AGGOR, F. S., AWAD, A. M. & EL-AREF, A. T. 2013. An innovative method for preparation of nanometal hydroxide superabsorbent hydrogel. *Carbohydr Polym,* 91**,** 693-8.

AKCAY, G. & LUTTGE, R. 2021. Stiff-to-Soft Transition from Glass to 3D Hydrogel Substrates in Neuronal Cell Culture. *Micromachines (Basel),* 12.

ALASTAIR I. GRAINGER, MARIANNE C. KING, DAVID A. NAGEL, H. RHEINALLT PARRI, COLEMAN, M. D. & HILL*, E. J. 2018. In vitro Models for Seizure-Liability Testing Using Induced Pluripotent Stem Cells. *Frontiers Neuroscience*.

ALEXANDRA E JOHNS & MARAGAKIS, N. J. 2022. Exploring Motor Neuron Diseases Using iPSC Platforms. *Stem Cells,* 40**,** 2-13.

ALIZADEH, A., DYCK, S. M. & KARIMI-ABDOLREZAEE, S. 2019. Traumatic Spinal Cord Injury: An Overview of Pathophysiology, Models and Acute Injury Mechanisms. *Front Neurol,* 10**,** 282.

ALLEN, A. R. 1911. Surgery of experimental lesion of spinal cord equivalent to crush injury of fracture dislocation of spinal column. *Journal of American Medical Association*

ALLEN, A. R. 1914. Remarks on the histopathological changes in the spinal cord due to impact. An experimental study. *The Journal of Nervous and Mental Disease*.

ALLENBY, M. C., TAHLAWI, A., MORAIS, J. C. F., LI, K., PANOSKALTSIS, N. & MANTALARIS, A. 2018. Ceramic Hollow Fibre Constructs for Continuous Perfusion and Cell Harvest from 3D Hematopoietic Organoids. *Stem Cells Int,* 2018**,** 6230214.

ALMAD, A., SAHINKAYA, F. R. & MCTIGUE, D. M. 2011. Oligodendrocyte fate after spinal cord injury. *Neurotherapeutics,* 8**,** 262-73.

AMSDEN, B. 1998. Solute diffusion within hydrogels. Mechanisms and models. *Macromolecules,* 31**,** 8382-8395.

ASSINCK, P., DUNCAN, G. J., HILTON, B. J., PLEMEL, J. R. & TETZLAFF, W. 2017. Cell transplantation therapy for spinal cord injury. *Nat Neurosci,* 20**,** 637-647.

ATCC. 2022. *SH-SY5Y* [Online]. Available: https://www.atcc.org/products/crl-2266 [Accessed].

BAHAREH AZIMI, PARVIZ NOURPANAH, MOHAMMAD RABIEE, MOHAMMAD RABIEE & ARBAB, S. 2014. Poly (ϵ-caprolactone) Fiber: An Overview *Journal of Engineered Fibers and Fabrics*.

BARRIGA, E. H., FRANZE, K., CHARRAS, G. & MAYOR, R. 2018. Tissue stiffening coordinates morphogenesis by triggering collective cell migration in vivo. *Nature,* 554**,** 523-527.

BAUMANN, N. & PHAM-DINH, D. 2002. *Encyclopaedia of the human brain – Astrocytes,* San Diego, California, USA, Academic Press.

BEDIR, T., ULAG, S., USTUNDAG, C. B. & GUNDUZ, O. 2020. 3D bioprinting applications in neural tissue engineering for spinal cord injury repair. *Mater Sci Eng C Mater Biol Appl,* 110**,** 110741.

BEHNAZ SADAT EFTEKHARI, MAHNAZ ESKANDARI, PAUL A. JANMEY, ALI SAMADIKUCHAKSARAEI & GHOLIPOURMALEKABADI, M. 2020. Surface Topography and Electrical Signaling: Single and Synergistic Effects on Neural Differentiation of Stem Cells. *Advanced Functional Materials,* 30
BETTINGER, C. J., LANGER, R. & BORENSTEIN, J. T. 2009. Engineering substrate topography at the Micro- and nanoscale to control cell function. *Angew Chem Int Ed Engl,* 48**,** 5406-5415.
BHARATHAN, S. P., MANIAN, K. V., AALAM, S. M., PALANI, D., DESHPANDE, P. A., PRATHEESH, M. D., SRIVASTAVA, A. & VELAYUDHAN, S. R. 2017. Systematic evaluation of markers used for the identification of human induced pluripotent stem cells. *Biol Open,* 6**,** 100-108.
BICAN, O., MINAGAR, A. & PRUITT, A. A. 2013a. The Spinal Cord A Review of Functional Neuroanatomy. *Neurologic Clinics,* 31**,** 1-+.
BICAN, O., MINAGAR, A. & PRUITT, A. A. 2013b. The spinal cord: a review of functional neuroanatomy. *Neurol Clin,* 31**,** 1-18.
BOIDO, M., RUPA, R., GARBOSSA, D., FONTANELLA, M., DUCATI, A. & VERCELLI, A. 2009. Embryonic and adult stem cells promote raphespinal axon outgrowth and improve functional outcome following spinal hemisection in mice. *Eur J Neurosci,* 30**,** 833-46.
BONNIER, F., KEATING, M. E., WROBEL, T. P., MAJZNER, K., BARANSKA, M., GARCIA-MUNOZ, A., BLANCO, A. & BYRNE, H. J. 2015. Cell viability assessment using the Alamar blue assay: a comparison of 2D and 3D cell culture models. *Toxicol In Vitro,* 29**,** 124-31.
BOOM, R. M., BOOMGAARD, T. V. D. & SMOLDERS, C. A. 1994. Mass transfer and thermodynamics during immersion precipitation for a two-polymer system: Evaluation with the system PES—PVP—NMP—water. *Jounral of Membrane Science* 90**,** 231-249.
BOULET, T., KELSO, M. L. & OTHMAN, S. F. 2011. Microscopic magnetic resonance elastography of traumatic brain injury model. *J Neurosci Methods,* 201**,** 296-306.
BOVEY, F. A., HOOD, F. P., ANDERSON, E. W. & SNYDER, L. C. 1965. Polymer NMR Spectroscopy. XI. Polystyrene and Polystyrene Model Compounds. *J. Chem. Phys,* 42.
BRADBURY, E. J., MOON, L. D., POPAT, R. J., KING, V. R., BENNETT, G. S., PATEL, P. N., FAWCETT, J. W. & MCMAHON, S. B. 2002. Chondroitinase ABC promotes functional recovery after spinal cord injury. *Nature,* 416**,** 636-40.
BRINKMANN, B. G., AGARWAL, A., SEREDA, M. W., GARRATT, A. N., MULLER, T., WENDE, H., STASSART, R. M., NAWAZ, S., HUMML, C., VELANAC, V., RADYUSHKIN, K., GOEBBELS, S., FISCHER, T. M., FRANKLIN, R. J., LAI, C., EHRENREICH, H., BIRCHMEIER, C., SCHWAB, M. H. & NAVE, K. A. 2008. Neuregulin-1/ErbB signaling serves distinct functions in myelination of the peripheral and central nervous system. *Neuron,* 59**,** 581-95.
BUDDAY, S., SOMMER, G., HAYBAECK, J., STEINMANN, P., HOLZAPFEL, G. A. & KUHL, E. 2017a. Rheological characterization of human brain tissue. *Acta Biomater,* 60**,** 315-329.
BUDDAY, S., SOMMER, G., HOLZAPFEL, G. A., STEINMANN, P. & KUHL, E. 2017b. Viscoelastic parameter identification of human brain tissue. *J Mech Behav Biomed Mater,* 74**,** 463-476.
BUSCH, S. A. & SILVER, J. 2007. The role of extracellular matrix in CNS regeneration. *Curr Opin Neurobiol,* 17**,** 120-7.
CAMERON J. FERRIS, KERRY J. GILMORE, WALLACE, G. G. & PANHUIS, M. I. H. 2013. Modified gellan gum hydrogels for tissue engineering applications. *Soft Matter,* 9**,** 3705-3711.
CARBONE, L. 2011. Pain in laboratory animals: the ethical and regulatory imperatives. *PLoS One,* 6**,** e21578.
CARGILL, R. S., 3RD, DEE, K. C. & MALCOLM, S. 1999. An assessment of the strength of NG108-15 cell adhesion to chemically modified surfaces. *Biomaterials,* 20**,** 2417-25.
CAZZOLA, D., HOLSGROVE, T. P., PREATONI, E., GILL, H. S. & TREWARTHA, G. 2017. Cervical Spine Injuries: A Whole-Body Musculoskeletal Model for the Analysis of Spinal Loading. *PLoS One,* 12**,** e0169329.
CHAMBERS, S. M., FASANO, C. A., PAPAPETROU, E. P., TOMISHIMA, M., SADELAIN, M. & STUDER, L. 2009. Highly efficient neural conversion of human ES and iPS cells by dual inhibition of SMAD signaling. *Nat Biotechnol,* 27**,** 275-80.

CHANDRASEKARAN, A., AVCI, H. X., OCHALEK, A., ROSINGH, L. N., MOLNAR, K., LASZLO, L., BELLAK, T., TEGLASI, A., PESTI, K., MIKE, A., PHANTHONG, P., BIRO, O., HALL, V., KITIYANANT, N., KRAUSE, K. H., KOBOLAK, J. & DINNYES, A. 2017. Comparison of 2D and 3D neural induction methods for the generation of neural progenitor cells from human induced pluripotent stem cells. *Stem Cell Res,* 25**,** 139-151.
CHELLI, B., BARBALINARDO, M., VALLE, F., GRECO, P., BYSTRENOVA, E., BIANCHI, M. & BISCARINI, F. 2014. Neural cell alignment by patterning gradients of the extracellular matrix protein laminin. *Interface Focus,* 4**,** 20130041.
CHEN, D. T. N., WEN, Q., JANMEY, P. A., CROCKER, J. C. & YODH, A. G. 2010. Rheology of Soft Materials *Annual Review of Condensed Matter Physics* 1**,** 301-322.
CHEN, Y., HU, X., HU, X., ZHANG, S. & ZHANG, Y. 2015. Polymeric hollow fiber membranes prepared by dual pore formation mechanism. *Material Letters* 143**,** 315-318.
CHEUNG YT, LAU WK, YU MS, LAI CS, YEUNG SC, SO KF & RC., C. 2009. Effects of all-trans-retinoic acid on human SH-SY5Y neuroblastoma as in vitro model in neurotoxicity research. *Neurotoxicology,* 30**,** 127-135.
CHOUHAN, G., MOAKES, R. J. A., ESMAEILI, M., HILL, L. J., DECOGAN, F., HARDWICKE, J., RAUZ, S., LOGAN, A. & GROVER, L. M. 2019. A self-healing hydrogel eye drop for the sustained delivery of decorin to prevent corneal scarring. *Biomaterials,* 210**,** 41-50.
COFANO, F., BOIDO, M., MONTICELLI, M., ZENGA, F., DUCATI, A., VERCELLI, A. & GARBOSSA, D. 2019. Mesenchymal Stem Cells for Spinal Cord Injury: Current Options, Limitations, and Future of Cell Therapy. *Int J Mol Sci,* 20.
COHEN, D. M., PATEL, C. B., AHOBILA-VAJJULA, P., SUNDBERG, L. M., CHACKO, T., LIU, S. J. & NARAYANA, P. A. 2009. Blood-spinal cord barrier permeability in experimental spinal cord injury: dynamic contrast-enhanced MRI. *NMR Biomed,* 22**,** 332-41.
COMPAAN, A. M., SONG, K., HUANG, Y., COMPAAN, A. M., SONG, K. & HUANG, Y. 2019. Gellan Fluid Gel as a Versatile Support Bath Material for Fluid Extrusion Bioprinting. *ACS Applied Materials & Interfaces,* 11**,** 5714-5726.
COOPER, J. G., SICARD, D., SHARMA, S., GULDEN, S. V., MCGUIRE, T. L., CAJIAO, M. P., TSCHUMPERLIN, D. J. & KESSLER, J. A. 2020. Spinal Cord Injury Results in Chronic Mechanical Stiffening. *Journal of Neurotrauma,* 37**,** 494-506.
COUTINHO, D. F., SANT, S. V., SHIN, H., OLIVEIRA, J. T., GOMES, M. E., NEVES, N. M., KHADEMHOSSEINI, A. & REIS, R. L. 2010. Modified Gellan Gum hydrogels with tunable physical and mechanical properties. *Biomaterials,* 31**,** 7494-502.
CURT, A. & DIETZ, V. 2005. Controversial treatments for spinal-cord injuries. *Lancet,* 365**,** 841-841.
CZEISLER, C., SHORT, A., NELSON, T., GYGLI, P., ORTIZ, C., CATACUTAN, F. P., STOCKER, B., CRONIN, J., LANNUTTI, J., WINTER, J. & OTERO, J. J. 2016. Surface topography during neural stem cell differentiation regulates cell migration and cell morphology. *J Comp Neurol,* 524**,** 3485-3502.
DAVID E KOSER, AMELIA J THOMPSON, SARAH K FOSTER, ASHA DWIVEDY, EVA K PILLAI, GRAHAM K SHERIDAN, HANNO SVOBODA, MATHEUS VIANA, LUCIANO DA F COSTA, JOCHEN GUCK, HOLT, C. E. & FRANZE, K. 2016. Mechanosensing is critical for axon growth in the developing brain. *Nature Neuroscience,* 19**,** 1592-1598.
DE NAPOLI, I. E., SCAGLIONE, S., GIANNONI, P., QUARTO, R. & CATAPANO, G. 2011. Mesenchymal stem cell culture in convection-enhanced hollow fiber membrane bioreactors for bone tissue engineering. *Journal of Membrane Science* 379**,** 341-352.
DESHMANE, S. L., KREMLEV, S., AMINI, S. & SAWAYA, B. E. 2009. Monocyte chemoattractant protein-1 (MCP-1): an overview. *J Interferon Cytokine Res,* 29**,** 313-26.
DEUMENS, R., KOOPMANS, G. C., DEN BAKKER, C. G., MAQUET, V., BLACHER, S., HONIG, W. M., JEROME, R., PIRARD, J. P., STEINBUSCH, H. W. & JOOSTEN, E. A. 2004. Alignment of glial cells stimulates directional neurite growth of CNS neurons in vitro. *Neuroscience,* 125**,** 591-604.
DEVIVO, M. J., GO, B. K. & JACKSON, A. B. 2002. Overview of the national spinal cord injury statistical center database. *J Spinal Cord Med,* 25**,** 335-8.
DOBKIN, B. H., CURT, A. & GUEST, J. 2006. Cellular transplants in China: Observational study from the largest human experiment in chronic spinal cord injury. *Neurorehabilitation and Neural Repair,* 20**,** 5-13.

DOMINGUEZ-BAJO, A., GONZALEZ-MAYORGA, A., LOPEZ-DOLADO, E., MUNUERA, C., GARCIA-HERNANDEZ, M. & SERRANO, M. C. 2020. Graphene Oxide Microfibers Promote Regenerative Responses after Chronic Implantation in the Cervical Injured Spinal Cord. *ACS Biomater Sci Eng,* 6**,** 2401-2414.
DOMINGUEZ-BAJO, A., GONZALEZ-MAYORGA, A., LOPEZ-DOLADO, E. & SERRANO, M. C. 2017. Graphene-Derived Materials Interfacing the Spinal Cord: Outstanding in Vitro and in Vivo Findings. *Front Syst Neurosci,* 11**,** 71.
DUMONT, C. M., CARLSON, M. A., MUNSELL, M. K., CICIRIELLO, A. J., STRNADOVA, K., PARK, J., CUMMINGS, B. J., ANDERSON, A. J. & SHEA, L. D. 2019. Aligned hydrogel tubes guide regeneration following spinal cord injury. *Acta Biomater,* 86**,** 312-322.
DUMONT, R. J., OKONKWO, D. O., VERMA, S., HURLBERT, R. J., BOULOS, P. T., ELLEGALA, D. B. & DUMONT, A. S. 2001. Acute spinal cord injury, part I: pathophysiologic mechanisms. *Clin Neuropharmacol,* 24**,** 254-64.
EBERLE, D. F., G. KURTH, T. JAGIELSKA, A. MÖLLMERT, S. ULBRICHT, E. WAGNER, K. TAUBENBERGER, A.V. TRÄBER, N. ESCOLANO, J. VLIET, K.J.V. AND GUCK, J 2020. Acquired demyelination but not genetic developmental defects in myelination leads to brain tissue stiffness changes. *Brain Multiphysics,* 1.
ECHEVERRY, S., SHI, X. Q., RIVEST, S. & ZHANG, J. 2011. Peripheral nerve injury alters blood-spinal cord barrier functional and molecular integrity through a selective inflammatory pathway. *J Neurosci,* 31**,** 10819-28.
EGHBALI, H., NAVA, M. M., MOHEBBI-KALHORI, D. & RAIMONDI, M. T. 2016. Hollow fiber bioreactor technology for tissue engineering applications. *Int J Artif Organs,* 39**,** 1-15.
EL FRAY, M., PROWANS, P., PUSKAS, J. E. & ALTSTADT, V. 2006. Biocompatibility and fatigue properties of polystyrene-polyisobutylene-polystyrene, an emerging thermoplastic elastomeric biomaterial. *Biomacromolecules,* 7**,** 844-50.
ELLIOTT DONAGHUE, I., TAM, R., SEFTON, M. V. & SHOICHET, M. S. 2014. Cell and biomolecule delivery for tissue repair and regeneration in the central nervous system. *J Control Release,* 190**,** 219-27.
ENGLER, A. J., GRIFFIN, M. A., SEN, S., BONNEMANN, C. G., SWEENEY, H. L. & DISCHER, D. E. 2004. Myotubes differentiate optimally on substrates with tissue-like stiffness: pathological implications for soft or stiff microenvironments. *J Cell Biol,* 166**,** 877-87.
ESPOSITO, E. & CUZZOCREA, S. 2011. Anti-TNF therapy in the injured spinal cord. *Trends Pharmacol Sci,* 32**,** 107-15.
FAN, Y. W., CUI, F. Z., HOU, S. P., XU, Q. Y., CHEN, L. N. & LEE, I. S. 2002. Culture of neural cells on silicon wafers with nano-scale surface topograph. *J Neurosci Methods,* 120**,** 17-23.
FANG, A., HAO, Z., WANG, L., LI, D., HE, J., GAO, L., MAO, X. & PAZ, R. 2019. In vitro model of the glial scar. *Int J Bioprint,* 5**,** 235.
FASHANDI, H., ZARRINI, K., YOUSSEFI, M. & ABOLHASANI, M. M. 2015. . Synergistic Contribution of Spinneret Diameter and Physical Gelation To Develop Macrovoid-Free Hollow Fiber Membranes Using Single Orifice Spinneret. *Industrial & Engineering Chemistry Research,* 54**,** 7728-7736.
FAYE, P. A., VEDRENNE, N., MIRESSI, F., RASSAT, M., ROMANENKO, S., RICHARD, L., BOURTHOUMIEU, S., FUNALOT, B., STURTZ, F., FAVREAU, F. & LIA, A. S. 2020. Optimized Protocol to Generate Spinal Motor Neuron Cells from Induced Pluripotent Stem Cells from Charcot Marie Tooth Patients. *Brain Sci,* 10.
FELES, S., OVERATH, C., REICHARDT, S., DIEGELER, S., SCHMITZ, C., KRONENBERG, J., BAUMSTARK-KHAN, C., HEMMERSBACH, R., HELLWEG, C. E. & LIEMERSDORF, C. 2022. Streamlining Culture Conditions for the Neuroblastoma Cell Line SH-SY5Y: A Prerequisite for Functional Studies. *Methods Protoc,* 5.
FITCH, M. T. & SILVER, J. 2008. CNS injury, glial scars, and inflammation: Inhibitory extracellular matrices and regeneration failure. *Exp Neurol,* 209**,** 294-301.
FRANCO WOOLFE, STEPHEN G. WAXMAN & HAINS, B. C. 2007. In Silico Modeling of Axonal Reconnection within A Discrete Fiber Tract after Spinal Cord Injury. *Journal of Neurotrauma,* 24**,** 421-432.
FROSTELL, A., HAKIM, R., THELIN, E. P., MATTSSON, P. & SVENSSON, M. 2016. A Review of the Segmental Diameter of the Healthy Human Spinal Cord. *Frontiers in Neurology,* 7.

FU, H., HU, D., ZHANG, L., SHEN, X. & TANG, P. 2018. Efficacy of Oligodendrocyte Progenitor Cell Transplantation in Rat Models with Traumatic Thoracic Spinal Cord Injury: A Systematic Review and Meta-Analysis. *J Neurotrauma,* 35**,** 2507-2518.
FUHRMANN, T., ANANDAKUMARAN, P. N. & SHOICHET, M. S. 2017. Combinatorial Therapies After Spinal Cord Injury: How Can Biomaterials Help? *Adv Healthc Mater,* 6.
GARREC, D. A. & NORTON, I. T. 2012. Understanding fluid gel formation and properties. *Journal of Food Engineering,* 112**,** 175-182.
GAUDET, A. D. & FONKEN, L. K. 2018. Glial Cells Shape Pathology and Repair After Spinal Cord Injury. *Neurotherapeutics,* 15**,** 554-577.
GEORGE, J., HSU, C. C., NGUYEN, L. T. B., YE, H. & CUI, Z. 2020. Neural tissue engineering with structured hydrogels in CNS models and therapies. *Biotechnol Adv,* 42**,** 107370.
GEORGE, J. H., NAGEL, D., WALLER, S., HILL, E., PARRI, H. R., COLEMAN, M. D., CUI, Z. & YE, H. 2018. A closer look at neuron interaction with track-etched microporous membranes. *Scientific Reports,* 19.
GORDON, A. & GESCHWIND, D. H. 2020. Human in vitro models for understanding mechanisms of autism spectrum disorder. *Mol Autism,* 11**,** 26.
GORDON, A., YOON, S. J., TRAN, S. S., MAKINSON, C. D., PARK, J. Y., ANDERSEN, J., VALENCIA, A. M., HORVATH, S., XIAO, X., HUGUENARD, J. R., PASCA, S. P. & GESCHWIND, D. H. 2021. Long-term maturation of human cortical organoids matches key early postnatal transitions. *Nat Neurosci,* 24**,** 331-342.
GRACIA LÓPEZ-CARBALLO, LUCRECIA MORENO, SUSANA MASIÁ, PALOMA PÉREZ & BARETTINO, D. 2002. Activation of the phosphatidylinositol 3-kinase/Akt signaling pathway by retinoic acid is required for neural differentiation of SH-SY5Y human neuroblastoma cells. *J Biol Chem,* 277**,** 297-304.
GRAHAM, V., KHUDYAKOV, J., ELLIS, P. & PEVNY, L. 2003. SOX2 functions to maintain neural progenitor identity. *Neuron,* 39**,** 749-65.
GRAUPENSPERGER, S., SWEET, S. N. & EVANS, M. B. 2018. Multimorbidity of overweight and obesity alongside anxiety and depressive disorders in individuals with spinal cord injury. *J Spinal Cord Med***,** 1-9.
GREBENYUK, S. & RANGA, A. 2019. Engineering Organoid Vascularization. *Front Bioeng Biotechnol,* 7**,** 39.
GREEN, M. A., BILSTON, L. E. & SINKUS, R. 2008. In vivo brain viscoelastic properties measured by magnetic resonance elastography. *NMR Biomed,* 21**,** 755-64.
GYLLENSTEN, L. & MALMFORS, T. 1963. Myelinization of the optic nerve and its dependence on visual function--a quantitative investigation in mice. *J Embryol Exp Morphol,* 11**,** 255-66.
HACHEM, L. D., AHUJA, C. S. & FEHLINGS, M. G. 2017. Assessment and management of acute spinal cord injury: From point of injury to rehabilitation. *Journal of Spinal Cord Medicine,* 40**,** 665-675.
HAERI, M. & HAERI, M. 2015. ImageJ Plugin for Analysis of Porous Scaffolds used in Tissue Engineering. *Journal of Open Research Software,* 3.
HAGEMANN, C., MORENO GONZALEZ, C., GUETTA, L., TYZACK, G., CHIAPPINI, C., LEGATI, A., PATANI, R. & SERIO, A. 2022. Axonal Length Determines Distinct Homeostatic Phenotypes in Human iPSC Derived Motor Neurons on a Bioengineered Platform. *Adv Healthc Mater,* 11**,** e2101817.
HAMHABER, U., SACK, I., PAPAZOGLOU, S., RUMP, J., KLATT, D. & BRAUN, J. 2007. Three-dimensional analysis of shear wave propagation observed by in vivo magnetic resonance elastography of the brain. *Acta Biomater,* 3**,** 127-37.
HE, Y., LV, B., HUAN, Y., LIU, B., LI, Y., JIA, L., QU, C., WANG, D., YU, H. & YUAN, H. 2018. Zhenbao pill protects against acute spinal cord injury via miR-146a-5p regulating the expression of GPR17. *Biosci Rep,* 38.
HIEMSTRA, C., VAN DER AA, L. J., ZHONG, Z. Y., DIJKSTRA, P. J. & FEIJEN, J. 2007a. Rapidly in situ-forming degradable hydrogels from dextran thiols through michael addition. *Biomacromolecules,* 8**,** 1548-1556.
HIEMSTRA, C., ZHOU, W., ZHONG, Z. Y., WOUTERS, M. & FEIJEN, J. 2007b. Rapidly in situ forming biodegradable robust hydrogels by combining stereocomplexation and photopolymerization. *Journal of the American Chemical Society,* 129**,** 9918-9926.

HIROSHI TAKAHASHI, MASASHI YAMAZAKI, AKIHIKO OKAWA, TSUYOSHI SAKUMA, KEI KATO, MITSUHIRO HASHIMOTO, KOICHI HAYASHI, TAKEO FURUYA, TAKAYUKI FUJIYOSHI, JUNKO KAWABE, TOMONORI YAMAUCHI, CHIKATO MANNOJI, TOMOHIRO MIYASHITA, RYO KADOTA, MASAYUKI HASHIMOTO, YASUO ITO, TAKAHASHI, K. & KODA, M. 2012. Neuroprotective therapy using granulocyte colony-stimulating factor for acute spinal cord injury: a phase I/IIa clinical trial. *European Spine Journal,* 21**,** 2580-2587.
HONG, J., YEO, M., YANG, G. H. & KIM, G. 2019. Cell-Electrospinning and Its Application for Tissue Engineering. *Int J Mol Sci,* 20.
HONG, S., DISSING-OLESEN, L. & STEVENS, B. 2016. New insights on the role of microglia in synaptic pruning in health and disease. *Curr Opin Neurobiol,* 36**,** 128-34.
HONG, Y. J. & DO, J. T. 2019. Neural Lineage Differentiation From Pluripotent Stem Cells to Mimic Human Brain Tissues. *Front Bioeng Biotechnol,* 7**,** 400.
HOSSEINI, V., AHADIAN, S., OSTROVIDOV, S., CAMCI-UNAL, G., CHEN, S., KAJI, H., RAMALINGAM, M. & KHADEMHOSSEINI, A. 2012. Engineered contractile skeletal muscle tissue on a microgrooved methacrylated gelatin substrate. *Tissue Eng Part A,* 18**,** 2453-65.
HUANG, H. Y., CHEN, L., WANG, H. M., XIU, B., LI, B. C., WANG, R., ZHANG, J., ZHANG, F., GU, Z., LI, Y., SONG, Y. L., HAO, W., PANG, S. Y. & SUN, J. Z. 2003. Influence of patients' age on functional recovery after transplantation of olfactory ensheathing cells into injured spinal cord injury. *Chinese Medical Journal,* 116**,** 1488-1491.
HUANG, J., WU, C., XU, G., SUN, Y., GUI, C., FU, J., CUI, Z. & HUANG, H. 2022. The decreased expression of miR-429 in plasma exosomes after spinal cord injury inhibits neuronal apoptosis by mediating the PTEN/PI3K/Akt pathway. *Ann Transl Med,* 10**,** 6.
HULTBORN, H. 2006. Spinal reflexes, mechanisms and concepts: from Eccles to Lundberg and beyond. *Prog Neurobiol,* 78**,** 215-32.
HUME, S. L., HOYT, S. M., WALKER, J. S., SRIDHAR, B. V., ASHLEY, J. F., BOWMAN, C. N. & BRYANT, S. J. 2012. Alignment of multi-layered muscle cells within three-dimensional hydrogel macrochannels. *Acta Biomater,* 8**,** 2193-2202.
HUNT, N. C. & GROVER, L. M. 2010. Cell encapsulation using biopolymer gels for regenerative medicine. *Biotechnology Letters,* 32**,** 733-742.
HURTADO, A., CREGG, J. M., WANG, H. B., WENDELL, D. F., OUDEGA, M., GILBERT, R. J. & MCDONALD, J. W. 2011. Robust CNS regeneration after complete spinal cord transection using aligned poly-L-lactic acid microfibers. *Biomaterials,* 32**,** 6068-6079.
IIZAWA, T., TAKETA, H., MARUTA, M., ISHIDO, T., GOTOH, T. & SAKOHARA, S. 2007. Synthesis of porous poly(N-isopropylacrylamide) gel beads by sedimentation polymerization and their morphology. *Journal of Applied Polymer Science,* 104**,** 842-850.
ITANO, Y., ITO, A., UEHARA, T. & NOMURA, Y. 1996. Regulation of Bcl-2 protein expression in human neuroblastoma SH-SY5Y cells: positive and negative effects of protein kinases C and A, respectively. *J Neurochem,* 67**,** 131-7.
J.TUCHOLSKI, M.LESORT & G.V.W.JOHNSON 2001. Tissue transglutaminase is essential for neurite outgrowth in human neuroblastoma SH-SY5Y cells. *Neuroscience,* 102**,** 481-491.
JESSICA J. SENIOR, MEGAN E. COOKE, LIAM M. GROVER & SMITH, A. M. 2019. Fabrication of Complex Hydrogel Structures Using Suspended Layer Additive Manufacturing (SLAM). *Advanced Functional Materials,* 29.
JIANG, Y., CHEN, J., DENG, C., SUURONEN, E. J. & ZHONG, Z. 2014. Click hydrogels, microgels and nanogels: emerging platforms for drug delivery and tissue engineering. *Biomaterials,* 35**,** 4969-85.
JOHANSSON, C. B., SVENSSON, M., WALLSTEDT, L., JANSON, A. M. & FRISEN, J. 1999. Neural stem cells in the adult human brain. *Exp Cell Res,* 253**,** 733-6.
JORBA, I., MENAL, M. J., M., T., GOZALE, D., PIÑOL-RIPOL, G., COLELL, A., MONTSERRAT, J. M., NAVAJAS, D., FARRÉ, R. & ALMENDROS, I. 2017. Ageing and chronic intermittent hypoxia mimicking sleep apnea do not modify local brain tissue stiffness in healthy mice. *Journal of the Mechanical Behaviour of Biomedical Materials,* 71**,** 106-113.
JULIET, P. A., FROST, E. E., BALASUBRAMANIAM, J. & DEL BIGIO, M. R. 2009. Toxic effect of blood components on perinatal rat subventricular zone cells and oligodendrocyte precursor cell proliferation, differentiation and migration in culture. *J Neurochem,* 109**,** 1285-99.
JUMING TANG, MARVIN A. TUNG & YANYUN ZENG 1995. Mechanical Properties of Gellan Gels in Relation to Divalent Cations. *Journal of Food Science,* 60**,** 748-752.

JUNG-YEN YANG, YEN-CHUNG TING, JUIN-YIH LAI, HSUAN-LIANG LIU, HSU-WEI FANG & TSAI, W.-B. 2008. Quantitative analysis of osteoblast-like cells (MG63) morphology on nanogrooved substrata with various groove and ridge dimensions. *Journal of Biomedical Materials Research* 90**,** 629-640.
KANG, K. S., KIM, S. W., OH, Y. H., YU, J. W., KIM, K. Y., PARK, H. K., SONG, C. H. & HAN, H. 2005. A 37-year-old spinal cord-injured female patient, transplanted of multipotent stem cells from human UC blood, with improved sensory perception and mobility, both functionally and morphologically: a case study. *Cytotherapy,* 7**,** 368-373.
KATAKURA, M., HASHIMOTO, M., SHAHDAT, H. M., GAMOH, S., OKUI, T., MATSUZAKI, K. & SHIDO, O. 2009. Docosahexaenoic acid promotes neuronal differentiation by regulating basic helix-loop-helix transcription factors and cell cycle in neural stem cells. *Neuroscience,* 160**,** 651-60.
KATOH, H., YOKOTA, K. & FEHLINGS, M. G. 2019. Regeneration of Spinal Cord Connectivity Through Stem Cell Transplantation and Biomaterial Scaffolds. *Frontiers in Cellular Neuroscience,* 13.
KATSETOS, C. D., LEGIDO, A., PERENTES, E. & MORK, S. J. 2003. Class III beta-tubulin isotype: a key cytoskeletal protein at the crossroads of developmental neurobiology and tumor neuropathology. *J Child Neurol,* 18**,** 851-66; discussion 867.
KEIRSTEAD, H. S., NISTOR, G., BERNAL, G., TOTOIU, M., CLOUTIER, F., SHARP, K. & STEWARD, O. 2005. Human embryonic stem cell-derived oligodendrocyte progenitor cell transplants remyelinate and restore locomotion after spinal cord injury. *J Neurosci,* 25**,** 4694-705.
KERMAN, I., TOPPARE, L., YILMAZ, F. & YAGCI, Y. 2005. Thiophene Ended ∈-Caprolactone Conducting Copolymers and their Electrochromic Properties. *Journal of Macromolecular Science,* 42**,** 509-520.
KIM, C. K., WON, J. S., AN, J. Y., LEE, H. J., NAM, A. J., NAM, H., LEE, J. Y., LEE, K. H., LEE, S. H. & JOO, K. M. 2022. Significant Therapeutic Effects of Adult Human Neural Stem Cells for Spinal Cord Injury Are Mediated by Monocyte Chemoattractant Protein-1 (MCP-1). *Int J Mol Sci,* 23.
KIM, D. S., LEE, D. R., KIM, H. S., YOO, J. E., JUNG, S. J., LIM, B. Y., JANG, J., KANG, H. C., YOU, S., HWANG, D. Y., LEEM, J. W., NAM, T. S., CHO, S. R. & KIM, D. W. 2012. Highly pure and expandable PSA-NCAM-positive neural precursors from human ESC and iPSC-derived neural rosettes. *PLoS One,* 7**,** e39715.
KONDZIOLKA, D., STEINBERG, G. K., CULLEN, S. B. & MCGROGAN, M. 2004. Evaluation of surgical techniques for neuronal cell transplantation used in patients with stroke. *Cell Transplantation,* 13**,** 749-754.
KONDZIOLKA, D., STEINBERG, G. K., WECHSLER, L., MELTZER, C. C., ELDER, E., GEBEL, J., DECESARE, S., JOVIN, T., ZAFONTE, R., LEBOWITZ, J., FLICKINGER, J. C., TONG, D., MARKS, M. P., JAMIESON, C., LUU, D., BELL-STEPHENS, T. & TERAOKA, J. 2005. Neurotransplantation for patients with subcortical motor stroke: a phase 2 randomized trial. *J Neurosurg,* 103**,** 38-45.
KONDZIOLKA, D., WECHSLER, L., GOLDSTEIN, S., MELTZER, C., THULBORN, K. R., GEBEL, J., JANNETTA, P., DECESARE, S., ELDER, E. M., MCGROGAN, M., REITMAN, M. A. & BYNUM, L. 2000. Transplantation of cultured human neuronal cells for patients with stroke. *Neurology,* 55**,** 565-9.
KOTHAPALLI, C., MAHAJAN, G. & FARRELL, K. 2020. Substrate stiffness induced mechanotransduction regulates temporal evolution of human fetal neural progenitor cell phenotype, differentiation, and biomechanics. *Biomater Sci,* 8**,** 5452-5464.
KOVALEVICH, J. & LANGFORD, D. 2013. Considerations for the use of SH-SY5Y neuroblastoma cells in neurobiology. *Methods Mol Biol,* 1078**,** 9-21.
KRUSE, S. A., ROSE, G. H., GLASER, K. J., MANDUCA, A., FELMLEE, J. P., JACK, C. R., JR. & EHMAN, R. L. 2008. Magnetic resonance elastography of the brain. *Neuroimage,* 39**,** 231-7.
KUEH, J. L., LI, D., RAISMAN, G., JENKINS, D., LI, Y. & STEVENS, R. 2012. Directionality and bipolarity of olfactory ensheathing cells on electrospun nanofibers. *Nanomedicine (Lond),* 7**,** 1211-24.

KULANGARA, K., ADLER, A. F., WANG, H., CHELLAPPAN, M., HAMMETT, E., YASUDA, R. & LEONG, K. W. 2014. The effect of substrate topography on direct reprogramming of fibroblasts to induced neurons. *Biomaterials,* 35**,** 5327-5336.
KWON, B. K., OKON, E., HILLYER, J., MANN, C., BAPTISTE, D., WEAVER, L. C., FEHLINGS, M. G. & TETZLAFF, W. 2011. A Systematic Review of Non-Invasive Pharmacologic Neuroprotective Treatments for Acute Spinal Cord Injury. *Journal of Neurotrauma,* 28**,** 1545-1588.
LAM, D., FISCHER, N. O. & ENRIGHT, H. A. 2021. Probing function in 3D neuronal cultures: A survey of 3D multielectrode array advances. *Curr Opin Pharmacol,* 60**,** 255-260.
LANKFORD, K. L., IMAIZUMI, T., HONMOU, O. & KOCSIS, J. D. 2002. A quantitative morphometric analysis of rat spinal cord remyelination following transplantation of allogenic Schwann cells. *J Comp Neurol,* 443**,** 259-74.
LEILA F. DERAVI, NINA R. SINATRA, CHRISTOPHE O. CHANTRE, ALEXANDER P. NESMITH, HONGYAN YUAN, SAHM K. DERAVI, JOSUE A. GOSS, LUKE A. MACQUEEN, MOHAMMAD R. BADROSSAMY, GRANT M. GONZALEZ, MICHAEL D. PHILLIPS & PARKER, K. K. 2017. Design and Fabrication of Fibrous Nanomaterials Using Pull Spinning. *Macromolecular Materials and Engineering,* 302.
LI, J. & LEPSKI, G. 2013. Cell Transplantation for Spinal Cord Injury: A Systematic Review. *Biomed Research International,* 2013.
LI, J. & MOONEY, D. J. 2016. Designing hydrogels for controlled drug delivery. *Nat Rev Mater,* 1.
LI, Q. & BARRES, B. A. 2018. Microglia and macrophages in brain homeostasis and disease. *Nat Rev Immunol,* 18**,** 225-242.
LI, W., SUN, W., ZHANG, Y., WEI, W., AMBASUDHAN, R., XIA, P., TALANTOVA, M., LIN, T., KIM, J., WANG, X., KIM, W. R., LIPTON, S. A., ZHANG, K. & DING, S. 2011. Rapid induction and long-term self-renewal of primitive neural precursors from human embryonic stem cells by small molecule inhibitors. *Proc Natl Acad Sci U S A,* 108**,** 8299-304.
LI, Y., LIU, M., YAN, Y. & YANG, S. T. 2014. Neural differentiation from pluripotent stem cells: The role of natural and synthetic extracellular matrix. *World J Stem Cells,* 6**,** 11-23.
LILLEY, E., ANDREWS, M. R., BRADBURY, E. J., ELLIOTT, H., HAWKINS, P., ICHIYAMA, R. M., KEELEY, J., MICHAEL-TITUS, A. T., MOON, L. D. F., PLUCHINO, S., RIDDELL, J., RYDER, K. & YIP, P. K. 2020. Refining rodent models of spinal cord injury. *Exp Neurol,* 328**,** 113273.
LIM, J. Y., HANSEN, J. C., SIEDLECKI, C. A., RUNT, J. & DONAHUE, H. J. 2005. Human foetal osteoblastic cell response to polymer-demixed nanotopographic interfaces. *J R Soc Interface,* 2**,** 97-108.
LIN, C. C. & JR, L. E. C. 1984. Gelrite as a gelling agent for the growth of thermophilic microorganisms. *Applied Environmental Microbiology,* 47**,** 427-427.
LINDEROTH, B. & FOREMAN, R. D. 1999. Physiology of spinal cord stimulation: review and update. *Neuromodulation,* 2**,** 150-64.
LIU, H. Q., EDEL, J. B., BELLAN, L. M. & CRAIGHEAD, H. G. 2006. Electrospun polymer nanofibers as subwavelength optical waveguides incorporating quantum dots. *Small,* 2**,** 495-499.
LIU, J., TU, H., ZHANG, D., ZHENG, H. & LI, Y. L. 2012. Voltage-gated sodium channel expression and action potential generation in differentiated NG108-15 cells. *BMC Neurosci,* 13**,** 129.
LIU, S. Q., MA, Y. G., PENG, H. & FAN, L. 2005. Monocyte chemoattractant protein-1 level in serum of patients with acute spinal cord injury. *Chin J Traumatol,* 8**,** 216-9.
LIU, Y., YE, H., SATKUNENDRARAJAH, K., YAO, G. S., BAYON, Y. & FEHLINGS, M. G. 2013. A self-assembling peptide reduces glial scarring, attenuates post-traumatic inflammation and promotes neurological recovery following spinal cord injury. *Acta Biomater,* 9**,** 8075-88.
LIU, Z. Q. 1991. Scale space approach to directional analysis of images. *Appl Opt,* 30**,** 1369-73.
LIZARRAGA-VALDERRAMA, L. R., TAYLOR, C. S., CLAEYSSENS, F., HAYCOCK, J. W., KNOWLES, J. C. & ROY, I. 2019. Unidirectional neuronal cell growth and differentiation on aligned polyhydroxyalkanoate blend microfibres with varying diameters. *J Tissue Eng Regen Med,* 13**,** 1581-1594.

LOBENWEIN, D., TEPEKOYLU, C., KOZARYN, R., PECHRIGGL, E. J., BITSCHE, M., GRABER, M., FRITSCH, H., SEMSROTH, S., STEFANOVA, N., PAULUS, P., CZERNY, M., GRIMM, M. & HOLFELD, J. 2015. Shock Wave Treatment Protects From Neuronal Degeneration via a Toll-Like Receptor 3 Dependent Mechanism: Implications of a First-Ever Causal Treatment for Ischemic Spinal Cord Injury. *J Am Heart Assoc,* 4**,** e002440.
LOPES FM, SCHRODER R, DA FROTA ML, J., ZANOTTO-FILHO A, MULLER CB, PIRES AS, MEURER RT, COLPO GD, GELAIN DP, KAPCZINSKI F, MOREIRA JC, FERNANDES MDA C & F., K. 2010. Comparison between proliferative and neuron-like SH-SY5Y cells as an in vitro model for Parkinson disease studies. *Brain Res,* 1337.
LORD, M. S., FOSS, M. & BESENBACHER, F. 2010. Influence of nanoscale surface topography on protein adsorption and cellular response. *Nano Today,* 5**,** 66-78.
LU, D., YANG, Y., ZHANG, P., MA, Z., LI, W., SONG, Y., FENG, H., YU, W., REN, F., LI, T., ZENG, H. & WANG, J. 2022. Development and Application of Three-Dimensional Bioprinting Scaffold in the Repair of Spinal Cord Injury. *Tissue Eng Regen Med*.
LUANA PERSANO, ANDREA CAMPOSEO, CAGRI TEKMEN & PISIGNANO, D. 2013. Industrial Upscaling of Electrospinning and Applications of Polymer Nanofibers: A Review. *Macromolecular Materials and Engineering,* 298**,** 504-520.
LUCIA SLOVINSKA, JURAJ BLASKO, MIRIAM NAGYOVA, SZEKIOVA, E. & CIZKOVA, D. 2015. In Vitro Models of Spinal Cord Injury. *Recovery of Motor Function Following Spinal Cord Injury*.
LÜHMANN, T. & HALL, H. 2009. Cell Guidance by 3D-Gradients in Hydrogel Matrices: Importance for Biomedical Applications. *Materials* 2**,** 1058-1083.
MADSEN, C. G., SKOV, A., BALDURSDOTTIR, S., RADES, T., JORGENSEN, L. & MEDLICOTT, N. J. 2015. Simple measurements for prediction of drug release from polymer matrices - Solubility parameters and intrinsic viscosity. *Eur J Pharm Biopharm,* 92**,** 1-7.
MAEDA, Y., OTSUKA, T., TAKEDA, M., OKAZAKI, T., SHIMIZU, K., KUWABARA, M., HOSOGAI, M., YUGE, L. & MITSUHARA, T. 2021. Transplantation of rat cranial bone-derived mesenchymal stem cells promotes functional recovery in rats with spinal cord injury. *Sci Rep,* 11**,** 21907.
MALIK, N. & RAO, M. S. 2013. A review of the methods for human iPSC derivation. *Methods Mol Biol,* 997**,** 23-33.
MCCAUGHEY, E. J., PURCELL, M., MCLEAN, A. N., FRASER, M. H., BEWICK, A., BOROTKANICS, R. J. & ALLAN, D. B. 2016. Changing demographics of spinal cord injury over a 20-year period: a longitudinal population-based study in Scotland. *Spinal Cord,* 54**,** 270-276.
MCCORRY, L. K. 2007. Physiology of the autonomic nervous system. *Am J Pharm Educ,* 71**,** 78.
MCDAID, D., PARK, A. L., GALL, A., PURCELL, M. & BACON, M. 2019. Understanding and modelling the economic impact of spinal cord injuries in the United Kingdom. *Spinal Cord,* 57**,** 778-788.
MCGONIGLE, P. 2014. Animal models of CNS disorders. *Biochemical Pharmacology,* 87**,** 140-149.
MEDBERRY, C. J., CRAPO, P. M., SIU, B. F., CARRUTHERS, C. A., WOLF, M. T., NAGARKAR, S. P., AGRAWAL, V., JONES, K. E., KELLY, J., JOHNSON, S. A., VELANKAR, S. S., WATKINS, S. C., MODO, M. & BADYLAK, S. F. 2013. Hydrogels derived from central nervous system extracellular matrix. *Biomaterials,* 34**,** 1033-40.
MELINO, G., THIELE, C. J., KNIGHT, R. A. & PIACENTINI, M. 1997. Retinoids and the control of growth/death decisions in human neuroblastoma cell lines. *J Neurooncol,* 31**,** 65-83.
MESHKINI, A., SALEHPOUR, F., AGHAZADEH, J., MIRZAEI, F. & NASERI ALAVI, S. A. 2018. Riluzole Can Improve Sensory and Motor Function in Patients with Acute Spinal Cord Injury. *Asian J Neurosurg,* 13**,** 656-659.
MIGLIORINI, C., TONGE, B. & TALEPOROS, G. 2008. Spinal cord injury and mental health. *Australian and New Zealand Journal of Psychiatry,* 42**,** 309-314.
MIJAILOVIC, A. S., GALARZA, S., RAAYAI-ARDAKANI, S., BIRCH, N. P., SCHIFFMAN, J. D., CROSBY, A. J., COHEN, T., PEYTON, S. R. & VAN VLIET, K. J. 2021. Localized characterization of brain tissue mechanical properties by needle induced cavitation rheology and volume controlled cavity expansion. *J Mech Behav Biomed Mater,* 114**,** 104168.

MILLER, C., JEFTINIJA, S. & MALLAPRAGADA, S. 2002. Synergistic effects of physical and chemical guidance cues on neurite alignment and outgrowth on biodegradable polymer substrates. *Tissue Eng,* 8**,** 367-78.
MILLWARD, J. M., GUO, J., BERNDT, D., BRAUN, J., SACK, I. & INFANTE-DUARTE, C. 2015. Tissue structure and inflammatory processes shape viscoelastic properties of the mouse brain. *NMR Biomed,* 28**,** 831-9.
MING, G. L. & SONG, H. 2011. Adult neurogenesis in the mammalian brain: significant answers and significant questions. *Neuron,* 70**,** 687-702.
MOEENDARBARY, E., WEBER, I. P., SHERIDAN, G. K., KOSER, D. E., SOLEMAN, S., HAENZI, B., BRADBURY, E. J., FAWCETT, J. & FRANZE, K. 2017. The soft mechanical signature of glial scars in the central nervous system. *Nat Commun,* 8**,** 14787.
MORAUD, E. M., CAPOGROSSO, M., FORMENTO, E., WENGER, N., DIGIOVANNA, J., COURTINE, G. & MICERA, S. 2016. Mechanisms Underlying the Neuromodulation of Spinal Circuits for Correcting Gait and Balance Deficits after Spinal Cord Injury. *Neuron,* 89**,** 814-28.
MORELLI, S., PISCIONERI, A., SALERNO, S. & DE BARTOLO, L. 2022. Hollow Fiber and Nanofiber Membranes in Bioartificial Liver and Neuronal Tissue Engineering. *Cells Tissues Organs,* 211**,** 447-476.
MORONI, L., BURDICK, J. A., HIGHLEY, C., LEE, S. J., MORIMOTO, Y., TAKEUCHI, S. & YOO, J. J. 2018. Biofabrication strategies for 3D in vitro models and regenerative medicine. *Nat Rev Mater,* 3**,** 21-37.
MORRIS, E. R., NISHINARI, K. & RINAUDO, M. 2012. Gelation of gellan – A review. *Food Hydrocolloids,* 28**,** 373-411.
MOXON, S. R. 2016. *DEVELOPMENT OF BIOPOLYMER HYDROGELS AS COMPLEX TISSUE ENGINEERING SCAFFOLDS.* Doctoral thesis, University of Huddersfield.
MUANGSANIT, P., ROBERTON, V., COSTA, E. & PHILLIPS, J. B. 2021. Engineered aligned endothelial cell structures in tethered collagen hydrogels promote peripheral nerve regeneration. *Acta Biomater,* 126**,** 224-237.
N.MOLINA, AGUIRRE, J. & WALCZAK, M. 2019. Application of FFT analysis for the study of directionality of wear scars in exposure to slurry flow of varying velocity. *Wear,* 426-427**,** 589-595.
NAGOSHI, N., OKANO, H. & NAKAMURA, M. 2020. Regenerative therapy for spinal cord injury using iPSC technology. *Inflamm Regen,* 40**,** 40.
NAS, K., YAZMALAR, L., SAH, V., AYDIN, A. & ONES, K. 2015. Rehabilitation of spinal cord injuries. *World J Orthop,* 6**,** 8-16.
NECTOW, A. R., KILMER, M. E. & KAPLAN, D. L. 2014. Quantifying cellular alignment on anisotropic biomaterial platforms. *J Biomed Mater Res A,* 102**,** 420-8.
NGUYEN, M. D., JULIEN, J. P. & RIVEST, S. 2002. Innate immunity: The missing link in neuroprotection and neurodegeneration? *Nature Reviews Neuroscience,* 3**,** 216-227.
NICOLLE, S., LOUNIS, M., WILLINGER, R. & PALIERNE, J. F. 2005. Shear linear behavior of brain tissue over a large frequency range. *Biorheology,* 42**,** 209-23.
NOREAU, L. & FOUGEYROLLAS, P. 2000. Long-term consequences of spinal cord injury on social participation: the occurrence of handicap situations. *Disabil Rehabil,* 22**,** 170-80.
OKUBO, T., NAGOSHI, N., KOHYAMA, J., TSUJI, O., SHINOZAKI, M., SHIBATA, S., KASE, Y., MATSUMOTO, M., NAKAMURA, M. & OKANO, H. 2018. Treatment with a Gamma-Secretase Inhibitor Promotes Functional Recovery in Human iPSC- Derived Transplants for Chronic Spinal Cord Injury. *Stem Cell Reports,* 11**,** 1416-1432.
OSTROVIDOV, S., HOSSEINI, V., AHADIAN, S., FUJIE, T., PARTHIBAN, S. P., RAMALINGAM, M., BAE, H., KAJI, H. & KHADEMHOSSEINI, A. 2014. Skeletal muscle tissue engineering: Methods to form skeletal myotubes and their applications. *Tissue Engineering* 20**,** 403-436.
OTSUKA, T., MAEDA, Y., KUROSE, T., NAKAGAWA, K., MITSUHARA, T., KAWAHARA, Y. & YUGE, L. 2021. Comparisons of Neurotrophic Effects of Mesenchymal Stem Cells Derived from Different Tissues on Chronic Spinal Cord Injury Rats. *Stem Cells Dev,* 30**,** 865-875.
OYINBO, C. A. 2011. Secondary injury mechanisms in traumatic spinal cord injury: a nugget of this multiply cascade. *Acta Neurobiologiae Experimentalis,* 71**,** 281-299.
PAOLI, P., GIANNONI, E. & CHIARUGI, P. 2013. Anoikis molecular pathways and its role in cancer progression. *Biochim Biophys Acta,* 1833**,** 3481-3498.

PARKINS, C. C., MCABEE, J. H., RUFF, L., WENDLER, A., MAIR, R., GILBERTSON, R. J., WATTS, C. & SCHERMAN, O. A. 2021. Mechanically matching the rheological properties of brain tissue for drug-delivery in human glioblastoma models. *Biomaterials,* 276**,** 120919.
PASCUAL, G., SOTOMAYOR, S., RODRIGUEZ, M., PEREZ-KOHLER, B., KUHNHARDT, A., FERNANDEZ-GUTIERREZ, M., SAN ROMAN, J. & BELLON, J. M. 2016. Cytotoxicity of Cyanoacrylate-Based Tissue Adhesives and Short-Term Preclinical In Vivo Biocompatibility in Abdominal Hernia Repair. *PLoS One,* 11**,** e0157920.
PATAR, A., DOCKERY, P., HOWARD, L. & MCMAHON, S. S. 2019. Cell viability in three ex vivo rat models of spinal cord injury. *J Anat,* 234**,** 244-251.
PEARSE, D. D. & BUNGE, M. B. 2006. Designing cell- and gene-based regeneration strategies to repair the injured spinal cord. *Journal of Neurotrauma,* 23**,** 438-452.
PENNEY, J., RALVENIUS, W. T. & TSAI, L. H. 2020. Modeling Alzheimer's disease with iPSC-derived brain cells. *Mol Psychiatry,* 25**,** 148-167.
PICCININI, F., TESEI, A., ARIENTI, C. & BEVILACQUA, A. 2017. Cell Counting and Viability Assessment of 2D and 3D Cell Cultures: Expected Reliability of the Trypan Blue Assay. *Biol Proced Online,* 19**,** 8.
PICOLLET-D'HAHAN, N., DOLEGA, M. E., LIGUORI, L., MARQUETTE, C., LE GAC, S., GIDROL, X. & MARTIN, D. K. 2016. A 3D Toolbox to Enhance Physiological Relevance of Human Tissue Models. *Trends Biotechnol,* 34**,** 757-769.
PINHO, A. G., CIBRAO, J. R., SILVA, N. A., MONTEIRO, S. & SALGADO, A. J. 2020. Cell Secretome: Basic Insights and Therapeutic Opportunities for CNS Disorders. *Pharmaceuticals (Basel),* 13.
PITTENGER, M. F., DISCHER, D. E., PEAULT, B. M., PHINNEY, D. G., HARE, J. M. & CAPLAN, A. I. 2019. Mesenchymal stem cell perspective: cell biology to clinical progress. *NPJ Regen Med,* 4**,** 22.
PLUNET, W., KWON, B. K. & TETZLAFF, W. 2002. Promoting axonal regeneration in the central nervous system by enhancing the cell body response to axotomy. *J Neurosci Res,* 68**,** 1-6.
POPA, C., POPA, F., GRIGOREAN, V. T., ONOSE, G., SANDU, A. M., POPESCU, M., BURNEI, G., STRAMBU, V. & SINESCU, C. 2010. Vascular dysfunctions following spinal cord injury. *J Med Life,* 3**,** 275-85.
PRESGRAVES, S. P., AHMED, T., BORWEGE, S. & JOYCE, J. N. 2004. Terminally differentiated SH-SY5Y cells provide a model system for studying neuroprotective effects of dopamine agonists. *Neurotox Res,* 5**,** 579-98.
PRINS, R. M. & LIAU, L. M. 2003. Immunology and immunotherapy in neurosurgical disease. *Neurosurgery,* 53**,** 144-152.
PUPPI, D., MOTA, C., GAZZARRI, M., DINUCCI, D., GLORIA, A., MYRZABEKOVA, M., AMBROSIO, L. & CHIELLINI, F. 2012. Additive manufacturing of wet-spun polymeric scaffolds for bone tissue engineering. *Biomed Microdevices,* 14**,** 1115-27.
QIAN, X., SONG, H. & MING, G. L. 2019. Brain organoids: advances, applications and challenges. *Development,* 146.
QUAN, Q., MENG, H.-Y., CHANG, B., LIU, G.-B., CHENG, X.-Q., TANG, H., WANG, Y., PENG, J., ZHAO, Q. & LU, S.-B. 2019. Aligned fibers enhance nerve guide conduits when bridging peripheral nerve defects focused on early repair stage. *Neural Regenerative Research,* 14**,** 903-912.
RAISMAN, G. & LI, Y. 2007. Repair of neural pathways by olfactory ensheathing cells. *Nat Rev Neurosci,* 8**,** 312-9.
RAJNICEK, A., BRITLAND, S. & MCCAIG, C. 1997. Contact guidance of CNS neurites on grooved quartz: influence of groove dimensions, neuronal age and cell type. *J Cell Sci,* 110 (Pt 23)**,** 2905-13.
RAMÍREZ HERNÁNDEZ, A., CRISANTO CONTRERAS, O., CONDE ACEVEDO, J. & NAVARRO MORENO, L. G. 2013. Poly(∈-caprolactone) Degradation Under Acidic and Alkaline Conditions. *American Journal of Polymer Science,* 3**,** 70-75.
RANJAN, V. D., ZENG, P., LI, B. & ZHANG, Y. 2020. In vitro cell culture in hollow microfibers with porous structures. *Biomater Sci,* 8**,** 2175-2188.
RAO, M. & SOCKANATHAN, S. 2005. Transmembrane protein GDE2 induces motor neuron differentiation in vivo. *Science,* 309**,** 2212-5.

RAO, V. M., DELANEY, R. A. & SKINNER, G. 1986. Rheological properties of solid foods. *Engineering properties of foods*, 215-226.
REPIC, T., MADIRAZZA, K., BEKTUR, E. & SAPUNAR, D. 2016. Characterization of dorsal root ganglion neurons cultured on silicon micro-pillar substrates. *Sci Rep,* 6, 39560.
RIEK, K., MILLWARD, J. M., HAMANN, I., MUELLER, S., PFUELLER, C. F., PAUL, F., BRAUN, J., INFANTE-DUARTE, C. & SACK, I. 2012. Magnetic resonance elastography reveals altered brain viscoelasticity in experimental autoimmune encephalomyelitis. *Neuroimage Clin,* 1, 81-90.
ROBERTS, T. T., LEONARD, G. R. & CEPELA, D. J. 2017. Classifications In Brief: American Spinal Injury Association (ASIA) Impairment Scale. *Clin Orthop Relat Res,* 475, 1499-1504.
ROSS, R. A., SPENGLER, B. A. & BIEDLER, J. L. 1983. Coordinate morphological and biochemical interconversion of human neuroblastoma cells. *J Natl Cancer Inst,* 71, 741-7.
RUPENTHAL, I. D., GREEN, C. R. & ALANY, R. G. 2011a. Comparison of ion-activated in situ gelling systems for ocular drug delivery. Part 1: physicochemical characterisation and in vitro release. *Int J Pharm,* 411, 69-77.
RUPENTHAL, I. D., GREEN, C. R. & ALANY, R. G. 2011b. Comparison of ion-activated in situ gelling systems for ocular drug delivery. Part 2: Precorneal retention and in vivo pharmacodynamic study. *Int J Pharm,* 411, 78-85.
RYU, Y., IWASHITA, M., LEE, W., UCHIMURA, K. & KOSODO, Y. 2021. A Shift in Tissue Stiffness During Hippocampal Maturation Correlates to the Pattern of Neurogenesis and Composition of the Extracellular Matrix. *Front Aging Neurosci,* 13, 709620.
SACHS, P. C., MOLLICA, P. A. & BRUNO, R. D. 2017. Tissue specific microenvironments: a key tool for tissue engineering and regenerative medicine. *J Biol Eng,* 11, 34.
SALGADO, C. L., SANCHEZ, E. M., ZAVAGLIA, C. A. & GRANJA, P. L. 2012. Biocompatibility and biodegradation of polycaprolactone-sebacic acid blended gels. *J Biomed Mater Res A,* 100, 243-51.
SANDEAN, D. 2020. Management of acute spinal cord injury: A summary of the evidence pertaining to the acute management, operative and non-operative management. *World J Orthop,* 11, 573-583.
SANDERSON, G. R. & CLARK, R. C. 1984. Gellan gum, a new gelling polysaccharide. *Gums and stabilisers for the food industry,* 2, 201-210.
SANG, L. L., LIU, Y. Q., HUA, W. X., XU, K. G., WANG, G. B., ZHONG, W., WANG, L. Y., XU, S., XING, M. M. Q. & QIU, X. Z. 2016. Thermally sensitive conductive hydrogel using amphiphilic crosslinker self-assembled carbon nanotube to enhance neurite outgrowth and promote spinal cord regeneration. *Rsc Advances,* 6, 26341-26351.
SANTIAGO-TOLEDO, G., GEORGIOU, M., DOS REIS, J., ROBERTON, V. H., VALINHAS, A., WOOD, R. C., PHILLIPS, J. B., MASON, C., LI, D., LI, Y., SINDEN, J. D., CHOI, D., JAT, P. S. & WALL, I. B. 2019. Generation of c-MycER(TAM)-transduced human late-adherent olfactory mucosa cells for potential regenerative applications. *Sci Rep,* 9, 13190.
SEKI, T., HORI, T., MIYATA, H., MAEHARA, M. & NAMBA, T. 2019. Analysis of proliferating neuronal progenitors and immature neurons in the human hippocampus surgically removed from control and epileptic patients. *Sci Rep,* 9, 18194.
SEZER, N., AKKUS, S. & UGURLU, F. G. 2015. Chronic complications of spinal cord injury. *World Journal of Orthopedics,* 6, 24-33.
SHAHRIZAN, M. S. M., AZIZ, Z. H. A. & KATAS, H. 2022. Fluid gels: A systematic review towards their application in pharmaceutical dosage forms and drug delivery systems. *Journal of Drug Delivery Science and Technology,* 67.
SHALLARD, A. & MAYOR, R. 2020. All Roads Lead to Directional Cell Migration. *Trends in Cell Biology,* 30, 852-868.
SHARIF-ALHOSEINI, M., KHORMALI, M., REZAEI, M., SAFDARIAN, M., HAJIGHADERY, A., KHALATBARI, M. M., SAFDARIAN, M., MEKNATKHAH, S., REZVAN, M., CHALANGARI, M., DERAKHSHAN, P. & RAHIMI-MOVAGHAR, V. 2017. Animal models of spinal cord injury: a systematic review. *Spinal Cord,* 55, 714-721.
SHI, Y., KIRWAN, P. & LIVESEY, F. J. 2012. Directed differentiation of human pluripotent stem cells to cerebral cortex neurons and neural networks. *Nat Protoc,* 7, 1836-46.
SHIMOJO, D., ONODERA, K., DOI-TORII, Y., ISHIHARA, Y., HATTORI, C., MIWA, Y., TANAKA, S., OKADA, R., OHYAMA, M., SHOJI, M., NAKANISHI, A., DOYU, M., OKANO, H.

& OKADA, Y. 2015. Rapid, efficient, and simple motor neuron differentiation from human pluripotent stem cells. *Mol Brain,* 8**,** 79.
SHIMOMURA, K. & KAMADA, H. 1986. Roles of gelling agents in plant tissue culture. *Plant Tissue Culture* 3**,** 38-41.
SHIN, H., JEONG, S., LEE, J. H., SUN, W., CHOI, N. & CHO, I. J. 2021. 3D high-density microelectrode array with optical stimulation and drug delivery for investigating neural circuit dynamics. *Nat Commun,* 12**,** 492.
SILVA, N. A., SOUSA, N., REIS, R. L. & SALGADO, A. J. 2014. From basics to clinical: a comprehensive review on spinal cord injury. *Prog Neurobiol,* 114**,** 25-57.
SIMONS, M. & TRAJKOVIC, K. 2006. Neuron-glia communication in the control of oligodendrocyte function and myelin biogenesis. *J Cell Sci,* 119**,** 4381-9.
SKARDAL, A., MACK, D., ATALA, A. & SOKER, S. 2013. Substrate elasticity controls cell proliferation, surface marker expression and motile phenotype in amniotic fluid-derived stem cells. *J Mech Behav Biomed Mater,* 17**,** 307-16.
SOLIMAN, E., BIANCHI, F., SLEIGH, J. N., GEORGE, J. H., CADER, M. Z., CUI, Z. & YE, H. 2018. Aligned electrospun fibers for neural patterning. *Biotechnol Lett,* 40**,** 601-607.
SPENCER, K. C., SY, J. C., FALCON-BANCHS, R. & CIMA, M. J. 2017. A three dimensional in vitro glial scar model to investigate the local strain effects from micromotion around neural implants. *Lab Chip,* 17**,** 795-804.
SREENIVASA RAGHAVAN SANKAVARAM, RAMIL HAKIM, RUXANDRA COVACU, ARVID FROSTELL, SUSANNE NEUMANN, MIKAEL SVENSSON & BRUNDIN, L. 2019. Adult Neural Progenitor Cells Transplanted into Spinal Cord Injury Differentiate into Oligodendrocytes, Enhance Myelination, and Contribute to Recovery. *Stem Cell Reports,* 12**,** 950-966.
SRINIVAS, S., WALI, A. R. & PHAM, M. H. 2019. Efficacy of riluzole in the treatment of spinal cord injury: a systematic review of the literature. *Neurosurg Focus,* 46**,** E6.
STEVENS, L. R., GILMORE, K. J., WALLACE, G. G. & IN HET PANHUIS, M. 2016. Tissue engineering with gellan gum. *Biomater Sci,* 4**,** 1276-90.
STIFANI, N. 2014. Motor neurons and the generation of spinal motor neuron diversity. *Front Cell Neurosci,* 8**,** 293.
STYS, P. K. 1998. Anoxic and ischemic injury of myelinated axons in CNS white matter: From mechanistic concepts to therapeutics. *Journal of Cerebral Blood Flow and Metabolism,* 18**,** 2-25.
SUN, Q., HOU, Y., CHU, Z. & WEI, Q. 2022. Soft overcomes the hard: Flexible materials adapt to cell adhesion to promote cell mechanotransduction. *Bioact Mater,* 10**,** 397-404.
SUN, X., BAI, Y., ZHAI, H., LIU, S., ZHANG, C., XU, Y., ZOU, J., WANG, T., CHEN, S., ZHU, Q., LIU, X., MAO, H. & QUAN, D. 2019. Devising micro/nano-architectures in multi-channel nerve conduits towards a pro-regenerative matrix for the repair of spinal cord injury. *Acta Biomater,* 86**,** 194-206.
TAKAHASHI, K., TANABE, K., OHNUKI, M., NARITA, M., ICHISAKA, T., TOMODA, K. & YAMANAKA, S. 2007. Induction of pluripotent stem cells from adult human fibroblasts by defined factors. *Cell,* 131**,** 861-72.
TALEBIAN, S., MEHRALI, M., TAEBNIA, N., PENNISI, C. P., KADUMUDI, F. B., FOROUGHI, J., HASANY, M., NIKKHAH, M., AKBARI, M., ORIVE, G. & DOLATSHAHI-PIROUZ, A. 2019. Self-Healing Hydrogels: The Next Paradigm Shift in Tissue Engineering? *Adv Sci (Weinh),* 6**,** 1801664.
TAMIELLO, C., BUSKERMOLEN, A. B. C., BAAIJENS, F. P. T., BROERS, J. L. V. & BOUTEN, C. V. C. 2016. Heading in the Right Direction: Understanding Cellular Orientation Responses to Complex Biophysical Environments. *Cell Mol Bioeng,* 9**,** 12-37.
TASKIN, M. E., FRASER, K. H., ZHANG, T., GRIFFITH, B. P. & WU, Z. J. 2010. Micro-scale Modeling of Flow and Oxygen Transfer in Hollow Fiber Membrane Bundle. *J Memb Sci,* 362**,** 172-183.
TATOR, C. H. & FEHLINGS, M. G. 1991. Review of the secondary injury theory of acute spinal cord trauma with emphasis on vascular mechanisms. *J Neurosurg,* 75**,** 15-26.
TEMPLE, S. 1989. Division and differentiation of isolated CNS blast cells in microculture. *Nature,* 340**,** 471-3.
TETZLAFF, W., OKON, E. B., KARIMI-ABDOLREZAEE, S., HILL, C. E., SPARLING, J. S., PLEMEL, J. R., PLUNET, W. T., TSAI, E. C., BAPTISTE, D., SMITHSON, L. J., KAWAJA, M.

D., FEHLINGS, M. G. & KWON, B. K. 2011. A Systematic Review of Cellular Transplantation Therapies for Spinal Cord Injury. *Journal of Neurotrauma,* 28**,** 1611-1682.
THERMOFISHERSCIENTIFIC. 2022. *CellTracker™ Green CMFDA Dye* [Online]. Available: CellTracker™ Green CMFDA Dye [Accessed].
THERMOFISHERSCIENTIFIC 2023. alamarBlue Assays for Cell Viability.
THUMWANIT, V. & KEDJARUNE, U. 1999. Cytotoxicity of polymerized commercial cyanoacrylate adhesive on cultured human oral fibroblasts. *Aust Dent J,* 44**,** 248-52.
TING-YU LAI, JERRY CAO, PU OU-YANG, CHING-YI TSAI, CHIH-WEN LIN, CHIEN-CHIA CHEN, TSAI, M.-K. & LEE, C.-Y. 2022. Different methods of detaching adherent cells and their effects on the cell surface expression of Fas receptor and Fas ligand. *Scientific Reports,* 12.
TOTOIU, M. O. & KEIRSTEAD, H. S. 2005. Spinal cord injury is accompanied by chronic progressive demyelination. *J Comp Neurol,* 486**,** 373-83.
TRIVEDI, A., OLIVAS, A. D. & NOBLE-HAEUSSLEIN, L. J. 2006. Inflammation and Spinal Cord Injury: Infiltrating Leukocytes as Determinants of Injury and Repair Processes. *Clin Neurosci Res,* 6**,** 283-292.
TUIN, S. A., POURDEYHIMI, B. & LOBOA, E. G. 2014. Interconnected, microporous hollow fibers for tissue engineering: commercially relevant, industry standard scale-up manufacturing. *J Biomed Mater Res A,* 102**,** 3311-23.
URZEDO, A. L., GONCALVES, M. C., NASCIMENTO, M. H. M., LOMBELLO, C. B., NAKAZATO, G. & SEABRA, A. B. 2020. Cytotoxicity and Antibacterial Activity of Alginate Hydrogel Containing Nitric Oxide Donor and Silver Nanoparticles for Topical Applications. *ACS Biomater Sci Eng,* 6**,** 2117-2134.
UTZSCHNEIDER, D. A., ARCHER, D. R., KOCSIS, J. D., WAXMAN, S. G. & DUNCAN, I. D. 1994. Transplantation of glial cells enhances action potential conduction of amyelinated spinal cord axons in the myelin-deficient rat. *Proc Natl Acad Sci U S A,* 91**,** 53-7.
VANDENBURGH, H. H. & KARLISCH, P. 1989. Longitudinal growth of skeletal myotubes in vitro in a new horizontal mechanical cell stimulator. *In Vitro Cell Dev Biol,* 25**,** 607-16.
VAPPOU, J., BRETON, E., CHOQUET, P., GOETZ, C., WILLINGER, R. & CONSTANTINESCO, A. 2007. Magnetic resonance elastography compared with rotational rheometry for in vitro brain tissue viscoelasticity measurement. *MAGMA,* 20**,** 273-8.
VILINHAS, A. 2019. Microscale processing to address scale-up challenges in cell therapy manufacture. *Thesis (PhD), University College London*.
W.WELKER, R. 2012. Chapter 1 - Basics and Sampling of Particles for Size Analysis and Identification. *Developments in Surface Contamination and Cleaning***,** 1-80.
WALCZAK, P. A., PEREZ-ESTEBAN, P., BASSETT, D. C. & HILL, E. J. 2021. Modelling the central nervous system: tissue engineering of the cellular microenvironment. *Emerg Top Life Sci,* 5**,** 507-517.
WALTER, T., SHATTUCK, D. W., BALDOCK, R., BASTIN, M. E., CARPENTER, A. E., DUCE, S., ELLENBERG, J., FRASER, A., HAMILTON, N., PIEPER, S., RAGAN, M. A., SCHNEIDER, J. E., TOMANCAK, P. & HERICHE, J. K. 2010. Visualization of image data from cells to organisms. *Nat Methods,* 7**,** S26-41.
WANNER, I. B., DEIK, A., TORRES, M., ROSENDAHL, A., NEARY, J. T., LEMMON, V. P. & BIXBY, J. L. 2008. A new in vitro model of the glial scar inhibits axon growth. *Glia,* 56**,** 1691-709.
WATZLAWICK, R., RIND, J., SENA, E. S., BROMMER, B., ZHANG, T., KOPP, M. A., DIRNAGL, U., MACLEOD, M. R., HOWELLS, D. W. & SCHWAB, J. M. 2016. Olfactory Ensheathing Cell Transplantation in Experimental Spinal Cord Injury: Effect size and Reporting Bias of 62 Experimental Treatments: A Systematic Review and Meta-Analysis. *PLoS Biol,* 14**,** e1002468.
WEI, Z., LIU, J., XIE, H., WANG, B., WU, J. & ZHU, Z. 2021. MiR-122-5p Mitigates Inflammation, Reactive Oxygen Species and SH-SY5Y Apoptosis by Targeting CPEB1 After Spinal Cord Injury Via the PI3K/AKT Signaling Pathway. *Neurochem Res,* 46**,** 992-1005.
WEICKENMEIER, J., DE ROOIJ, R., BUDDAY, S., STEINMANN, P., OVAERT, T. C. & KUHL, E. 2016. Brain stiffness increases with myelin content. *Acta Biomater,* 42**,** 265-272.
WEICKENMEIER, J., KURT, M., OZKAYA, E., DE ROOIJ, R., OVAERT, T. C., EHMAN, R. L., BUTTS PAULY, K. & KUHL, E. 2018. Brain stiffens post mortem. *J Mech Behav Biomed Mater,* 84**,** 88-98.

WEIGHTMAN, A. P., PICKARD, M. R., YANG, Y. & CHARI, D. M. 2014. An in vitro spinal cord injury model to screen neuroregenerative materials. *Biomaterials,* 35**,** 3756-65.
WILKINSON, C. D. W., RIEHLE, M., WOOD, M., GALLAGHER, J. & CURTIS, A. 2002. The use of materials patterned on a nano- and micro-metric scale in cellular engineering. *Mater Sci Eng C* 19**,** 263-269.
WILSON, J. R., CADOTTE, D. W. & FEHLINGS, M. G. 2012. Clinical predictors of neurological outcome, functional status, and survival after traumatic spinal cord injury: a systematic review. *Journal of Neurosurgery-Spine,* 17**,** 11-26.
WORLDHEALTHORGANISATION. 2013. *Spinal Cord Injury* [Online]. World Health Organisation. Available: https://www.who.int/news-room/fact-sheets/detail/spinal-cord-injury [Accessed].
WUERFEL, J., PAUL, F., BEIERBACH, B., HAMHABER, U., KLATT, D., PAPAZOGLOU, S., ZIPP, F., MARTUS, P., BRAUN, J. & SACK, I. 2010. MR-elastography reveals degradation of tissue integrity in multiple sclerosis. *Neuroimage,* 49**,** 2520-5.
WUNG, N., ACOTT, S. M., TOSH, D. & ELLIS, M. J. 2014. Hollow fibre membrane bioreactors for tissue engineering applications. *Biotechnol Lett,* 36**,** 2357-66.
XICOY, H., WIERINGA, B. & MARTENS, G. J. 2017. The SH-SY5Y cell line in Parkinson's disease research: a systematic review. *Mol Neurodegener,* 12**,** 10.
XUE, H., WU, S., PAPADEAS, S. T., SPUSTA, S., SWISTOWSKA, A. M., MACARTHUR, C. C., MATTSON, M. P., MARAGAKIS, N. J., CAPECCHI, M. R., RAO, M. S., ZENG, X. & LIU, Y. 2009. A targeted neuroglial reporter line generated by homologous recombination in human embryonic stem cells. *Stem Cells,* 27**,** 1836-46.
YAMAZAKI, K., KAWABORI, M., SEKI, T. & HOUKIN, K. 2020. Clinical Trials of Stem Cell Treatment for Spinal Cord Injury. *Int J Mol Sci,* 21.
YANG, L. B., CHU, J. S. & FIX, J. A. 2002. Colon-specific drug delivery: new approaches and in vitro/in vivo evaluation. *International Journal of Pharmaceutics,* 235**,** 1-15.
YAO, J. F., WANG, K., REN, M. R., LIU, J. Z. & WANG, H. T. 2012. Phase inversion spinning of ultrafine hollow fiber membranes through a single orifice spinneret. *Journal of Membrane Science,* 421**,** 8-14.
YU, J., VODYANIK, M. A., SMUGA-OTTO, K., ANTOSIEWICZ-BOURGET, J., FRANE, J. L., TIAN, S., NIE, J., JONSDOTTIR, G. A., RUOTTI, V., STEWART, R., SLUKVIN, II & THOMSON, J. A. 2007. Induced pluripotent stem cell lines derived from human somatic cells. *Science,* 318**,** 1917-20.
YU, X. & BELLAMKONDA, R. 2001. Dorsal root ganglia neurite extension is inhibited by mechanical and chondroitin sulphate-rich interfaces. *Journal of Neuroscience Research,* 66**,** 303-310.
YU, X., ZHANG, S., ZHAO, D., ZHANG, X., XIA, C., WANG, T., ZHANG, M., LIU, T., HUANG, W. & WU, B. 2019. SIRT1 inhibits apoptosis in in vivo and in vitro models of spinal cord injury via microRNA-494. *Int J Mol Med,* 43**,** 1758-1768.
YUAN, Y. M. & HE, C. 2013. The glial scar in spinal cord injury and repair. *Neurosci Bull,* 29**,** 421-35.
ZAHUMENSKA, R., NOSAL, V., SMOLAR, M., OKAJCEKOVA, T., SKOVIEROVA, H., STRNADEL, J. & HALASOVA, E. 2020. Induced Pluripotency: A Powerful Tool for In Vitro Modeling. *Int J Mol Sci,* 21.
ZAKRZEWSKI, W., DOBRZYNSKI, M., SZYMONOWICZ, M. & RYBAK, Z. 2019. Stem cells: past, present, and future. *Stem Cell Res Ther,* 10**,** 68.
ZHAI, M. L., LI, J., YI, M. & HA, H. F. 2000. The swelling behavior of radiation prepared semi-interpenetrating polymer networks composed of polyNIPAAm and hydrophilic polymers. *Radiation Physics and Chemistry,* 58**,** 397-400.
ZHANG, S., BELL, E., ZHI, H., BROWN, S., IMRAN, S. A. M., AZUARA, V. & CUI, W. 2019. OCT4 and PAX6 determine the dual function of SOX2 in human ESCs as a key pluripotent or neural factor. *Stem Cell Res Ther,* 10**,** 122.
ZHANG, X., HUANG, C. T., CHEN, J., PANKRATZ, M. T., XI, J., LI, J., YANG, Y., LAVAUTE, T. M., LI, X. J., AYALA, M., BONDARENKO, G. I., DU, Z. W., JIN, Y., GOLOS, T. G. & ZHANG, S. C. 2010. Pax6 is a human neuroectoderm cell fate determinant. *Cell Stem Cell,* 7**,** 90-100.

ZHU, J., BALIEU, R., LU, X. & KRINGOS, N. 2018. Microstructure evaluation of polymer-modified bitumen by image analysis using two-dimensional fast Fourier transform. *Materials & Design,* 137**,** 164-175.
ZIRALDO, C., SOLOVYEV, A., ALLEGRETTI, A., KRISHNAN, S., HENZEL, M. K., SOWA, G. A., BRIENZA, D., AN, G., MI, Q. & VODOVOTZ, Y. 2015. A Computational, Tissue-Realistic Model of Pressure Ulcer Formation in Individuals with Spinal Cord Injury. *PLoS Comput Biol,* 11**,** e1004309.